Translatome analysis reveals cellular network in DLK-dependent hippocampal glutamatergic neuron degeneration

Erin M Ritchie [1,2], Siming Zhong[1], Qianyi Pu[1], Yunbo Li[1], Binhai Zheng[3], Yishi Jin[1,3,4*]

[1] Department of Neurobiology, School of Biological Sciences, University of California San Diego, La Jolla, CA 92093

[2] Biomedical Sciences Graduate Program, School of Medicine, University of California San Diego, La Jolla, CA 92093

[3] Department of Neurosciences, School of Medicine, University of California San Diego, La Jolla, CA 92093

[4] Kavli Institute of Brain and Mind, University of California San Diego, La Jolla, CA 92093

[*] Corresponding author: yijin@ucsd.edu

Running title: DLK in hippocampal glutamatergic neurons

Keywords: microtubules, Jun, stathmin, neurite differentiation, synapse formation, RiboTag-seq

7 Figures

11 Supplemental Figures

Version 07_01_24

Abstract

The conserved MAP3K12/Dual Leucine Zipper Kinase (DLK) plays versatile roles in neuronal development, axon injury and stress responses, and neurodegeneration, depending on cell-type and cellular contexts. Emerging evidence implicates abnormal DLK signaling in several neurodegenerative diseases. However, our understanding of the DLK-dependent gene network in the central nervous system remains limited. Here, we investigated the roles of DLK in hippocampal glutamatergic neurons using conditional knockout and induced overexpression mice. We found that dorsal CA1 and dentate gyrus neurons are vulnerable to elevated expression of DLK, while CA3 neurons appear largely unaffected. We identified the DLK-dependent translatome that includes conserved molecular signatures and displays cell-type specificity. Increasing DLK signaling is associated with disruptions to microtubules, potentially involving STMN4. Additionally, primary cultured hippocampal neurons expressing different levels of DLK show altered neurite outgrowth, axon specification, and synapse formation. The identification of translational targets of DLK in hippocampal glutamatergic neurons has relevance to our understanding of neurodegenerative diseases.

Introduction

The mammalian Mitogen Activated Protein Kinase Kinase Kinase (MAP3K12) Dual Leucine Zipper Kinase (DLK) is broadly expressed in the nervous system from early development to mature adults. DLK exerts its effects primarily through signal transduction cascades involving downstream MAP2Ks (MKK4, MKK7) and MAPKs (JNK, p38, ERK), which then phosphorylate many proteins, such as transcription factors including c-Jun, to regulate cellular responses (Asghari Adib et al., 2018; Hirai et al., 2006; Huang et al., 2017; Itoh et al., 2009; Jin & Zheng, 2019; Tedeschi & Bradke, 2013). In cultured neurons, DLK is localized to axons (Hirai et al., 2005; Lewcock et al., 2007), dendrites (Pozniak et al., 2013), and the Golgi apparatus (Hirai et al., 2002). DLK is also associated with transporting vesicles, which are considered platforms for DLK to serve as a sensor of neuronal stress or injury (Holland et al., 2016; Tortosa et al., 2022). Despite broad expression, functional investigations of DLK have been limited to select cell types under specific conditions.

Constitutive DLK knockout (KO) mice, generated by removing the first 224 amino acids including the ATP binding motif of the kinase domain (Hirai et al., 2006), or by deleting the entire kinase domain (Ghosh et al., 2011), die perinatally. The development of the embryonic nervous system is largely normal, with mild defects in several regions of the brain, such as radial migration and axon development in the cortex (Hirai et al., 2006) and neuronal apoptosis during development of spinal motor neurons and dorsal root ganglion (DRG) neurons (Ghosh et al., 2011; Itoh et al., 2011). Selective removal of DLK in layer 2/3 cortical neurons starting at E16.5 results in increased dendritic spine volume (Pozniak et al., 2013). Induced deletion of DLK in adult mice causes no obvious brain structural defects; synapse size and density in hippocampus and cortex appear unaltered, although basal synaptic strength is mildly increased (Pozniak et al., 2013). In contrast, under injury or stress conditions, DLK has critical context-specific roles. In DRG neurons, DLK is required for nerve growth factor withdrawal induced death, promotes neurite regrowth, and is also involved in retrograde injury signaling (Ghosh et al., 2011; Holland et al., 2016; Itoh et al., 2009; Shin et al., 2012). In a spinal cord injury model, DLK is required for *Pten* deletion-induced axon regeneration and sprouting as well as spontaneous sprouting of uninjured corticospinal tract neurons (Saikia et al., 2022). In optic nerve crush assay, DLK is necessary for *Pten* deletion-induced axon regeneration of retinal ganglion cells (RGC), but also contributes to injury-induced RGC death (Watkins et al., 2013). In a mouse model of stroke, increased DLK expression is associated with motor recovery following knockdown of the CCR5

chemokine receptor (Joy et al., 2019). These studies reveal critical roles of DLK in development, maintenance, or repair of neuronal circuits.

DLK is known to be expressed in hippocampal neurons (Blouin, 1996; Hirai et al., 2005; Mata et al., 1996). However, loss of DLK, either constitutively or in adult animals, causes no discernable effect on hippocampal morphology (Hirai et al., 2006; Pozniak et al., 2013). Microarray-based gene expression analysis did not detect significant changes associated with loss of DLK in the hippocampus (Pozniak et al., 2013). However, following exposure to kainic acid, loss of DLK, or preventing phosphorylation of the downstream transcription factor c-Jun, significantly reduces neuron death in hippocampus (Behrens et al., 1999; Pozniak et al., 2013). Additionally, elevated levels of p-c-Jun have been observed in hippocampus of patients with Alzheimer's disease (Le Pichon et al., 2017). Induced human neurons treated with ApoE4, a prevalent ApoE variant associated with Alzheimer's disease, also show upregulation of DLK, which leads to enhanced transcription of APP and thus Aβ levels (Huang et al., 2017). These data suggest transcriptional changes downstream of DLK signaling may be an important aspect of DLK signaling in hippocampal neuron degeneration under pathological conditions.

Here, we investigate the DLK-dependent molecular and cellular network in hippocampal glutamatergic neurons, which show selective vulnerability in Alzheimer's disease, ischemic stroke, and excitotoxic injury. Using DLK conditional knockout and overexpression mice, we reveal hippocampal regional differences in neuronal death upon elevated DLK signaling. We describe translational changes in hippocampal glutamatergic neurons using RiboTag-seq analysis. We show that the key transcription factor c-Jun and a member of the stathmin family, STMN4, display DLK-dependent translation. Our analyses on hippocampal tissues and cultured neurons support the conclusion that the DLK-dependent signaling network has important roles in the regulation of microtubule homeostasis, neuritogenesis, and synapse formation.

Results

DLK conditional knockout in differentiating and mature glutamatergic neurons does not alter gross morphology of hippocampus

As a first step to defining the roles of DLK in hippocampal glutamatergic neurons, we verified DLK expression in hippocampal tissue by RNAscope analysis. Consistent with prior in situ data (Blouin, 1996; Lein et al., 2007; Mata et al., 1996), we observed strong signals in the glutamatergic pyramidal cells and granule cells in P15 mice (Fig.S1A). To selectively delete DLK in glutamatergic neurons, we generated *Vglut1*$^{Cre/+}$*;DLK(cKO)*$^{fl/fl}$ mice. *DLK(cKO)*$^{fl/fl}$ have LoxP sites flanking the exon encoding the initiation ATG and the first 149 amino acids (Chen et al., 2016). *Vglut1*^{Cre} expression in hippocampus shows strong expression in CA3 and in a subset of pyramidal neurons close to stratum oriens in CA1 at P4, with broad expression in both CA1 and CA3 by P14 (Harris et al., 2014). In dentate gyrus, expression of *Vglut1*^{Cre} begins in neurons nearer the molecular layer around P4, with expression spreading towards the polymorph layer gradually during the first two postnatal months. By western blot analysis of hippocampal protein extracts we found that conditional deletion of DLK resulted in significantly reduced full-length protein (Fig.1A,B). The DLK antibody also detected a protein product of lower molecular weight at much reduced levels with longer exposure (Fig.S1B). As *Dlk* mRNA lacking the floxed exon was expressed (Fig.S1C), this lower-molecular weight protein could be produced by using a downstream alternative start codon, but lacks the N-terminal palmitoylation motif and ATP-binding site that are essential for DLK activity (Holland et al., 2016; Huntwork-Rodriguez et al., 2013). These data confirm a significant reduction in DLK protein with *Vglut1*$^{Cre/+}$*;DLK(cKO)*$^{fl/fl}$.

The *Vglut1*$^{Cre/+}$*;DLK(cKO)*$^{fl/fl}$ mice showed no detectable abnormality in behavior or appearance from birth to about one year of age. We examined tissue sections of hippocampus in P15 and P60 mice. Hippocampal sections stained with NeuN, a marker of neuronal nuclei, showed no significant difference in overall position of neuronal soma or thickness of the CA1 pyramidal cell layer at either timepoint (Fig.1C,D). Neuronal morphology visualized by immunostaining with Tuj1, labeling neuron-specific beta-III tubulin, also showed no obvious differences in the pattern and intensity of microtubules in *Vglut1*$^{Cre/+}$*;DLK(cKO)*$^{fl/fl}$ mice, compared to control (Fig.1E-H). Hippocampal morphology in 1 year old *Vglut1*$^{Cre/+}$*;DLK(cKO)*$^{fl/fl}$ mice was also indistinguishable from controls (Fig.S1D, S1F-H). These results show that DLK does not have essential roles in post-mitotic hippocampal glutamatergic neuron maintenance.

Increasing expression levels of DLK leads to hippocampal neuron death, with dorsal CA1 neurons showing selective vulnerability

We next asked how increased DLK signaling affects hippocampal glutamatergic neurons. We previously described a transgenic mouse, *H11-DLK*$^{iOE/+}$, allowing Cre-dependent DLK overexpression, which promotes DLK activity (Li et al., 2021). The DLK transgene is coexpressed with tdTomato through a T2A peptide. We generated *Vglut1* $^{Cre/+}$*;H11-DLK*$^{iOE/+}$ mice and confirmed increased *Dlk* mRNAs in CA1, CA3, and DG by RNAscope (FigS2A,B). By immunostaining hippocampal sections with anti-DLK antibodies we observed increased protein levels particularly in regions with pyramidal neuron dendrites in *Vglut1* $^{Cre/+}$*;H11-DLK*$^{iOE/+}$, comparing to control mice (Fig.S2C).

Vglut1 $^{Cre/+}$*;H11-DLK*$^{iOE/+}$ mice were born normally, and developed noticeable progressive motor deficits around four months of age with movement strongly affected around one year of age. We stained brain sections for NeuN at P10, P15, P60, and 1 year of age and observed a progressive reduction in brain size of these mice, compared to controls. At P10, the dorsal hippocampus in *Vglut1* $^{Cre/+}$*;H11-DLK*$^{iOE/+}$ was indistinguishable from control (Fig.2A, 2B). By P15, the mice showed significant thinning of the CA1 pyramidal layer, compared to control. TUNEL staining on hippocampal tissue showed that in control mice the CA1 pyramidal layer had few neurons undergoing cell death, while there were increased TUNEL signals in *Vglut1* $^{Cre/+}$*;H11-DLK*$^{iOE/+}$ mice (Fig.S4E, S4F). By P60, most CA1 pyramidal neurons were lost, while DG began to show thinning, which continued to worsen at 1 year of age (Fig.2A, 2B, S1E, S1H). In contrast, neurons in CA3 were largely unaffected, even at 1 year of age (Fig.2A, S1E, S1G). Additionally, we noticed that in P60 *Vglut1* $^{Cre/+}$*;H11-DLK*$^{iOE/+}$ mice, dorsal CA1 showed significantly fewer surviving neurons, while ventral CA1 pyramidal layer thickness appeared more similar to control than dorsal regions (Fig.S3A,B). Neuronal death generally induces reactive astrogliosis. We stained for GFAP, a marker of astrocyte reactivity, and found increased GFAP signal specifically in CA1 at P15, and at four months of age in CA1 and DG, but not CA3 (Fig.S4A-D). Together, these data reveal that dorsal CA1 neurons are vulnerable to elevated DLK expression, while neurons in CA3 appear largely resistant to DLK overexpression.

DLK dependent translated genes are enriched in synapse formation and function

To gain molecular understanding of gene expression associated with DLK in glutamatergic neurons, we next conducted translating ribosome profiling and RNA sequencing (RiboTag profiling) using *Rpl22*^{HA} mice, which enables Cre-dependent expression of an HA tagged RPL22, a component of the ribosome, from its endogenous locus (Sanz et al., 2009). We generated *Vglut1* $^{Cre/+}$*;H11-DLK*$^{iOE/+}$*;Rpl22*$^{HA/+}$, *Vglut1*$^{Cre/+}$*;DLK(cKO)*$^{fl/fl}$*;Rpl22*$^{HA/+}$, and their respective *Vglut1*$^{Cre/+}$*;Rpl22*$^{HA/+}$ sibling controls. We made protein extracts from dissected hippocampi of P15 mice, a time point at the early stages of DLK-dependent neuron degeneration. We obtained affinity purified HA-immunoprecipitates with the associated actively translated RNAs (Fig.S5A) (n=3 DLK(iOE)/3 WT or n=4 DLK(cKO)/4 WT). The purity of the isolated RNA samples was assessed by qRT-PCR using markers for glutamatergic neurons (*Vglut1*), CA1 pyramidal neurons (*Wfs1*), astrocytes (*Gfap*), and inhibitory neurons (*Vgat*) (Fig.S5B).

We mapped >24 million deep sequencing reads per sample to approximately 14,000 genes. We found 260 genes that were differentially translated in DLK(iOE) neurons compared to control with 114 upregulated and 146 downregulated (Fig.3A, using the cutoff of $p_{adj}<0.05$). 36 genes showed significant changes in DLK(cKO) compared to control with 24 down-regulated and 12 up-regulated, (Fig.3B, $p_{adj}<0.05$). Among genes with statistically significant changes, 17 genes were detected in both DLK(cKO) and DLK(iOE) (Fig.S5C). Of these, 13 genes were upregulated in DLK(iOE) and downregulated in DLK(cKO), and 3 genes were downregulated in DLK(iOE) and upregulated in DLK(cKO) (Fig.S5D, S5E). The most significant differentially expressed genes included *Jun,* encoding the DLK downstream transcription factor c-Jun, *Stmn4,* encoding a member of the Stathmin tubulin-binding protein family, and *Sh2d3c*, encoding a SH2-domain cytoplasmic signaling protein (Dodelet et al., 1999; Vervoort et al., 2007). One gene, *Slc25a17*, a peroxisomal transporter for cofactors FAD, CoA, and others (Agrimi et al., 2012) and broadly implicated in oxidative stress, was upregulated in both conditional knockout and overexpression of DLK compared to control, though the relevance of this change may require further investigation. To systematically compare whether DLK regulates the translatome in a coordinated manner, we performed rank-rank hypergeometric overlap (RRHO) analysis (Plaisier et al., 2010) on the entire translated mRNAs detected in DLK(iOE) and DLK(cKO). We found that RRHO detected significant overlap in genes which are upregulated in DLK(iOE) and downregulated in DLK(cKO) as well as the reverse (Fig.3C), supporting a conclusion that many of the same genes are constitutively regulated by DLK and when DLK levels are increased.

To gain understanding of DLK-dependent molecular and cellular network, we performed gene ontology analysis on the 260 genes differentially translated in DLK(iOE) neurons, as this dataset gave greater ability to detect significant GO terms than using the 36 genes identified in DLK(cKO). The genes upregulated in DLK(iOE) (114) showed enrichment in GO terms related to neuron apoptosis, cell migration, cell adhesion, and the extracellular matrix organization (Fig.3D), whereas the genes downregulated (146) had GO terms related to synaptic communication and ion transport (Fig.3E). To search for enrichment of curated cellular pathways from various databases, we conducted gene set enrichment analysis (GSEA) using the entire translatome (>12,000 genes from DLK(iOE) expression, ranking genes by $\log_2$ fold change). Compared to control, we found significant enrichment ($q<0.05$) of pathways relating to extracellular matrix organization, apoptosis, unfolded protein responses, the complement cascade, DNA damage responses, and glycosylation of proteins, and depletion of pathways relating to mitochondrial electron transport, synaptic adhesion molecules, potassium channels, and G-protein signaling (Fig.S5K). Among the genes upregulated in DLK(iOE), some were known to be involved in neurite outgrowth (*Plat*, others below), endocytosis or endosomal trafficking (*Snx16, Ston2, Hap1*), whereas the genes showing downregulation in DLK(iOE) included ion channel subunits (*Cacng8, Cacng3, Grin2b, Scn1a*) and those in exocytosis and calcium related proteins (*Doc2b, Hpca, Cadps2, Rab3c, Rph3a*). A significant cluster of differentially expressed genes in DLK(iOE) included those that regulate AMPA receptors (*Nptx1, Nptxr, Cnih3, Gpc4, Arc, Tspan7)* and cell adhesion molecules at synapses (*Nectin1, Flrt3, Pcdh8, Plxnd1*). A further survey using SynGO, a curated resource for genes related to synaptic function (Koopmans et al., 2019), also revealed 42 of 260 differentially translated genes in DLK(iOE) showed synaptic function with significant enrichment in synaptic organization and regulation of postsynaptic neurotransmitter receptor signaling processes (Fig.3F). Conversely, SynGo analysis revealed 10 of the 36 differentially translated genes in DLK(cKO) to function in similar synaptic processes as in DLK(iOE) (Fig.S5J). The bioinformatic analysis suggests that increased DLK expression can promote translation of genes related to neurite outgrowth and branching and reduce those related to the maturation and function of synapses.

The hippocampus is comprised of multiple glutamatergic neuron types with distinct spatial patterns of gene expression (Lein et al., 2004). As we observed regional vulnerability to DLK overexpression, we next asked if the differentially expressed genes associated with DLK(iOE) might show correlation to the neuronal vulnerability. We categorized the endogenous expression patterns of the 260 significantly changed genes in DLK(iOE) in CA1, CA3, and DG in hippocampus using in situ data from 8-week-old mice from the Allen Brain Atlas (Lein et al.,

2007). We found that around a third of the genes downregulated in DLK(iOE) showed enriched expression in CA1 (Fig.S5G), and some of these genes including *Tenm3, Lamp5,* and *Mpped1* were also up-regulated in DLK(cKO) (Fig.S5H, S5I). In comparison, about 50% of the genes upregulated in DLK(iOE) were similarly expressed among different cell types (Fig.S5F). Analysis of the DLK-dependent synaptic genes from our DLK(iOE) translatome further showed that a large portion of downregulated synaptic genes showed enriched expression in CA1 compared to CA3 or DG (Fig.3H), while upregulated synaptic genes were expressed in all regions (Fig.3G). The enrichment of DLK-dependent translation of genes in CA1 suggests that the decreased expression of these genes may contribute to CA1 neuron vulnerability to elevated DLK.

DLK regulates translation of JUN and STMN4

The transcription factor c-Jun is a key downstream factor in DLK and JNK signaling (Hirai et al., 2006; Itoh et al., 2009; Welsbie et al., 2017). Our RiboTag analysis revealed translation of *Jun* mRNA to be significantly dependent on DLK expression levels (Fig.3A,B). To validate this observation, we performed immunostaining of hippocampal tissues using an antibody recognizing total c-Jun. The fluorescence intensity of c-Jun staining in most regions of the hippocampus in *Vglut1*$^{Cre/+}$*;DLK(cKO)*$^{fl/fl}$ mice was comparable to that in the control mice, with CA3 area showing a trend towards reduced expression (Fig.S6A, P60). In *Vglut1* $^{Cre/+}$*;H11-DLK*$^{iOE/+}$ mice, we observed increased immunostaining intensity of c-Jun in CA3 and DG with the strongest increase (~4-fold) in CA1, compared to age-matched control mice (Fig.S6C, P15). Phosphorylation of c-Jun (p-c-Jun) is known to reflect activation of DLK and JNK signaling (Hirai et al., 2006). We further investigated p-c-Jun levels in these mice. In *Vglut1*$^{Cre/+}$*;DLK(cKO)*$^{fl/fl}$ mice, p-c-Jun levels in CA3 showed a significant reduction, with the trend of reduced levels in CA1 and DG, compared to control mice (Fig.S6B, P60). In *Vglut1* $^{Cre/+}$*;H11-DLK*$^{iOE/+}$ mice, levels of p-c-Jun were increased in glutamatergic neurons of CA1 (~10-fold), CA3 (~6-fold), and DG (~8-fold), compared to control mice (Fig.S6, P15). The levels of p-c-Jun remained elevated in the surviving neurons in all three regions of *Vglut1* $^{Cre/+}$*;H11-DLK*$^{iOE/+}$ mice at P60 (Fig.S3C). These results show that the translation of *Jun* mRNAs and phosphorylation of c-Jun is not only dependent on DLK, but also the degree of dependence is regional, with CA1 neurons showing higher dependence.

The Stathmin family of proteins is thought to regulate microtubules through sequestering tubulin dimers (Charbaut et al., 2001; Chauvin & Sobel, 2015). This family of proteins includes

four genes, which were all identified in our hippocampal glutamatergic neuron translatome. *Stmn4* showed significant up- or downregulation in DLK(iOE) or DLK(cKO), respectively (Fig.3A,B), while *Stmn1-3* showed no significant difference in either translatome dataset (Fig.S7A). We verified STMN4 protein expression by western blot of protein extracts from hippocampal tissues. In control mice, we detected the expression of STMN4 to peak around P8 (Fig.S7B,C,F,G). The abundance of STMN4 in DLK conditional knockout and overexpression was subtly altered, which could be due to broad expression of STMN4 in hippocampus masking specific changes in glutamatergic neurons. We thus examined *Stmn4* RNA changes in hippocampus by RNAscope. *Stmn4* mRNA was detected in glutamatergic neurons across all regions of the hippocampus, with strongest expression in CA1 pyramidal neurons. In *Vglut1* $^{Cre/+}$*;H11-DLK*$^{iOE/+}$ mice, glutamatergic neurons in CA1, CA3, and DG all showed upregulation of *Stmn4* (Fig.4A-C, S8A,C). In *Vglut1*$^{Cre/+}$*;DLK(cKO)*$^{fl/fl}$ mice downregulation of *Stmn4* was statistically significant in CA3 (Fig.4A-C). Overall, these data support a role of DLK in promoting translation of *Stmn4*.

Altered DLK activity disrupts microtubule homeostasis in hippocampal CA1 neurons

Substantial studies from other types of neurons in mice and invertebrate animals have linked DLK signaling with the regulation of microtubule cytoskeleton (Asghari Adib et al., 2018; Jin & Zheng, 2019; Tedeschi & Bradke, 2013). The observation that *Stmn4* translation in hippocampal glutamatergic neurons shows dependency on expression levels of DLK implies a likelihood of altered microtubule stability in these neurons. To assess microtubule distribution, we performed Tuj1 immunostaining on hippocampal tissues. We did not detect obvious changes in *Vglut1*$^{Cre/+}$*;DLK(cKO)*$^{fl/fl}$ when compared to controls at P60 (Fig.1E). In *Vglut1* $^{Cre/+}$*;H11-DLK*$^{iOE/+}$ mice at P15, we also did not identify consistent differences in expression levels or patterns of neuronal microtubules in any region of hippocampus (Fig.4D, S8E), and we generally found the microtubule staining pattern at P15 to be less defined and consistent compared to P60. At P60, *Vglut1* $^{Cre/+}$*;H11-DLK*$^{iOE/+}$ exhibited thinning of all strata within CA1, and the Tuj1 staining pattern became less organized in parallel dendrites in the stratum radiatum (SR) region of CA1 (Fig.4I). Increased Tuj1 staining in thin branches extended in varied directions, with particularly bright staining in the apical dendrite near the pyramidal neuron cell body.

Several post-translational modifications of microtubules are thought to correlate with stable or dynamic state of microtubules. To further explore whether DLK expression levels

affected microtubule post-translational modifications, we performed immunostaining for acetylated tubulin, a modification generally associated with stable, longer-lived microtubules, and tyrosinated tubulin, a terminal amino acid that can be reversibly or irreversibly removed and is typically found on dynamic microtubules (Janke & Magiera, 2020). We detected no significant difference in the staining pattern and intensity of either tyrosinated tubulin or acetylated tubulin in *Vglut1*$^{Cre/+}$*;DLK(cKO)*$^{fl/fl}$ mice, compared with age-matched control mice (Fig.4N-R). Accordingly, both tubulin modifications showed no significant differences in pattern or intensity in CA1 SR of *Vglut1* $^{Cre/+}$*;H11-DLK*$^{iOE/+}$ compared to age-matched control mice at P15 (Fig.4E-H) despite neuron death beginning in CA1. However, by P60, we observed increased staining intensity of acetylated tubulin and tyrosinated tubulin in the apical dendrites of surviving neurons in *Vglut1* $^{Cre/+}$*;H11-DLK*$^{iOE/+}$ mice, particularly with tyrosinated tubulin staining revealing bright signals on small, thin branches (Fig.4J-M). To discern whether such microtubule modification changes were from neurons, we immunostained with antibodies for MAP2, a neuron specific microtubule associated protein, and observed bright MAP2 signal in thin branches extending in varied directions in *Vglut1* $^{Cre/+}$*;H11-DLK*$^{iOE/+}$ mice, compared to age-matched control mice (Fig.S8F,G). Together this analysis suggests increased DLK expression likely alters neuronal microtubule homeostasis and/or integrity.

Increasing DLK expression alters synapses in dorsal CA1

A consistent theme revealed in our hippocampal glutamatergic neuronal RiboTag profiling suggests that translation of synaptic proteins is likely dependent on the expression levels of DLK. To evaluate the effect of DLK in the hippocampus, we examined synapses using antibodies for Bassoon, a core protein in the presynaptic active zone, Vesicular Glutamate Transporter 1 (VGLUT1) for synaptic vesicles, and Homer1, a post-synaptic scaffolding protein. We immunostained P60 *Vglut1*$^{Cre/+}$*;DLK(cKO)*$^{fl/fl}$ mice and P15 *Vglut1* $^{Cre/+}$*;H11-DLK*$^{iOE/+}$ with littermate control mice. In control mice, Bassoon staining showed discrete puncta that were mostly apposed to the postsynaptic marker Homer1, representing properly formed synapses (Fig.5A). We measured synapse density by counting Bassoon and Homer1 puncta as well as the sites of Bassoon and Homer1 overlap. We measured synapse density in stratum radiatum (SR) of dorsal CA1, where CA3 neurons synapse onto CA1 dendrites. In *Vglut1*$^{Cre/+}$*;DLK(cKO)*$^{fl/fl}$ at P60 we saw no significant difference in the density of Bassoon or Homer1 puncta (Fig.5A-C). We noted a subtle reduction in Bassoon puncta size and increase in Homer1 puncta size, with smaller overlapped regions in *Vglut1*$^{Cre/+}$*;DLK(cKO)*$^{fl/fl}$ (Fig.S9G-I). The density of colocalized

puncta of Bassoon and Homer1, representing synapses, was also similar in *Vglut1*$^{Cre/+}$*;DLK(cKO)*$^{fl/fl}$ compared to control (Fig.5D). *Vglut1* $^{Cre/+}$*;H11-DLK*$^{iOE/+}$ at P15 did not cause detectable changes in Bassoon density, but we detected reduced Homer1 density in SR of CA1 (Fig.5E-G) and fewer synapses showing colocalization of Basson and Homer1 with *Vglut1* $^{Cre/+}$*;H11-DLK*$^{iOE/+}$ compared to control (Fig.5H). We found slightly smaller Homer1 puncta with *Vglut1* $^{Cre/+}$*;H11-DLK*$^{iOE/+}$ compared to control, though there was no change to the size of Bassoon or the overlap size of Bassoon and Homer1 (Fig.S9J-L). Staining of VGLUT1 protein showed less discrete puncta than those of Bassoon or Homer1, with small puncta and larger clusters of puncta close together. Loss of DLK was associated with an increased number of VGLUT1 puncta, and puncta were slightly smaller on average (Fig.S9A-C). Increased expression of DLK led to fewer VGLUT1 puncta in SR like we observed with Homer1 at P15 (Fig.S9D-F). Average VGLUT1 puncta size was increased with DLK overexpression (Fig.S9D-F). These data reveal that while conditional knockout of DLK may not have a strong effect on synapse number, increased expression of DLK leads to fewer synapses.

High levels of DLK cause short neurite formation in primary hippocampal neurons

To gain better resolution on how DLK expression levels affect glutamatergic neuron morphology and synapses, we next turned to primary hippocampal cultures. To enable visualization of Vglut1 positive neurons, we introduced a floxed Rosa26-tdTomato reporter into our mice (Madisen et al., 2010). We prepared primary hippocampal neurons from P1 pups and fixed cultured neurons at day in vitro 2 (DIV2) so only around ¼ of glutamatergic neurons had tdTomato and our genotype of interest (DLK(cKO), WT, or DLK(iOE)). We verified DLK protein pattern and levels by immunostaining with DLK antibodies (Fig.6A). In neurons from control mice, DLK was localized to cell soma, likely reflecting Golgi apparatus localization as reported (Hirai et al., 2002) and neurites, particularly the axon growth cone regions. In these cultures, we also immunostained for STMN4 and observed a punctate localization in the cell soma of hippocampal neurons likely corresponding to the Golgi and in neurites and growth cones (Fig.6A), in line with published data (Chauvin et al., 2008; Gavet et al., 2002), although STMN4 puncta appeared to be non-overlapping with DLK (Fig.S10B). In neurons from DLK(cKO), STMN4 exhibited a similar pattern to control, and STMN4 levels were not significantly decreased at DIV2. In neurons from DLK(OE), DLK levels were increased, and STMN4 levels were also increased (Spearman correlation r=0.7454) (Fig.6A,B), supporting our RiboTag analysis. STMN2 has been reported to be associated with DLK dependent responses in DRG

neurons (Summers et al., 2020; Thornburg-Suresh et al., 2023). Although our RiboTag analysis did not identify significant changes of *Stmn2*, we tested whether STMN2 protein level could be altered in cultured hippocampal neurons. In DIV2 control cultured neurons STMN2 staining revealed punctate localization similar to STMN4 in the perinuclear region likely corresponding to the Golgi (Gavet et al., 2002; Lutjens et al., 2000), along with punctate signal in neurites and growth cones. By immunostaining for DLK and STMN2 simultaneously, and measuring the staining intensity of DLK and STMN2 in cell somas, we detected a moderately positive correlation between DLK and STMN2 (Fig.S10C,D, Spearman correlation r=0.4693). These data suggest that in hippocampal glutamatergic neurons DLK has a stronger effect on STMN4 levels but may also regulate protein levels of STMN2.

In control cultures at DIV2, the majority of tdTomato labeled neurons generally developed multiple neurites from the cell soma, with one neurite developing into an axon, defined here as a neurite longer than 90 µm (Fig.S10A). At this timepoint the neurites are actively growing and establish thicker branches, which develop into dendrites and axons (Dotti, Sullivan, & Banker, 1988). Thin, often short, neurites could be observed branching off from the cell soma, axons, dendrites, and growth cones. In DLK(cKO) cultured neurons, we observed a trend of more neurons without an axon (Fig.6C), however the differentiated axons appeared indistinguishable from control. Additionally, we quantified the total number of neurites around the cell soma and observed fewer neurites (Fig.6A,D). In DLK(iOE) neurons, we observed a significant increase in neurons without an axon and in those with multiple axons (Fig.6C, S10A). Neurons exhibiting high DLK protein in the cell soma displayed an increased number of neurites, either around the cell soma as primary neurites or as secondary neurites (Fig.6A,D). Such neurites were typically thin, and frequently appeared short, like filopodia. These thin neurites also sometimes developed a rounded tip and showed beading and degeneration, with neurites appearing variable in thickness (Fig.6A,E). These data support a role for DLK in both short neurite formation and axon specification in hippocampal glutamatergic neurons.

With cultured neurons, we were able to further analyze microtubules in individual neurites. Control neurons exhibited staining for acetylated tubulin in differentiated axons and dendrites and in the central region of growth cones where stable microtubules are present. Acetylated tubulin was absent from filopodia and microtubules in the peripheral regions of growth cones. Tyrosinated tubulin was also present in differentiated axons and dendrites as well as filopodia and towards to peripheral regions of growth cones. The thin neurites in neurons expressing very high levels of DLK appeared to have thin bundles of microtubules and generally

were not associated with a growth cone or microtubules splaying apart at the end as is common in WT growth cones. DLK-dependent neurites also commonly had tyrosinated tubulin, while acetylated tubulin was frequently absent (Fig.6E,F). Additionally, STMN4 was present in the thin neurites (Fig.6A), suggesting the thin neurites may likely be dynamic in nature. Overall, our results suggest DLK regulates axon formation and promotes the formation of short, thin, dynamic branches in hippocampal neurons.

Increased DLK expression alters synapse formation in primary hippocampal neurons

Our RiboTag data showed DLK significantly affected synaptic genes, with genes related to cell adhesion, calcium signaling, and AMPA receptor expression at the synapse, which may contribute to changes in dendritic spine morphology and synaptic connections. We also observed increased DLK levels led to reduced synapse density in tissue. To further investigate the effects of DLK expression on synapses, we immunostained the cultured hippocampal neurons at DIV14 with Bassoon. The control neurons showed discrete Bassoon puncta in axons. DLK(cKO) neurons showed no significant change in Bassoon puncta size or density (Fig.7A-C). In contrast, DLK(iOE) neurons showed abnormal Bassoon staining that was larger and irregular in shape (Fig.7A-C), suggesting that high levels of DLK disrupted presynaptic active zones in neurons.

We also observed dendritic spine morphology and frequency in neurons with increase or loss of DLK. Morphology of spines is associated with differences in maturity, with mushroom spines representing a more mature morphology than thin spines (Yoshihara et al., 2009). At DIV14, many control neurons developed dendrites with dendritic spines that were visible by tdTomato. We categorized spines by their morphology into different types, including long thin, thin, stubby, mushroom, and branched spines following previous studies (Risher et al., 2014). We evaluated both the density and type of dendritic spines formed at DIV14 on neurons with spines. Neurons from DLK(cKO) showed spines at a higher density than control neurons (Fig.7D,E), with significantly more mushroom spines (Fig.7F). In contrast, in DLK(iOE) cultures, we observed fewer neurons with large, mature dendritic spines (Fig.7D-G). Neurons with dendritic spines had a reduced density of dendritic spines compared to control neurons. DLK(iOE) neurons also generally formed spines that tended to be more immature, with significantly fewer mushroom spines and a higher percentage of thin spines. These results reveal expression levels of DLK are inversely correlated with spine density and maturity.

Discussion

Selective vulnerability of hippocampal glutamatergic neurons to increased DLK expression

It is generally known that under normal conditions, the abundance of endogenous DLK in many parts of the brain is kept at low level. However, elevated DLK signaling has been associated with traumatic injury and implicated in Alzheimer's disease and other neurodegenerative disorders (Asghari Adib et al., 2018; Huang et al., 2017; Jin & Zheng, 2019; Le Pichon et al., 2017; Tedeschi & Bradke, 2013). In this study, we combined conditional knockout and overexpression of DLK to uncover its roles in the hippocampal glutamatergic neurons. Our finding that conditional deletion of DLK in the glutamatergic neurons using *Vglut1*^{Cre} in late embryonic development does not cause discernable morphological defects is consistent with the previous reports that hippocampal neurons are largely normal in constitutive knockout of DLK (Hirai et al., 2006; Hirai et al., 2011). In contrast, induced overexpression of DLK, which leads to activation of JNK signaling evidenced by increased p-c-Jun, causes the glutamatergic neurons in dorsal CA1 and dentate gyrus to undergo pronounced death, while CA3 neurons appear largely unaffected even under chronic elevated DLK expression. This pattern of DLK-induced neuronal death shares similarity to the differential vulnerability of CA1 and CA3 neurons reported in patients with Alzheimer's disease (West et al., 1994), and animal models of oxidative stress (Wilde et al., 1997), ischemia (Smith et al., 1984), and glutamate excitotoxicity from NMDA (Vornov et al., 1991). The dorsal-ventral hippocampal neuron death pattern associated with increased expression of DLK is also similar to that observed in animal models of ischemia (Smith et al., 1984). Such regional differences of hippocampal neurons in response to insults or genetic manipulation may be attributed to multiple factors, such as the nature of the neural network (Viana da Silva et al., 2024), intrinsic differences between CA1 and CA3 neurons in their abilities to buffer calcium changes, mitochondrial stress, protein homeostasis, glutamate receptor distribution (Schmidt-Kastner, 2015), and as discussed further, the degree to which transcription factors, such as p-c-Jun or other AP1 factors, are activated under different conditions.

DLK-dependent cellular network exhibits commonality and cell-type specificity

DLK to JNK signaling is known to lead to transcriptional regulation. Several studies have used transcriptomic profiling to reveal DLK-dependent gene expression in different regions of the

brain, such as cerebellum and forebrain, and in specific neuron types, such as DRG neurons and RGC neurons following axon injury or nerve growth factor withdrawal (Goodwani et al., 2020; Hu et al., 2019; Larhammar et al., 2017; Le Pichon et al., 2017; Shin et al., 2019; Watkins et al., 2013). One recent study reported RiboTag profiling of the DLK-dependent gene network in axotomized spinal cord motor neurons (Asghari Adib et al., 2024). In agreement with the overall findings from these studies, we find that loss of DLK in hippocampal glutamatergic neurons results in modest expression changes in a small number of genes, while overexpression of DLK leads to expression changes in a larger set of genes. Gene ontology and pathway analysis of our hippocampal glutamatergic neuron translatome reveals a similar set of terms as found in the other expression studies, including neuron differentiation, apoptosis, ion transport, and synaptic regulation.

Comparison of the translational targets of DLK in our study with these prior analyses also shows notable differences that are likely specific to neuron-type and contexts of experimental manipulations. For example, we find a strong induction of *Jun* translation associated with increased expression of DLK, but no significant changes in *Atf3* or *Atf4* translation, which were reported to show DLK-dependent increases in axotomized spinal cord motoneurons, and injured RGCs and DRGs (Asghari Adib et al., 2024; Larhammar et al., 2017; Shin et al., 2019; Watkins et al., 2013). Most ATF4 target genes (Somasundaram et al., 2023) also show no significant changes in our hippocampal glutamatergic neuron translatome. Moreover, we find a cohort of synaptic genes showing expression dependency on DLK, such as *Tenm3, Nptx1*, and *Nptxr,* but not any of the complement genes (*C1qa, C1qb, C1qc*), which are up-regulated in the regenerating spinal cord motor neurons where neuron-immune cell interaction has a critical role (Asghari Adib et al., 2024). Genomic structure and regulation intrinsic to the cell type may be a major factor underlying the gene expression differences in ours and other studies. Elevated DLK signaling in axotomized neurons may promote a strong regenerative response through activation of transcription factors, such as ATF3 and ATF4, whereas JUN and others that are actively expressed in hippocampal neurons may lead to a strong effect on synaptic tuning in response to DLK signaling. Overall, ours and the previous studies underscore the importance of systematic dissection of molecular pathways to understand neuron-type specific functionality to DLK signaling.

Our analysis of the spatial expression patterns of DLK-dependent genes provides molecular insight to the differential vulnerability of hippocampal glutamatergic neurons under neurodegenerative conditions. We find that a select set of DLK-dependent genes are enriched

in CA1 and are down-regulated upon DLK overexpression, suggesting that their expression may contribute to neuronal resilience. The c-Jun transcription factor has a key role in hippocampal cell death responses as mutations preventing c-Jun phosphorylation led to decreased neuronal apoptosis in the hippocampus following treatment with kainic acid (Behrens et al., 1999). Basal levels of phosphorylated c-Jun in hippocampus are generally low (Goodwani et al., 2020; Pozniak et al., 2013). We find modest reductions in total c-Jun and p-c-Jun in DLK(cKO) glutamatergic neurons, consistent with previous studies of the constitutive knockout of DLK (Hirai et al., 2006). In contrast, in DLK(iOE) neurons, translation of c-Jun and phosphorylation of c-Jun are increased, with CA1 neurons exhibiting higher increase than CA3 neurons. The c-Jun promoter has consensus AP1 sites, and c-Jun can regulate its own expression levels in cancer cell lines (Angel et al., 1988), NGF-deprived sympathetic neurons (Eilers et al., 1998) and kainic acid treated hippocampus (Mielke et al., 1999). We speculate that DLK and c-Jun may constitute a positive feedback regulation in hippocampal neurons. Together with other DLK-dependent genes, this DLK and Jun regulatory network could underlie the regional differences in hippocampal neuronal vulnerability under pathological conditions.

Conserved functions of DLK in regulating Stathmins

Stathmins are tubulin binding proteins broadly expressed in many types of neurons. Several studies have reported that DLK can regulate the expression of different Stathmin isoforms in multiple neuron types under injury conditions (Asghari Adib et al., 2024; DeVault et al., 2024; Hu et al., 2019; Larhammar et al., 2017; Le Pichon et al., 2017; Shin et al., 2019). In the hippocampus *Stmn2* is expressed at a higher level than *Stmn4*, with the relative ratios of *Stmn4*:*Stmn2* in hippocampus much higher than in DRGs (Zeisel et al., 2018). We find that translation of *Stmn4* shows significant dependence on DLK. ChIP-seq data for Jun from ENCODE (ENCSR000ERO) suggest a possible binding of Jun in the promoter region of Stmn4 (ENCODE Project Consortium, 2012; Luo et al., 2020). STMN4 expression in hippocampus peaks around P8, a time when neurite outgrowth and synapse formation and pruning are occurring (Paolicelli et al., 2011). At the level of hippocampal tissue, loss of DLK causes no detectable changes to microtubules, while increased levels of DLK appear to alter microtubule homeostasis in dendrites, with generally increased levels of both stable and dynamic microtubule markers. The CA1 neurons in DLK(iOE) also show fewer parallel arrays of apical dendrites, with prominent microtubules in apical dendrites and short branches extending in varied directions. Our results from primary hippocampal neurons support roles for DLK in both

short neurite and axon formation, similar to observations in cortical neurons, where DLK contributes to stage specific regulation of microtubules (Hirai et al., 2011). In primary cortical neurons overexpression of STMN4 can increase neurite length and branching when an epigenetic cofactor regulating MT dynamics was knocked down (Tapias et al., 2021). We speculate that DLK dependent regulation of STMN4 or STMNs may have a critical role in the long-term cytoskeletal rearrangements, ultimately affecting neuronal morphology and synaptic connections.

Conserved roles of DLK in synapse formation and maintenance

The *in vivo* functions of the DLK family of proteins were first revealed in studies of synapse formation in *C. elegans* and Drosophila (Collins et al., 2006; Nakata et al., 2005). Our hippocampal glutamatergic neuron translatomic data extends this function by revealing a strong theme of DLK-dependent network in synapse organization, such as cell/synapse adhesion molecules and regulating of trans-synaptic signaling, especially related to AMPA receptor expression in the post-synapse and calcium signaling, such as changes in Neuronal Pentraxin 1 and Neuronal Pentraxin Receptor *Nptx1* and *Nptxr* (Gómez de San José et al., 2022). From our synapse analysis in culture, we find increased DLK alters expression of presynaptic protein Bassoon, consistent with the findings on *C. elegans* and Drosophila synapses (Nakata et al., 2005; Collins et al., 2006). We also find DLK regulates dendritic spine morphology, with loss of DLK associated with a greater number of spines and more mature spines, while increased DLK was associated with fewer and less mature spines. These results are similar to that observed in layer 2/3 cortical neurons where loss of DLK is associated with larger dendritic spines in developing neurons and higher density of spines when exposed to Aβ plaques, which lead to loss of nearby spines (Le Pichon et al., 2017; Pozniak et al., 2013). In CA1 dendritic regions, loss of DLK did not significantly impact synapse numbers, while increased DLK reduced synapse density. In axotomized spinal cord motor neurons DLK induces activation of complement, leading to microglial pruning of synapses in injured motoneurons (Asghari Adib et al., 2024). These data support a conserved role of DLK in synapse formation and maintenance, through regulating the translation of genes involved in neuron outgrowth, synaptic adhesion, and synapse activity.

Limitation of our study

Our data reveal specific roles of DLK in hippocampal glutamatergic neuron development, synapse formation, and neuron death processes. We find striking DLK-dependent translational differences in CA1 enriched genes, however, further studies will be required to dissect the mechanisms of how DLK dependent signaling interacts with other networks underlying hippocampal regional neuron vulnerability to pathological insults. Our analysis of spatial expression patterns of DLK-dependent genes relies on P56 adult animals, which may not reflect the patterns at P15, or in response to altered DLK. We cannot rule out that some of the decreased expression of CA1 enriched genes in DLK(iOE) could be secondary due to neuronal death that could result in fewer CA1 neurons present in our mRNA samples. The phenotype associated with STMN4 manipulation in primary cortical neurons is consistent with our observations of DLK-dependent morphology, though additional experiments will be needed to elucidate *in vivo* roles of STMN4 and its interaction with other STMNs. It is worth noting that a systematic analysis of gene networks in neuron types selectively vulnerable to Alzheimer's disease has suggested processes related to axon plasticity and synaptic vesicle transmission, particularly with relation to microtubule dynamics, may be involved in the neuronal vulnerability (Roussarie et al., 2020). Future efforts would be required to systematically profile specific cell types in hippocampus.

Acknowledgements

We thank members of our labs for their support and valuable discussion throughout this work. We are grateful to Emily Griffin for troubleshooting immunoprecipitation of ribosomes for RiboTag, to Brenda Bloodgood for advice with RNAscope experiments, Gentry Patrick and Lara Dozier for their guidance in primary hippocampal cultures, and Gareth Thomas for discussion and comments. This publication includes data generated at the UC San Diego IGM Genomics Center utilizing an Illumina NovaSeq 6000 that was purchased with funding from a National Institutes of Health SIG grant (#S10 OD026929). This work was partly supported by an Innovative Research Grant from the Kavli Institute for Brain and Mind (E.M.R.), and a generous gift fund from the Kavli Foundation and NS R35 127314 (Y. J.).

Author Contributions

Conceptualization, EMR and YJ; Methodology, EMR, YL, BZ, and YJ; Investigation, EMR, SZ, and QP; Resources, BZ and YJ; Writing- Original Draft, EMR and YJ; Writing- Review and Editing, EMR, SZ, YL, BZ, and YJ; Supervision, YJ; Funding Acquisition, EMR and YJ.

Declaration of Interests

The authors declare no competing interests.

Data and code availability

Sequencing datasets have been deposited in the Gene Expression Omnibus (Accession GSE266662).

Supplemental Materials: 11 Supplemental Figures, 1 Supplemental Table, 2 Supplemental files

Document S1. Supplemental methods, Figures S1-S11 and Table S1

File S1. Excel file containing DLK(cKO) differentially expressed genes

File S2. Excel file containing DLK(iOE) differentially expressed genes

Figure legends

Figure 1. Deletion of DLK in postmitotic glutamatergic neurons does not alter gross morphology of hippocampus.

(A) Western blot of DLK and β-actin from hippocampal tissue of *Vglut1*$^{Cre/+}$*;DLK(cKO)*$^{fl/fl}$ and *DLK(cKO)*$^{fl/fl}$ littermate controls (age P60, each lane representing protein sample from individual mice, N=3 mice/genotype). (B) Quantification of DLK protein level normalized to β-actin. Statistics: Unpaired t-test, *** P<0.001. (C) Confocal z-stack (max projection) images of coronal sections of the dorsal hippocampus immunostained for NeuN. Mice are P15 and P60, respectively. Dashed boxes in CA1 pyramidal layers are enlarged below. Scale bar: 1,000 μm in hippocampi; 100 μm in CA1 layer. (D) Quantification of CA1 pyramidal layer thickness in P15 and P60 mice. Each dot represents averaged thickness from 3 sections per mouse, N≥4 mice/genotype per stage. Statistics: Two-way ANOVA with Holm-Sidak multiple comparison test; ns, not significant. (E) Confocal z-stack images of hippocampus CA1, CA3, and DG regions immunostained with Tuj1 (age P60). Dashed outlines mark ROI (region of interest) for fluorescence intensity quantification. Scale bar: 100 μm. (F,G,H) Tuj1 mean fluorescence intensity (MFI) after thresholding signals in dendritic regions in each hippocampal area. N=4 control, and 5 *Vglut1*$^{Cre/+}$*;DLK(cKO)*$^{fl/fl}$ mice. Statistics: Unpaired t-test. ns, not significant.

Figure 2. Induced DLK overexpression in hippocampal glutamatergic neurons causes degeneration of CA1 neurons.

(A) Coronal sections from dorsal hippocampus of P10, P15, and P60 mice, stained for NeuN (shown as z-stack of max intensity projection). Dashed boxes mark CA1 pyramidal layers enlarged below. Scale bar: 1,000μm in hippocampi; 100μm in CA1 layer. (B) Quantification of CA1 pyramidal layer thickness. Data points represent averaged measurement from 3 sections per mouse, N≥4 mice/genotype at each stage. Statistics: Two-way ANOVA with Holm-Sidak multiple comparison test. ns, not significant; *** P<0.001; **** P<0.0001.

Figure 3: A select set of genes in hippocampal glutamatergic neurons show translation dependency on the expression levels of DLK.

(A) Volcano plot showing RiboTag analysis of gene expression in *Vglut1*$^{Cre/+;}$*H11-DLK*$^{iOE/+}$*;Rpl22*$^{HA/+}$ vs *Vglut1*$^{Cre/+}$*;Rpl22*$^{HA/+}$ (age P15). 260 genes showing differential expression with adjusted p-values < 0.05 are shown in red. Names of genes with p<1E-10 are labeled. (B) Volcano plot showing RiboTag analysis of genes in *Vglut1*$^{Cre/+}$*;DLK(cKO)*$^{fl/fl}$*;Rpl22*$^{HA/+}$ vs *Vglut1*$^{Cre/+}$*;Rpl22*$^{HA/+}$ (age P15). 36 genes showing differential expression with adjusted p-values < 0.05 are shown in blue. Names of genes with p<1E-10 are labeled. (C) Rank-rank hypergeometric overlap comparison of gene expression in DLK(iOE) and DLK(cKO) datasets shows enrichment of similar genes when DLK is low or high. Color represents the -log transformed hypergeometric p-values (blue=weaker p-value, red=stronger p-value). (D,E) Gene ontology (GO) analysis of significantly upregulated or downregulated genes, respectively, when DLK expression is increased in hippocampal glutamatergic neurons. Colors correspond to P-values. Circle size represents fold enrichment for the GO term, with number on X position showing # of significant genes included in the GO term. (F) SynGO sunburst plot shows significant enrichment for differentially expressed genes when DLK expression is increased in hippocampal glutamatergic neurons. (G,H) Pie charts show distribution of synaptic genes whose expression exhibits dependency when DLK expression is increased in hippocampus, based on *in situ* data in CA1, CA3, and DG in dorsal hippocampus (P56) in the Allen Mouse Brain Atlas.

Figure 4. *Stmn4* and microtubule homeostasis show dependency on the expression levels of DLK.

(A) RNAscope analysis of *Stmn4* and *Vglut1* mRNAs in hippocampal neurons. Dashed circle outlines single nuclei. Shown as single-slice confocal image; scale bar 10μm. (B,C) Quantification of the ratio of *Stmn4* to *Vglut1* RNAscope puncta in same nuclei of CA1 and CA3 neurons, respectively. N >50 cells per genotype, from 6,3,3 mice of respective genotype and 4 sections per mouse. Statistics: One way ANOVA with Dunnett's multiple comparison test, ns, not significant; ** P<0.01; **** P<0.0001. (D-F) Confocal images of immunostained CA1 sections for Tuj1, tyrosinated tubulin, and acetylated tubulin, respectively, in P15 control and *Vglut1*$^{Cre/+;}$*H11-DLK*$^{iOE/+}$ mice. SR denotes stratum radiatum region used for quantification. (G) Normalized tyrosinated tubulin mean fluorescence intensity (MFI) after thresholding signals in SR in CA1. N=9, 6 mice, 3 sections averaged per mouse. (H) Normalized acetylated tubulin MFI after thresholding signal in SR in CA1. N=6, 4 mice, 3 sections averaged per mouse. (I-K) Confocal images of immunostained CA1 sections for Tuj1, tyrosinated tubulin, and acetylated tubulin, respectively, in P60 control and *Vglut1*$^{Cre/+;}$*H11-DLK*$^{iOE/+}$ mice. (L) Normalized

tyrosinated tubulin MFI after thresholding signal in SR in CA1. N=9, 9 mice, 3 sections averaged per mouse. (M) Normalized acetylated tubulin MFI after thresholding signal in SR in CA1. N=6, 6 mice, 3 sections averaged per mouse. (N-P) Confocal images of immunostained CA1 sections for Tuj1, tyrosinated tubulin, and acetylated tubulin, respectively, in P60 control and *Vglut1*$^{Cre/+}$*;DLK(cKO)*$^{fl/fl}$ mice. (Q) Normalized tyrosinated tubulin MFI after thresholding signal in SRin CA1. N=5, 7 mice, 3 sections averaged per mouse. (M) Normalized acetylated tubulin MFI after thresholding signal in SR in CA1. N=6, 7 mice, 3 sections averaged per mouse. All tubulin images shown as maximum projection of z-stack, scale bar 10μm. Dashed lines outline pyramidal layer. Arrows point to apical dendrites with elevated signal; arrowheads point to thin neurites with elevated signal. Statistics: (G,H,L,M,Q,R) Unpaired t-test. ns, not significant; * P<0.05.

Figure 5. Hippocampal dorsal CA1 glutamatergic neurons show altered synapses when DLK expression is increased.

(A) Confocal images of Bassoon and Homer1 immunostaining in CA1 stratum radiatum (SR) of control and *Vglut1*$^{Cre/+}$*;DLK(cKO)*$^{fl/fl}$ mice at P60. (B-C) Quantification of Bassoon and Homer1 puncta density, respectively. (D) Quantification of synapses displaying co-localization of Bassoon and Homer1. Data points represent individual ROIs quantified from 5-6 images per mouse across 3 sections. N=7 control, and 8 *Vglut1*$^{Cre/+}$*;DLK(cKO)*$^{fl/fl}$ mice. (E) Confocal images of Bassoon and Homer1 immunostaining in CA1 SR of control and *Vglut1*$^{Cre/+}$*;H11-DLK*$^{iOE/+}$ mice at P15. (F-G) Quantification of Bassoon and Homer1 puncta density, respectively. (H) Quantification of synapses displaying co-localization of Bassoon and Homer1. All images shown as single slice; scale bars, 5μm in panel images, and 1μm in enlarged images. Data points represent individual ROIs quantified from 5-6 images per mouse across 3 sections, N=9 control, and 6 *Vglut1*$^{Cre/+}$*;H11-DLK*$^{iOE/+}$ mice. Statistics: unpaired t-test or Mann-Whitney U test if not passing normality. ns, not significant; *** P<0.001; **** P<0.0001.

Figure 6. DLK promotes short neurite formation in primary hippocampal neurons.

(A) Confocal images of DIV2 primary hippocampal neurons from genotypes indicated and immunostained with DLK and STMN4. tdTomato labeling of neurons is from Cre-dependent Rosa26-tdTomato. Red arrows point to some of the thin neurites from neurons with increased

DLK expression. Scale bar 10μm. (B) Quantification of STMN4 immunostaining integrated density (Area X MFI) in neuronal soma, relative to DLK integrated density. N≥3 cultures/genotype, ≥60 cells/genotype. Spearman correlation r=0.7454. (C) Quantification of neurons with no, one, or more than one axon in each genotype. Number of neurons: 47 from 3 Vglut1^{Cre} (control) cultures, 49 from 3 DLK(cKO) cultures, 42 from 4 DLK(iOE) cultures. Statistics: Fisher's exact test shows significance (P<0.0001) between the three genotypes and number of axons. Axon formation in control vs DLK(cKO): P=0.1857. Formation of multiple axons in control vs DLK(cKO): P>0.9999. Axon formation in control vs DLK(iOE): P=0.0042. Formation of multiple axons in control vs DLK(iOE): P=0.0001. (D) Quantification of number of primary neurites, which include both branches and filopodia, per neuron. Number of neurons: 55 from 4 Vglut1-cre (control) cultures, 70 from 4 DLK(cKO) cultures, 45 from 5 DLK(iOE) cultures. Statistics, Kruskal-Wallis test with Dunn's multiple comparison test. **** P<0.0001. (E) Confocal z-stack images show that neurons with high expression of DLK have filopodia structures (arrows) around the soma and on axons with tyrosinated tubulin, scale bar 10μm. (F) Confocal z-stack images show that neurons with high expression of DLK have filopodia structures (arrows) around the soma and on axons without acetylated tubulin, scale bar 10μm.

Figure 7. Increasing DLK expression alters synapse formation in primary hippocampal neurons.

(A) Confocal images of DIV14 neurons of indicated genotype, co-stained with Bassoon and DLK. (B) Quantification of bassoon puncta density. (C) Quantification of average bassoon puncta size from individual ROIs. Number of neurons: 30 from 3 Vglut1-cre (control) cultures, 41 from 3 DLK(cKO) cultures, 46 from 4 DLK(iOE) cultures. Statistics: One way ANOVA with Dunnett's multiple comparison test. ns, not significant; * P<0.05. (D) Confocal z-stack images of DIV14 neurons from *Vglut1*$^{Cre/+}$, *Vglut1*$^{Cre/+}$*;DLK(cKO)*$^{fl/fl}$, and *Vglut1*$^{Cre/+}$*;H11-DLK*$^{iOE/+}$, labeled by Rosa26-tdTomato. Lower panels show zoomed view of dendritic spines. Scale bar 10μm top, 5μm bottom. (E) Measurement of dendritic spine density. (F) Mushroom spine density. (G) Distribution of spine types. (E-G) Number of neurons: 35 from 3 Vglut1-cre (control) cultures, 31 from 3 DLK(cKO) cultures, 31 from 3 DLK(iOE) cultures. Statistics: One way ANOVA with Dunnett's multiple comparison test. * P<0.05; ** P<0.01.

Methods

EXPERIMENTAL MICE

All animal protocols were approved by the Animal Care and Use Committee of the University of California San Diego. Map3k12fl (*DLK(cKO)*$^{fl/fl}$) allele was reported in Chen et al., 2016 and made by Dr. Lawrence B. Holzman (Univ. Penn). Map3k12 (*H11-DLK*$^{iOE/+}$) transgene was described in Li et al., 2021. Vglut1^{Cre} mice line (JAX stock #023527) was described in Harris et al., 2014. RiboTag allele (JAX stock #029977) was described in Sanz et al., 2009. ROSA26-loxP-STOP-loxP-tdTomato fl/fl reporter line (JAX stock #007914) was constructed in Madisen et al., 2010. Standard mating procedure was followed to generated *Vglut1*$^{Cre/+}$*;DLK(cKO)*$^{fl/fl}$ and *Vglut1* $^{Cre/+}$*;H11-DLK*$^{iOE/+}$ experimental mice. Genotyping primers are in Supplemental table 1. Sibling control mice had either *Vglut1*$^{Cre/+}$ or the floxed alleles alone. All experiments used both male and female mice. *Vglut1* ^{Cre} dependent expression of *H11-DLK*$^{iOE/+}$ tdTomato reporter was observed to be expressed in most or all CA3, many CA1 neurons, with limited number of DG neurons at P15, similar to the described *Vglut1* ^{Cre} reporter line (Harris et al., 2014), and tdTomato was expressed throughout all regions by P60. *Vglut1* $^{Cre/+}$*;H11-DLK*$^{iOE/+}$ mice around 4 months of age developed noticeable progressive motor deficits, which were likely unrelated to hippocampal glutamatergic neuron death, and were not studied further.

WESTERN BLOTTING

Samples of brain tissue were lysed in ice-cold RIPA buffer (50mM Tris/HCl pH 7.4, 150mM NaCl, 0.5% DOC, 0.1% SDS, 1% NP-40 freshly supplemented with protease inhibitor cocktail and 1mM PMSF). Tissues were homogenized by Dounce homogenization using 30 passes pestle A and 30 passes pestle B. Samples were spun down at 13,000 x g for 10 min at 4C. Supernatants were collected, and protein concentration was determined using the BCA assay (Thermo Scientific, 23227). Equal concentration of proteins (~10-20ng) were run on NuPAGE™ 4-12% Bis-Tris Gel, 1.0 mm (Invitrogen, NP0322BOX) with 20X NuPAGE™ MES SDS Running Buffer (Invitrogen, NP0002). Protein samples were transferred to a PVDF membrane (0.2 µm, Bio-RAD, 1620177) by Mini Trans-Blot Cell at 100 mA for 1 hour at 4°C. Membranes were blocked in 5% skim milk in TBST for 1 hour at room temperature, and then incubated with primary antibody in 3% BSA or 5% skim milk in TBST at 4°C overnight. Membranes were washed 3 x 10 min in TBST and incubated with 1:5000 of the appropriate HRP-conjugated secondary antibody in 3% BSA in TBST at room temperature for 1hr, then washed 3 x 10 min in TBST. Bands were detected using enhanced chemiluminescence (ECL) reagents (GE

Healthcare, RPN2106) or Pico PLUS Chemiluminescent Substrate (Thermo Scientific, 34580) using a Licor Odyssey XF Imager. Molecular weight markers were PageRuler Plus Prestained Protein Ladder (Thermo Scientific, 26619) or Precision Plus Protein Ladder (Bio-Rad, 1610374).

Quantification of western blot images was performed by measuring identical size regions from each band, subtracting the background signal, and normalizing to internal actin controls for each sample. Time course analysis was further normalized to P1 WT protein levels. All images shown had N=3 biological replicates.

IMMUNOFLUORESCENCE OF HIPPOCAMPAL TISSUES

Mice were transcardially perfused with saline solution followed by 4% PFA in PBS. Brains were dissected and post-fixed overnight in 4% PFA at 4°C, then washed with PBS and transferred to 30% sucrose in PBS for at least three days. Brains were mounted coronally for cryosectioning in OCT Compound (Fisher HealthCare, 4585) on dry ice. Sections were cut to 25µm thickness, divided evenly among six wells, and stored in PBS with 0.01% sodium azide at 4°C until staining. For immunostaining, free floating sections were washed 3 times in 0.2% Triton X-100 in PBS, blocked for 1 hour at room temperature in 5% donkey serum in 0.4% Triton X-100 in PBS, then incubated with primary antibodies in 2% donkey serum in 0.4% Triton X-100 in PBS overnight at 4°C rocking. Following three washes with 0.2% Triton in PBS, sections were incubated with secondary antibodies in 2% donkey serum in 0.4% Triton X-100 in PBS for 1 hour at room temperature. Sections were again washed three times with 0.2% Triton X-100 in PBS, stained with DAPI for 10 min (14.3mM in PBS) and washed three times in PBS before mounting on glass slides using Prolong Diamond Antifade Mountant. TUNEL staining was performed using the DeadEnd Fluorometric TUNEL System (Promega, G3250) with a modified protocol as described previously (Li et al., 2021).

IMMUNOPRECIPITATION AND ISOLATION OF RIBOSOME ASSOCIATED mRNA

Immunoprecipitation of HA-tagged ribosomes was conducted following the protocol described in Sanz et al., 2019 (Sanz et al., 2019). Briefly, hippocampi from both hemispheres were dissected in ice cold PBS from mice of desired genotypes at postnatal day 15, and were stored at -80°C before further processing. Frozen tissues were homogenized by Dounce homogenization using 30 passes pestle A and 30 passes pestle B in 1.5mL homogenization buffer (50mM Tris, pH 7.5, 1% NP-40, 100mM KCl, 12mM $MgCl_2$, 100ug/mL cycloheximide, cOmplete EDTA-free protease inhibitor cocktail (Roche), 1mg/mL heparin, 200U/mL RNasin, 1mM DTT). Following centrifugation at 10,000 x g for 10 minutes at 4°C, 5µg anti-HA high affinity (Roche) were added

to the supernatant and incubated 4 hours rotating end-over-end at 4°C. The entire antibody-lysate solution was added to 400µl Protein G Dynabeads per sample overnight rotating end-over-end at 4°C. High salt buffer was prepared (50mM Tris, pH 7.5, 1% NP-40, 300mM KCl, 12mM $MgCl_2$, 100ug/mL cycloheximide, 0.5mM DTT), and beads were washed 3 x 10 minutes using a magnetic tube rack. During the final wash, samples were transferred to a new tube, and beads were eluted in 350µl of RLT buffer (from the Qiagen RNAeasy Minikit) supplemented with 1% β-mercaptoethanol. RNA was extracted following manufacturer's instructions in the RNAeasy Minikit (Qiagen). RNA integrity was measured using an Agilent TapeStation conducted at the IGM Genomics Center, University of California, San Diego, La Jolla, CA. All RNA for sequencing had RIN≥8.0, 28S/18S≥1.0.

To confirm immunoprecitipation in RiboTag IP samples, 10% of IP sample was isolated after final wash in high salt buffer. After removal of high salt buffer, protein was eluted in 2X RIPA buffer and 4x Laemmli Sample Buffer (Bio-Rad, 161–0747) by heating 10 min at 50°C. Beads were separated using a magnetic tube rack, the supernatant was isolated and beta-mercaptoethanol was added. Samples were boiled at 95°C for 10 min and centrifuged 5 min at 13,000 x g. Immunoprecipitated samples were separated by SDS-PAGE using Any kD Mini-PROTEAN TGX Precast Protein Gels (Bio-Rad, 4569034).

To ensure appropriate depletion of transcripts from non-Vglut1 expressing cells, we performed qRT-PCR analysis on representative marker genes for cell types in immunoprecipitated glutamatergic neuron RNA relative to whole hippocampal RNA. Briefly, RNAs isolated from whole hippocampi and immuoprecipitated from glutamatergic neurons were reverse transcribed to cDNA using Superscript III First Strand Synthesis System (Invitrogen, cat#18080051) following the manufacturer's protocol. 100ng RNA/sample was reverse transcribed with random hexamers. iQ Sybr Green Supermix (Bio-Rad, #1708880) was used for qPCR, and mRNA levels of marker genes (*Vglut1* (glutamatergic neurons), *Wfs1* (CA1 neurons), *Gfap* (Astrocytes), and *Vgat* (inhibitory neurons)) were normalized to *Gapdh* expression. Expression levels of qRT-PCR samples was analyzed using the CFX Real-Time PCR Detection System and CFX Manager Software (Bio-Rad). Relative enrichment of marker genes was evaluated using the comparative C_T method. All samples were run in triplicate. Primers for *Gapdh*, *Vglut1*, *Wfs1*, *Gfap*, and *Vgat* are from Furlanis et al., 2019 (see Supplemental table 1).

SEQUENCING

Library preparation and sequencing for ribosome associated mRNAs were performed by the UCSD IGM Genomics Center using Illumina Stranded mRNA Prep. Sequencing was performed on NovaSeq S4 with PE100 reads.

READ MAPPING

Following paired end RNA sequencing of isolated RNA, >24 million reads per sample were obtained (n=3DLK(iOE)/3WT, n=4 DLK(cKO)/4WT). The Galaxy platform was used for read mapping and differential expression analysis (Afgan et al., 2018). Read quality was checked using FastQC (version 0.11.8). Reads were mapped to the mouse reference genome (mm10) using STAR galaxy version 2.6.0b-1 with default settings (Dobin et al., 2013). Four DLK(cKO) and controls included 2 male and 2 female. For DLK(iOE), one female sample was removed from each genotype (control and DLK(iOE) due to read mapping variability/read quality, resulting in N=3 per genotype (2 male/1 female). Mapped reads were assigned to genes using featureCounts version 1.6.3 (Liao et al., 2014). High Pearson correlation (r > 0.99) was observed between all Vglut1$^{Cre/+}$;DLK(cKO)$^{fl/fl}$;Rpl22$^{HA/+}$ or Vglut1$^{Cre/+;}$Hipp11-DLK(iOE)/+;Rpl22$^{HA/+}$ samples and their respective littermate controls. Differential gene expression analysis was conducted using DESeq2 galaxy version 2.11.40.2 (Love et al., 2014) with genotype, sex, and batch included as factors in the analysis. Generation of volcano plots was performed in RStudio version 1.2.1335 using the ggplot2 package version 3.3.5 (Wickham, 2016). Heatmaps were generated using the heatmap.2 function on Galaxy (Galaxy version 3.0.1) using normalized gene counts with a log2 transformation and scaling by row.

GENE ONTOLOGY/PATHWAY ANALYSIS

Gene ontology analysis was performed using DAVID 2021 version (Huang et al., 2009) on genes found to be differentially expressed with $p<0.05$. For gene ontology and pathway analysis, background gene lists were generated by removing any gene with a base mean from DEseq2 normalization less than 1. *Gfap* was removed from GO and pathway analysis as a differentially expressed gene as it likely reflects a small amount of contamination from non-Vglut1 positive cells. DAVID analysis was performed using default thresholds, and Benjamini corrected p-values are reported. GO terms displayed in figures were chosen from top terms reaching significance related to biological processes or cellular components (BP5, CC4 or CC5) categories after filtering terms for semantic similarity. For SynGO analysis, mouse genes detected as differentially expressed were converted to human IDs using the ID conversion tool, and analysis was performed using the brain expressed background gene list provided by

SynGO (Koopmans et al., 2019) (Version/release 20210225). GSEA (4.2.2) (Subramanian et al., 2005) was used for pathway analysis based on expression data after filtering lowly expressed genes and ranking by log2 fold change. Pathway analysis used the canonical pathways gene list (ftp.broadinstitute.org://pub/gsea/gene_sets/c2.cp.v7.5.1.symbols.gmt) with 1000 permutations, collapse gene set, and permutation type gene set. All other settings used were default. Pathway visual was created using Cytoscape (version 3.9.1) (Shannon et al., 2003).

RANK RANK HYPERGEOMETRIC OVERLAP (RRHO) ANALYSIS FOR CORRELATION OF GENE EXPRESSION PATTERNS

We used Rank Rank Hypergeometric overlap (https://systems.crump.ucla.edu/rankrank/rankranksimple.php) to compare DLK(iOE) and DLK(cKO) translatome datasets (Plaisier et al., 2010). Input gene lists included 12740 genes which were expressed across all samples. For each gene, the -Log10P_{adj} was multiplied by the sign of the fold change to obtain the metric used for ranking. Both DLK(iOE) and DLK(cKO) datasets were ranked in order to have increasing DLK along the x and y axis. RRHO was run using a step size of 100 genes. The Benjamini-Yekutieli corrected graph is shown.

HIPPOCAMPAL SPATIAL EXPRESSION ANALYSIS

Gene expression patterns of differentially translated genes were evaluated using Allen Mouse Brain Atlas in situ data from P56 mice, and supplemented with data from Habib et al., 2016 through the Single cell portal from the Broad Institute or data from Zeisel et al., 2018, adolescent data through mousebrain.org when no in situ data was available or when expression was weak.

RNASCOPE ANALYSIS

The RNAscope Fluorescent Multiplex Reagent kit (Cat. #320850) Amp 4 Alt A-FL(Wang et al., 2012) with probes from Advanced Cell Diagnostics were used. The protocol was carried out under RNase-free conditions and following the manufacturer's instructions. Mice were anesthetized with isoflurane prior to decapitation. Brains were dissected immediately and flash frozen in OCT at -80°C. Fresh-frozen tissue was cryosectioned coronally to 20µm, collected on glass slides (Superfrost Plus), and stored at -80°C. Slides were fixed with 4% paraformaldehyde, dehydrated with 50% ethanol, 70% ethanol, and 2x washes in 100% ethanol for 5 min each at RT, followed by incubation in Protease IV reagent for 30 min at 40°C.

Hybridization with target probes was performed at 40°C for 2 hours in a humidified slide box in an incubator followed by wash and amplification steps according to the manufacturer's protocol. Finally, tissue was counterstained with DAPI, and mounted with Prolong diamond antifade mountant. All target probes were multiplexed with probes for *Vglut1* to label glutamatergic neurons.

PRIMARY HIPPOCAMPAL NEURON CULTURES AND IMMUNOSTAINING

Prior to preparing cultures, Poly-D-Lysine (Corning, Cat#354210) was coated on 12mm glass coverslips (0.2 mg/mL) or 6-well plates (0.05mg/ml) for two days at 37°C. Primary neurons were generated by isolating hippocampi from P1 mouse pups. Mice were rapidly decapitated, then brains were removed, placed into ice cold HBSS (calcium- and magnesium-free) supplemented with 10mM HEPES for removal of meninges and dissection of hippocampi (Kaech & Banker, 2006). Dissected hippocampi were dissociated in HBSS with HEPES in 0.25% trypsin for 15 minutes at 37°C. Hippocampi were then washed 3 times with 5ml of 20% Fetal bovine serum in HBSS. Cells were triturated in Opti-MEM supplemented with 20mM glucose by five passes with an unpolished glass pipette and five to ten passes using a fire polished glass pipette. Cells were counted using a hemocytometer, and 60,000 cells were plated per coverslip into a 24-well plate or 300,000 per well of a 6-well dish. Cultures were kept in an incubator at 37°C with 5% CO2. After four hours, plating media was replaced with prewarmed Neurobasal Medium supplemented with glutamine, penicillin/streptomycin, and B27. Cells were fixed after 48 hours (DIV2) or on DIV14 with prewarmed 4% PFA/4% sucrose in PBS for 20 min at room temperature followed by 3 washes with PBS. Media were changed carefully to minimize impacts to growth cone morphology.

Staining of fixed neurons was performed in 24-well plates. Coverslips were incubated in 50mM ammonium chloride for 10 min, followed by 3 washes PBS, 5 min 0.1% Triton X-100 in PBS, and blocking in 30mg/ml Bovine serum albumin (BSA) in 0.1% Triton in PBS for 30 min. Coverslips were incubated in primary antibody diluted in 30mg/ml BSA in 0.1% Triton in PBS according to antibody table for 90 minutes at room temperature followed by four washes in 0.1% Triton in PBS. Secondary antibodies were diluted in 30mg/ml BSA in 0.1% Triton in PBS with 1% donkey serum according to antibody table, and incubated for 60 minutes at room temperature. Finally, coverslips were washed three times in 0.2% Triton in PBS, stained with DAPI, washed three times with PBS, and mounted using Prolong Diamond Antifade Mountant.

CONFOCAL IMAGING AND QUANTIFICATION

Fluorescent images were acquired using a Zeiss LSM800 confocal microscope using a 10x, 20x, or 63x objective. All tissue sections and neurons within the same experiment were imaged under identical conditions. For brain tissue, three sections per mouse were imaged with a minimum of three mice per genotype for data analysis. Dorsal hippocampal images were taken from approximately bregma -1.5mm to -2.3mm. For image analysis, the quantification was performed blind to genotype or in an automated manner when possible. All image processing and analysis was performed using Fiji distribution of ImageJ unless otherwise specified (Schindelin et al., 2012).

For quantification of mRNA puncta, ROI were drawn to count puncta overlapping with nuclei of *Vglut1* positive cells. Individual puncta were counted from >50 cells per genotype in a blinded manner. Puncta counts were normalized to *Vglut1* puncta counts to control for variability in staining or preservation of RNA. Three to four sections per mouse were quantified and three mice per genotype were stained with each probe.

Pyramidal cell layer thickness was measured across CA1 by averaging the lengths of three perpendicular lines extending across the maximum projected z-stack of the pyramidal cell layer for each section. Three sections were averaged per mouse from dorsal hippocampus. For sections including ventral hippocampus, cell layer thickness of CA1 was measured using three lines either above the ventral edge of the suprapyramidal blade of dentate gyrus (Dong et al., 2009) for dorsal hippocampus (posterior) quantifications or below the ventral edge of the DG for ventral CA1 quantifications. Hippocampal cross-sectional area was measured by tracing outlines of CA1, CA3, or DG (including dendritic layers) in dorsal hippocampus sections.

Tuj1, tyrosinated tubulin, acetylated tubulin, and MAP2 intensities were measured using the mean gray value from auto thresholding (default) over stratum radiatum of CA1, the molecular layer of DG, or stratum lacunosum-moleculare, stratum radiatum, and stratum lucidum of CA3.

Staining of p-c-Jun in conditional knockout animals and c-Jun intensities were quantified from 20x images using mean gray values of ROIs for each brain slice cropped around the pyramidal cell or granule cell layers with background subtraction of non-nuclear signal from dendritic regions. Analysis of p-c-Jun positive nuclei in DLK(iOE) mice was counted from 10x images with cellpose 2.0 to segment nuclei positive for p-c-Jun signals using the following settings: diameter 15.5, flow threshold 0.4, cellprob threshold 2, stitch threshold 0, model zoo cyto. Data were normalized to the average value from control mice.

TUNEL positive signals were counted as fluorescent signals overlapping with the pyramidal cell or dentate granule cell layer in each region from 10x tile scan images of dorsal hippocampus. Z-stacks covering the entire section were max projected for quantification.

VGLUT1 (protein), Bassoon, and Homer1 puncta were quantified from stratum radiatum of dorsal CA1. Images were quantified using a single slice image, and a 25x25µm ROI was chosen to minimize absence of puncta due to cell bodies. A gaussian filter of 1 pixel was applied to the image. Background subtraction was performed using a rolling ball radius of 10 pixels, and an automated threshold was applied to the image using the Otsu method. Puncta larger than 2 pixels were counted for individual proteins. Overlap of Bassoon and Homer1 puncta of any size were counted. The number and average size of puncta were recorded from two images per brain section and three sections per mouse.

GFAP mean fluorescence intensity was quantified in a 312µm x 312µm box around the pyramidal cell or granule cell layers of CA1, CA3, and DG with background intensity subtracted after measuring from an area without GFAP signal.

Neurons were selected for neurite outgrowth and axon analysis after confirming DLK protein level by antibody staining and measurement of DLK fluorescence intensity in cell soma at DIV2. While we used tdTomato as a reporter for Vglut1 positive neurons, not all tdTomato positive neurons showed detectable differences in DLK levels at this early (DIV2) timepoint. Cell somas were outlined using tdTomato, and DLK integrated density was measured. Integrated density reflects the mean gray value multiplied by the area. Vglut1$^{Cre/+}$ control cells were selected for further analysis if DLK integrated density was 4,000-8,500. Cells from DLK(cKO) cultures with integrated density values of DLK less than 4,000 were selected for further analysis as “DLK(cKO)” and cells from DLK(iOE) with integrated density values of greater than 8,500 were selected for further analysis as “DLK(iOE)”. While we observed variably increased DLK signals in DLK(iOE) neurons from moderate to strong increases, all DLK(iOE) neurons with increased levels above the set threshold were grouped together in quantifications due to limited numbers of neurons. Primary neurites were counted in a blinded manner from tdTomato channel, counting both branches and filopodia originating from cell soma region. Neurites were considered as axons in axon specification analysis if longer than 90µm.

Bassoon puncta in cell culture were quantified from 20µm stretches of neurite. Regions for analysis were selected based on tdTomato positive signal on thin processes without dendritic spines exhibiting Bassoon signal, that was not in a region densely populated by Bassoon signal

from other neurites. DLK levels were also used to select ROIs. Signal from tdTomato was used to create a 10 pixel ROI along the neurite. Bassoon puncta were identified in a blinded manner by smoothing the image, applying a triangle threshold, and manually dividing merged puncta based on bassoon intensity. All puncta 5 pixels or larger and overlapping with tdTomato signal were analyzed for puncta size and density.

Dendritic spines were quantified from a 20µm countable and representative stretch of dendrite within 75µm of the neuron soma from one of the three largest dendrites. Spines density was counted using tdTomato signal, and calculated by counting total dendritic spines divided by the traced length of dendrite. Spines were manually categorized following measurements in Risher et al., 2014. Filopodia (>2µm) are not included in spine density counts. Spines were quantified from 3 independent cultures per genotype with 8-16 neurons per culture.

STASTICAL ANALYSIS

All statistical analysis shown in graphs was performed using GraphPad Prism 9.4.0. Points represent individual values, with bars reflecting mean values, and error bars plotting standard error of the mean (SEM).

Antibodies			
Reagent or resource	Source	Identifier	Additional information
Rabbit polyclonal anti-Map3k12 antibody	Genetex	GTX124127	IF 1:250 tissue, 1:1000 cells, WB 1:1000; Lot #40653
Rabbit monoclonal anti-p-c-Jun (Ser73) (D47G9) antibody	Cell signaling	3270	IF 1:200 tissue, 1:1000 cells; Lot #5
Rabbit polyclonal anti-GFAP antibody	Dako	Z0334	IF: 1:500; Lot #20049469
Rat monoclonal anti-HA High Affinity	Roche	11867423001	IP 5ug; Lot #47877600
Rabbit monoclonal anti-HA (C29F4)	Cell Signaling	3724	WB 1:1000; Lot #8
Mouse monoclonal anti-NeuN	Millipore	MAB377	IF 1:200; Lot #3104227/3808682
Mouse monoclonal anti-Tubb3 (Tuj1)	Biolegend	801202	IF 1:1000 tissue, 1:5000 cells; Lot #B249869
Rabbit polyclonal anti-Tubb3	Sigma-Aldrich	T2200	IF 1:500 cells; Lot #21190649
Mouse monoclonal anti-Acetyl-Tubulin (6-11b-1)	Sigma-Aldrich	T7451	IF 1:500 tissue, 1:3000 cells; WB 1:1000;
Mouse monoclonal anti-Stmn4	Santa Cruz Biotechnology	Sc-376936	IF 1:250 cells; WB 1:50; Lot # E3012
Rabbit polyclonal anti-Stmn4	Proteintech	12027-1-AP	IF 1:400 cells; WB 1:1000; Lot#00005750
Mouse monoclonal anti-Stmn2	R&D Systems	MAB6930	IF 1:1000 cells; WB 0.4ng/mL; Lot#CFIL052310A
Rabbit polyclonal anti-Stmn2	Proteintech	10586-1-AP	IF 1:400 cells; WB 1:2000; Lot#00124321
Mouse monoclonal anti-Tyrosinated Tubulin (TUB1A2)	Sigma-Aldrich	T9028	IF 1:1000 tissue, 1:5000 cells; WB 1:1000; Lot #22181017

Rabbit polyclonal anti-Vglut1	Synaptic Systems	135 302	IF 1:1000 tissue; Lot #1-53
Rabbit monoclonal anti-c-Jun (60A8)	Cell Signaling	9165	IF 1:200 tissue, 1:1000 cells; Lot #11
Mouse monoclonal anti-Bassoon (SAP7F407)	Novus	NB120-13249	IF 1:500 tissue, cells; Lot #06082117
Chicken polyclonal anti-MAP2	Abcam	Ab5392	IF 1:5,000 cells; Lot #1012833-1
Monoclonal mouse anti-beta actin	ABclonal	AC004	WB 1:5000; Lot #3500100012
Mouse monoclonal anti-Flag M2	Sigma-Aldrich	F1804	WB 1:500
Rabbit polyclonal anti-Homer1	Synaptic systems	160-003	IF 1:500 tissue
Alexafluor488 goat anti mouse IGG (H+L)	Invitrogen	A11001	IF 1:500 tissue, 1:2000 cells; Lot #745480
Alexafluor488 donkey anti mouse IGG (H+L)	Invitrogen	A21202	IF 1:500 tissue, 1:2000 cells; Lot #2266877
Alexafluor647 goat anti rabbit IGG (H+L)	Invitrogen	A21245	IF 1:500 tissue, 1:2000 cells; Lot #2299231
Alexafluor488 donkey anti rabbit IGG (H+L)	Invitrogen	A21206	IF 1:500 tissue, 1:2000 cells; Lot #2376850
Alexafluor647 goat anti mouse IGG (H+L)	Invitrogen	A21236	IF 1:500 tissue, 1:2000 cells; Lot #2300995
Alexa Fluor 647 goat anti chicken IgG (H+L)	Invitrogen	A21449	IF 1:2000 cells; Lot #2079903
Anti-rabbit: ECL Anti-Rabbit IgG, HRP	Cytiva	NA934V	WB 1:5000; Lot #17624274
Anti-mouse: ECL Anti-mouse IgG, HRP	Cytiva	NXA931V	WB 1:5000; Lot #17675041
Stabilized goat anti-rabbit HRP conjugated	Pierce	1858415	1:5000 WB; Lot # HE104909

Mice			
Reagent or resource	Source	Identifier	Additional information
Inducible DLK overexpression: Hipp11-DLK-iOE	Li et al., 2021		
Conditional DLK knockout (DLK-cKO)	Chen et al., 2016		
B6;129S-Slc17a7tm1.1(cre)Hze/J	The Jackson Laboratory	Strain #023527	Harris et al., 2014
B6J.129(Cg)-Rpl22tm1.1Psam/SjJ	The Jackson Laboratory	Strain #029977	Sanz et al., 2009
B6.Cg-Gt(ROSA)26Sortm14(CAG-tdTomato)Hze/J	The Jackson Laboratory	Strain #007914	Madisen et al., 2010

RNA probes		
Reagent or resource	Source	Identifier
RNAscope probe MAP3K12-C2	ACD	458151-C2
RNAscope probe Slc17a7-C3	ACD	416631-C3
RNAscope probe Gfap-C2	ACD	313211-C2
RNAscope probe Stmn4	ACD	537541

Other reagents		
Reagent or resource	Source	Identifier
DeadEnd Fluorometric TUNEL System	Promega	G3250
RNAeasy Minikit	Qiagen	74104
Superscript III First Strand Synthesis System	Invitrogen	18080051
iQ Sybr Green Supermix	Bio-Rad	1708880
Pierce™ BCA Protein Assay Kits	Thermo Scientific	23227
Protein G Dynabeads	Invitrogen	10003D
DAPI	Invitrogen	D1306
Prolong Diamond Antifade Mountant	Invitrogen	P36970
OCT Compound	Fisher HealthCare	4585
Laemmli Sample Buffer	Bio-Rad	161-0747

cOmplete EDTA-free Protease Inhibitor Cocktail	Roche	05056489001
Any kD Mini-PROTEAN TGX Precast Protein Gels	Bio-Rad	4569034
NuPAGE™ 4-12% Bis-Tris Gel, 1.0 mm	Invitrogen	NP0322BOX
20X NuPAGE™ MES SDS Running Buffer	Invitrogen	NP0002
0.2 µm PVDF membrane	Bio-Rad	1620177
Amersham ECL Western Blotting Detection Reagent	GE Healthcare	RPN2106
Super Signal West Pico PLUS Chemiluminescent Substrate	Thermo Scientific	34580
Restore™ Western Blot Stripping Buffer	Thermo Scientific	21059
HBSS	Gibco	14175-095
2.5% Trypsin	Gibco	15090-046
Opti-MEM Reduced Serum Medium	Gibco	31985-070
Neurobasal Medium	Gibco	21103-049
Penicillin-Streptomycin	Gibco	15070-063
12mm cover glasses	Carolina	633009
B27	Gibco	17504-044
Glutamine	Gibco	23050081
RNAse inhibitor, murine	New England Biolabs	M0314
Cycloheximide	Sigma-Aldrich	C4859

References

Afgan, E., Baker, D., Batut, B., van den Beek, M., Bouvier, D., Čech, M., … Blankenberg, D. (2018). The Galaxy platform for accessible, reproducible and collaborative biomedical analyses: 2018 update. *Nucleic Acids Research*, *46*(W1), W537–W544. Retrieved from http://dx.doi.org/10.1093/nar/gky379

Agrimi, G., Russo, A., Scarcia, P., & Palmieri, F. (2012). The human gene SLC25A17 encodes a peroxisomal transporter of coenzyme A, FAD and NAD+. *Biochemical Journal*, *443*(1), 241–247. https://doi.org/10.1042/BJ20111420

An integrated encyclopedia of DNA elements in the human genome. (2012). *Nature*, *489*(7414), 57–74. https://doi.org/10.1038/nature11247

Angel, P., Hattori, K., Smeal, T., & Karin, M. (1988). The jun proto-oncogene is positively autoregulated by its product, Jun/AP-1. *Cell*, *55*(5), 875–885. https://doi.org/https://doi.org/10.1016/0092-8674(88)90143-2

Asghari Adib, E., Shadrach, J. L., Reilly-Jankowiak, L., Dwivedi, M. K., Rogers, A. E., Shahzad, S., … Collins, C. A. (2024). DLK signaling in axotomized neurons triggers complement activation and loss of upstream synapses. *Cell Reports*, *43*(2), 113801. https://doi.org/10.1016/j.celrep.2024.113801

Asghari Adib, E., Smithson, L. J., & Collins, C. A. (2018). An axonal stress response pathway: degenerative and regenerative signaling by DLK. *Current Opinion in Neurobiology*, *53*, 110–119. https://doi.org/10.1016/j.conb.2018.07.002

Behrens, A., Sibilia, M., & Wagner, E. F. (1999). Amino-terminal phosphorylation of c-Jun regulates stress-induced apoptosis and cellular proliferation. *Nature Genetics*, *21*(3), 326–329. https://doi.org/10.1038/6854

Blondeau, A., Lucier, J. F., Matteau, D., Dumont, L., Rodrigue, S., Jacques, P. É., & Blouin, R. (2016). Dual leucine zipper kinase regulates expression of axon guidance genes in mouse neuronal cells. *Neural Development*, *11*(1), 1–12. https://doi.org/10.1186/s13064-016-0068-8

Blouin, R. (1996). Cell-specific expression of the ZPK gene in adult mouse tissues. *DNA and Cell Biology*, *15*(8), 631–642. https://doi.org/10.1089/dna.1996.15.631

Charbaut, E., Curmi, P. A., Ozon, S., Lachkar, S., Redeker, V., & Sobel, A. (2001). Stathmin Family Proteins Display Specific Molecular and Tubulin Binding Properties. *Journal of Biological Chemistry*, *276*(19), 16146–16154. https://doi.org/10.1074/jbc.M010637200

Chauvin, S., Poulain, F. E., Ozon, S., & Sobel, A. (2008). Palmitoylation of stathmin family proteins domain A controls Golgi versus mitochondrial subcellular targeting. *Biology of the Cell*, *100*(10), 577–591. https://doi.org/10.1042/bc20070119

Chauvin, S., & Sobel, A. (2015). Neuronal stathmins: A family of phosphoproteins cooperating for neuronal development, plasticity and regeneration. *Progress in Neurobiology*, *126*, 1–18. https://doi.org/10.1016/j.pneurobio.2014.09.002

Chen, M., Geoffroy, C. G., Wong, H. N., Tress, O., Nguyen, M. T., Holzman, L. B., … Zheng, B. (2016). Leucine Zipper-bearing Kinase promotes axon growth in mammalian central nervous system neurons. *Scientific Reports*, (February), 1–16. https://doi.org/10.1038/srep31482

Collins, C. A., Wairkar, Y. P., Johnson, S. L., & DiAntonio, A. (2006). Highwire Restrains Synaptic Growth by Attenuating a MAP Kinase Signal. *Neuron*, *51*(1), 57–69. https://doi.org/10.1016/j.neuron.2006.05.026

DeVault, L., Mateusiak, C., Palucki, J., Brent, M., Milbrandt, J., & DiAntonio, A. (2024). The response of Dual-leucine zipper kinase (DLK) to nocodazole: Evidence for a homeostatic cytoskeletal repair mechanism. *PLOS ONE*, *19*(4), e0300539. Retrieved from https://doi.org/10.1371/journal.pone.0300539

Dobin, A., Davis, C. A., Schlesinger, F., Drenkow, J., Zaleski, C., Jha, S., … Gingeras, T. R. (2013). STAR: Ultrafast universal RNA-seq aligner. *Bioinformatics*, *29*(1), 15–21. https://doi.org/10.1093/bioinformatics/bts635

Dodelet, V. C., Pazzagli, C., Zisch, A. H., Hauser, C. A., & Pasquale, E. B. (1999). A Novel Signaling Intermediate, SHEP1, Directly Couples Eph Receptors to R-Ras and Rap1A *. *Journal of Biological Chemistry*, *274*(45), 31941–31946. https://doi.org/10.1074/jbc.274.45.31941

Dong, H. W., Swanson, L. W., Chen, L., Fanselow, M. S., & Toga, A. W. (2009). Genomic-anatomic evidence for distinct functional domains in hippocampal field CA1. *Proceedings of the National Academy of Sciences of the United States of America*, *106*(28), 11794–11799. https://doi.org/10.1073/pnas.0812608106

Dotti, C. G., Sullivan, C. A., & Banker, G. A. (1988). The establishment of polarity by hippocampal neurons in culture. *The Journal of Neuroscience*, *8*(4), 1454 LP – 1468. https://doi.org/10.1523/JNEUROSCI.08-04-01454.1988

Eilers, A., Whitfield, J., Babij, C., Rubin, L. L., & Ham, J. (1998). Role of the Jun Kinase Pathway in the Regulation of c-Jun Expression and Apoptosis in Sympathetic Neurons. *The Journal of Neuroscience*, *18*(5), 1713 LP – 1724. https://doi.org/10.1523/JNEUROSCI.18-05-01713.1998

Furlanis, E., Traunmüller, L., Fucile, G., & Scheiffele, P. (2019). Landscape of ribosome-engaged transcript isoforms reveals extensive neuronal-cell-class-specific alternative splicing programs. *Nature Neuroscience*, *22*(10), 1709–1717. https://doi.org/10.1038/s41593-019-0465-5

Gavet, O., Messari, S. El, Ozon, S., & Sobel, A. (2002). Regulation and subcellular localization of the microtubule-destabilizing stathmin family phosphoproteins in cortical neurons. *Journal of Neuroscience Research*, *68*(5), 535–550. https://doi.org/10.1002/jnr.10234

Ghosh, A. S., Wang, B., Pozniak, C. D., Chen, M., Watts, R. J., & Lewcock, J. W. (2011). DLK induces developmental neuronal degeneration via selective regulation of proapoptotic JNK activity. *The Journal of Cell Biology*, *194*(5), 751–764. https://doi.org/10.1083/jcb.201103153

Gómez de San José, N., Massa, F., Halbgebauer, S., Oeckl, P., Steinacker, P., & Otto, M. (2022). Neuronal pentraxins as biomarkers of synaptic activity: from physiological functions to pathological changes in neurodegeneration. *Journal of Neural Transmission*, *129*(2), 207–230. https://doi.org/10.1007/s00702-021-02411-2

Goodwani, S., Fernandez, C., Acton, P. J., Buggia-Prevot, V., McReynolds, M. L., Ma, J., … Ray, W. J. (2020). Dual leucine zipper kinase is constitutively active in the adult mouse brain and has both stress-induced and homeostatic functions. *International Journal of Molecular Sciences*, *21*(14), 1–24. https://doi.org/10.3390/ijms21144849

Habib, N., Li, Y., Heidenreich, M., Swiech, L., Avraham-Davidi, I., Trombetta, J. J., … Regev, A. (2016). Div-Seq: Single-nucleus RNA-Seq reveals dynamics of rare adult newborn neurons. *Science*, *353*(6302), 925–928. https://doi.org/10.1126/science.aad7038

Hahn, O., Foltz, A. G., Atkins, M., Kedir, B., Moran-Losada, P., Guldner, I. H., … Wyss-Coray, T. (2023). Atlas of the aging mouse brain reveals white matter as vulnerable foci. *Cell*, *186*(19), 4117-4133.e22. https://doi.org/https://doi.org/10.1016/j.cell.2023.07.027

Harris, J. A., Hirokawa, K. E., Sorensen, S. A., Gu, H., Mills, M., Ng, L. L., … Zeng, H. (2014). Anatomical characterization of Cre driver mice for neural circuit mapping and manipulation. *Frontiers in Neural Circuits*, *8*, 76. https://doi.org/10.3389/fncir.2014.00076

Hirai, S., Cui, D. F., Miyata, T., Ogawa, M., Kiyonari, H., Suda, Y., … Ohno, S. (2006). The c-Jun N-Terminal Kinase Activator Dual Leucine Zipper Kinase Regulates Axon Growth and Neuronal Migration in the Developing Cerebral Cortex. *The Journal of Neuroscience*, *26*(46), 11992–12002. https://doi.org/10.1523/JNEUROSCI.2272-06.2006

Hirai, S. I., Banba, Y., Satake, T., & Ohno, S. (2011). Axon formation in neocortical neurons depends on stage-specific regulation of microtubule stability by the dual leucine zipper kinase-c-jun N-terminal kinase pathway. *Journal of Neuroscience*, *31*(17), 6468–6480. https://doi.org/10.1523/JNEUROSCI.5038-10.2011

Hirai, S. I., Kawaguchi, A., Hirasawa, R., Baba, M., Ohnishi, T., & Ohno, S. (2002). MAPK-upstream protein kinase (MUK) regulates the radial migration of immature neurons in telencephalon of mouse embryo. *Development*, *129*(19), 4483–4495. https://doi.org/10.1242/dev.129.19.4483

Hirai, S. I., Kawaguchi, A., Suenaga, J., Ono, M., Cui, D. F., & Ohno, S. (2005). Expression of MUK/DLK/ZPK, an activator of the JNK pathway, in the nervous systems of the developing mouse embryo. *Gene Expression Patterns*, *5*(4), 517–523. https://doi.org/10.1016/j.modgep.2004.12.002

Holland, S. M., Collura, K. M., Ketschek, A., Noma, K., Ferguson, T. A., Jin, Y., … Thomas, G. M. (2016). Palmitoylation controls DLK localization, interactions and activity to ensure effective axonal injury signaling. *Proceedings of the National Academy of Sciences of the United States of America*, *113*(3), 763–768. https://doi.org/10.1073/pnas.1514123113

Hu, Z., Deng, N., Liu, K., & Zeng, W. (2019). DLK mediates the neuronal intrinsic immune response and regulates glial reaction and neuropathic pain. *Experimental Neurology*, *322*(August), 113056. https://doi.org/10.1016/j.expneurol.2019.113056

Huang, D. W., Sherman, B. T., & Lempicki, R. A. (2009). Systematic and integrative analysis of large gene lists using DAVID bioinformatics resources. *Nature Protocols*, *4*(1), 44–57. https://doi.org/10.1038/nprot.2008.211

Huang, Y. W. A., Zhou, B., Wernig, M., & Südhof, T. C. (2017). ApoE2, ApoE3, and ApoE4 Differentially Stimulate APP Transcription and Aβ Secretion. *Cell*, *168*(3), 427-441.e21. https://doi.org/10.1016/j.cell.2016.12.044

Huntwork-Rodriguez, S., Wang, B., Watkins, T., Ghosh, A. S., Pozniak, C. D., Bustos, D., … Lewcock, J. W. (2013). JNK-mediated phosphorylation of DLK suppresses its ubiquitination to promote neuronal apoptosis. *Journal of Cell Biology*, *202*(5), 747–763. https://doi.org/10.1083/jcb.201303066

Itoh, A., Horiuchi, M., Bannerman, P., Pleasure, D., & Itoh, T. (2009). Impaired regenerative

response of primary sensory neurons in ZPK/DLK gene-trap mice. *Biochemical and Biophysical Research Communications*, *383*(2), 258–262. https://doi.org/10.1016/j.bbrc.2009.04.009

Itoh, A., Horiuchi, M., Wakayama, K., Xu, J., Bannerman, P., Pleasure, D., & Itoh, T. (2011). ZPK/DLK, a mitogen-activated protein kinase kinase kinase, is a critical mediator of programmed cell death of motoneurons. *Journal of Neuroscience*, *31*(20), 7223–7228. https://doi.org/10.1523/JNEUROSCI.5947-10.2011

Janke, C., & Magiera, M. M. (2020). The tubulin code and its role in controlling microtubule properties and functions. *Nature Reviews Molecular Cell Biology*, *21*(6), 307–326. https://doi.org/10.1038/s41580-020-0214-3

Jin, Y., & Zheng, B. (2019). Multitasking : Dual Leucine Zipper – Bearing Kinases in Neuronal Development and Stress Management. *Annual Review of Cell and Developmental Biology*, 501–522.

Joy, M. T., Ben Assayag, E., Shabashov-Stone, D., Liraz-Zaltsman, S., Mazzitelli, J., Arenas, M., … Carmichael, S. T. (2019). CCR5 Is a Therapeutic Target for Recovery after Stroke and Traumatic Brain Injury. *Cell*, *176*(5), 1143-1157.e13. https://doi.org/10.1016/j.cell.2019.01.044

Kaech, S., & Banker, G. (2006). Culturing hippocampal neurons. *Nature Protocols*, *1*(5), 2406–2415. https://doi.org/10.1038/nprot.2006.356

Koopmans, F., van Nierop, P., Andres-Alonso, M., Byrnes, A., Cijsouw, T., Coba, M. P., … Verhage, M. (2019). SynGO: An Evidence-Based, Expert-Curated Knowledge Base for the Synapse. *Neuron*, *103*(2), 217-234.e4. https://doi.org/10.1016/j.neuron.2019.05.002

Larhammar, M., Huntwork-Rodriguez, S., Jiang, Z., Solanoy, H., Ghosh, A. S., Wang, B., … Watkins, T. A. (2017). Dual leucine zipper kinase-dependent PERK activation contributes to neuronal degeneration following insult. *ELife*, *6*, 1–27. https://doi.org/10.7554/eLife.20725

Le Pichon, C. E., Meilandt, W. J., Dominguez, S., Solanoy, H., Lin, H., Ngu, H., … Lewcock, J. W. (2017). Loss of dual leucine zipper kinase signaling is protective in animal models of neurodegenerative disease. *Science Translational Medicine*, *9*(403). https://doi.org/10.1126/scitranslmed.aag0394

Lein, E. S., Hawrylycz, M. J., Ao, N., Ayres, M., Bensinger, A., Bernard, A., … Jones, A. R. (2007). Genome-wide atlas of gene expression in the adult mouse brain. *Nature*, *445*(7124), 168–176. https://doi.org/10.1038/nature05453

Lein, E. S., Zhao, X., & Gage, F. H. (2004). Defining a Molecular Atlas of the Hippocampus Using DNA Microarrays and High-Throughput In Situ Hybridization. *The Journal of Neuroscience*, *24*(15), 3879 LP – 3889. https://doi.org/10.1523/JNEUROSCI.4710-03.2004

Lewcock, J. W., Genoud, N., Lettieri, K., & Pfaff, S. L. (2007). The Ubiquitin Ligase Phr1 Regulates Axon Outgrowth through Modulation of Microtubule Dynamics. *Neuron*, *56*(4), 604–620. https://doi.org/10.1016/j.neuron.2007.09.009

Li, Y., Ritchie, E. M., Steinke, C. L., Qi, C., Chen, L., Zheng, B., & Jin, Y. (2021). Activation of MAP3K DLK and LZK in Purkinje cells causes rapid and slow degeneration depending on signaling strength. *ELife*, *10*, e63509. https://doi.org/10.7554/eLife.63509

Liao, Y., Smyth, G. K., & Shi, W. (2014). FeatureCounts: An efficient general purpose program for assigning sequence reads to genomic features. *Bioinformatics*, *30*(7), 923–930. https://doi.org/10.1093/bioinformatics/btt656

Love, M. I., Huber, W., & Anders, S. (2014). Moderated estimation of fold change and dispersion for RNA-seq data with DESeq2. *Genome Biology*, *15*(12), 550. https://doi.org/10.1186/s13059-014-0550-8

Luo, Y., Hitz, B. C., Gabdank, I., Hilton, J. A., Kagda, M. S., Lam, B., … Cherry, J. M. (2020). New developments on the Encyclopedia of DNA Elements (ENCODE) data portal. *Nucleic Acids Research*, *48*(D1), D882–D889. https://doi.org/10.1093/nar/gkz1062

Lutjens, R., Igarashi, M., Pellier, V., Blasey, H., Di Paolo, G., Ruchti, E., … Grenningloh, G. (2000). Localization and targeting of SCG10 to the trans-Golgi apparatus and growth cone vesicles. *European Journal of Neuroscience*, *12*(7), 2224–2234. https://doi.org/https://doi.org/10.1046/j.1460-9568.2000.00112.x

Madisen, L., Zwingman, T. A., Sunkin, S. M., Oh, S. W., Zariwala, H. A., Gu, H., … Zeng, H. (2010). A robust and high-throughput Cre reporting and characterization system for the whole mouse brain. *Nature Neuroscience*, *13*(1), 133–140. https://doi.org/10.1038/nn.2467

Mata, M., Merritt, S. E., Fan, G., Yu, G. G., & Holzman, L. B. (1996). Characterization of dual leucine zipper-bearing kinase, a mixed lineage kinase present in synaptic terminals whose phosphorylation state is regulated by membrane depolarization via calcineurin. *Journal of Biological Chemistry*, *271*(28), 16888–16896. https://doi.org/10.1074/jbc.271.28.16888

Mielke, K., Brecht, S., Dorst, A., & Herdegen, T. (1999). Activity and expression of JNK1, p38 and ERK kinases, c-Jun N-terminal phosphorylation, and c-jun promoter binding in the adult rat brain following kainate-induced seizures. *Neuroscience*, *91*(2), 471–483. https://doi.org/https://doi.org/10.1016/S0306-4522(98)00667-8

Nakata, K., Abrams, B., Grill, B., Goncharov, A., Huang, X., Chisholm, A. D., & Jin, Y. (2005). Regulation of a DLK-1 and p38 MAP kinase pathway by the ubiquitin ligase RPM-1 is required for presynaptic development. *Cell*, *120*(3), 407–420. https://doi.org/10.1016/j.cell.2004.12.017

Paolicelli, R. C., Bolasco, G., Pagani, F., Maggi, L., Scianni, M., Panzanelli, P., … Gross, C. T. (2011). Synaptic Pruning by Microglia Is Necessary for Normal Brain Development. *Science*, *333*(6048), 1456–1458. https://doi.org/10.1126/science.1202529

Plaisier, S. B., Taschereau, R., Wong, J. A., & Graeber, T. G. (2010). Rank–rank hypergeometric overlap: identification of statistically significant overlap between gene-expression signatures. *Nucleic Acids Research*, *38*(17), e169–e169. https://doi.org/10.1093/nar/gkq636

Pozniak, C. D., Ghosh, A. S., Gogineni, A., Hanson, J. E., Lee, S., Larson, J. L., … Lewcock, J. W. (2013). Dual leucine zipper kinase is required for excitotoxicity-induced neuronal degeneration. *The Journal of Experimental Medicine*, *210*(12), 2553–2567. https://doi.org/10.1084/jem.20122832

Risher, W. C., Ustunkaya, T., Singh Alvarado, J., & Eroglu, C. (2014). Rapid Golgi Analysis Method for Efficient and Unbiased Classification of Dendritic Spines. *PLOS ONE*, *9*(9), e107591. Retrieved from https://doi.org/10.1371/journal.pone.0107591

Roussarie, J.-P., Yao, V., Rodriguez-Rodriguez, P., Oughtred, R., Rust, J., Plautz, Z., …

Greengard, P. (2020). Selective Neuronal Vulnerability in Alzheimer's Disease: A Network-Based Analysis. *Neuron*, *107*(5), 821-835.e12. https://doi.org/https://doi.org/10.1016/j.neuron.2020.06.010

Saikia, J. M., Chavez-Martinez, C. L., Kim, N. D., Allibhoy, S., Kim, H. J., Simonyan, L., … Zheng, B. (2022). A Critical Role for DLK and LZK in Axonal Repair in the Mammalian Spinal Cord. *Journal of Neuroscience*, *42*(18), 3716–3732. https://doi.org/10.1523/JNEUROSCI.2495-21.2022

Sanz, E., Bean, J. C., Carey, D. P., Quintana, A., & McKnight, G. S. (2019). RiboTag: Ribosomal Tagging Strategy to Analyze Cell-Type-Specific mRNA Expression In Vivo. *Current Protocols in Neuroscience*, *88*(1), e77. https://doi.org/https://doi.org/10.1002/cpns.77

Sanz, E., Yang, L., Su, T., Morris, D. R., McKnight, G. S., & Amieux, P. S. (2009). Cell-type-specific isolation of ribosome-associated mRNA from complex tissues. *Proceedings of the National Academy of Sciences of the United States of America*, *106*(33), 13939–13944. https://doi.org/10.1073/pnas.0907143106

Schindelin, J., Arganda-Carreras, I., Frise, E., Kaynig, V., Longair, M., Pietzsch, T., … Cardona, A. (2012). Fiji: an open-source platform for biological-image analysis. *Nature Methods*, *9*(7), 676–682. https://doi.org/10.1038/nmeth.2019

Schmidt-Kastner, R. (2015). Genomic approach to selective vulnerability of the hippocampus in brain ischemia-hypoxia. *Neuroscience*, *309*, 259–279. https://doi.org/10.1016/j.neuroscience.2015.08.034

Shannon, P., Markiel, A., Ozier, O., Baliga, N. S., Wang, J. T., Ramage, D., … Ideker, T. (2003). Cytoscape: A Software Environment for Integrated Models of Biomolecular Interaction Networks. *Genome Research* , *13*(11), 2498–2504. https://doi.org/10.1101/gr.1239303

Shin, J. E., Cho, Y., Beirowski, B., Milbrandt, J., Cavalli, V., & DiAntonio, A. (2012). Dual Leucine Zipper Kinase Is Required for Retrograde Injury Signaling and Axonal Regeneration. *Neuron*, *74*(6), 1015–1022. https://doi.org/10.1016/j.neuron.2012.04.028

Shin, J. E., Ha, H., Cho, Y., Kim, Y. K., & DiAntonio, A. (2019). DLK regulates a distinctive transcriptional regeneration program after peripheral nerve injury. *Neurobiology of Disease*, #pagerange#. https://doi.org/10.1016/j.nbd.2019.02.001

Smith, M.-L., Auer, R. N., & Siesjö, B. K. (1984). The density and distribution of ischemic brain injury in the rat following 2–10 min of forebrain ischemia. *Acta Neuropathologica*, *64*(4), 319–332. https://doi.org/10.1007/BF00690397

Somasundaram, P., Farley, M. M., Rudy, M. A., Stefanoff, D. G., Shah, M., Goli, P., … Watkins, T. A. (2023). *Coordinated stimulation of axon regenerative and neurodegenerative transcriptional programs by Atf4 following optic nerve injury*. https://doi.org/10.1101/2023.03.29.534798

Subramanian, A., Tamayo, P., Mootha, V. K., Mukherjee, S., Ebert, B. L., Gillette, M. A., … Mesirov, J. P. (2005). Gene set enrichment analysis: A knowledge-based approach for interpreting genome-wide expression profiles. *Proceedings of the National Academy of Sciences*, *102*(43), 15545–15550. https://doi.org/10.1073/pnas.0506580102

Summers, D. W., Frey, E., Walker, L. J., Milbrandt, J., & DiAntonio, A. (2020). DLK Activation Synergizes with Mitochondrial Dysfunction to Downregulate Axon Survival Factors and

Promote SARM1-Dependent Axon Degeneration. *Molecular Neurobiology*, *57*(2), 1146–1158. https://doi.org/10.1007/s12035-019-01796-2

Tapias, A., Lázaro, D., Yin, B. K., Rasa, S. M. M., Krepelova, A., Sacramento, E. K., … Wang, Z. Q. (2021). Hat cofactor trrap modulates microtubule dynamics via sp1 signaling to prevent neurodegeneration. *ELife*, *10*, 1–64. https://doi.org/10.7554/eLife.61531

Tedeschi, A., & Bradke, F. (2013). The DLK signalling pathway—a double-edged sword in neural development and regeneration. *EMBO Reports*, *14*(6), 605–614. https://doi.org/10.1038/embor.2013.64

Thornburg-Suresh, E. J. C., Richardson, J. E., & Summers, D. W. (2023). The Stathmin-2 membrane-targeting domain is required for axon protection and regulated degradation by DLK signaling. *Journal of Biological Chemistry*, *299*(7), 1–16. https://doi.org/10.1016/j.jbc.2023.104861

Tortosa, E., Sengupta Ghosh, A., Li, Q., Wong, W. R., Hinkle, T., Sandoval, W., … Hoogenraad, C. C. (2022). Stress-induced vesicular assemblies of dual leucine zipper kinase are signaling hubs involved in kinase activation and neurodegeneration. *The EMBO Journal*, *41*(14), 1–20. https://doi.org/10.15252/embj.2021110155

Vervoort, V. S., Roselli, S., Oshima, R. G., & Pasquale, E. B. (2007). Splice variants and expression patterns of SHEP1, BCAR3 and NSP1, a gene family involved in integrin and receptor tyrosine kinase signaling. *Gene*, *391*(1), 161–170. https://doi.org/https://doi.org/10.1016/j.gene.2006.12.016

Viana da Silva, S., Haberl, M. G., Gaur, K., Patel, R., Narayan, G., Ledakis, M., … Leutgeb, S. (2024). Localized APP expression results in progressive network dysfunction by disorganizing spike timing. *Neuron*, *112*(1), 124-140.e6. https://doi.org/https://doi.org/10.1016/j.neuron.2023.10.001

Vornov, J. J., Tasker, R. C., & Coyle, J. T. (1991). Direct observation of the agonist-specific regional vulnerability to glutamate, NMDA, and kainate neurotoxicity in organotypic hippocampal cultures. *Experimental Neurology*, *114*(1), 11–22. https://doi.org/https://doi.org/10.1016/0014-4886(91)90079-R

Wang, F., Flanagan, J., Su, N., Wang, L. C., Bui, S., Nielson, A., … Luo, Y. (2012). RNAscope: A novel in situ RNA analysis platform for formalin-fixed, paraffin-embedded tissues. *Journal of Molecular Diagnostics*, *14*(1), 22–29. https://doi.org/10.1016/j.jmoldx.2011.08.002

Watkins, T. A., Wang, B., Huntwork-Rodriguez, S., Yang, J., Jiang, Z., Eastham-Anderson, J., … Lewcock, J. W. (2013). DLK initiates a transcriptional program that couples apoptotic and regenerative responses to axonal injury. *PNAS*, *110*(10), 4039–4044. https://doi.org/10.1073/pnas.1211074110

Welsbie, D. S., Mitchell, K. L., Jaskula-ranga, V., Sluch, V. M., Yang, Z., Kim, J., … Zack, D. J. (2017). Enhanced Functional Genomic Screening Identifies Novel Mediators of Dual Leucine Zipper Kinase- Dependent Injury Signaling in Neurons. *Neuron*, *94*, 1142–1154. https://doi.org/10.1016/j.neuron.2017.06.008

West, M. J., Coleman, P. D., Flood, D. G., & Troncoso, J. C. (1994). Differences in the pattern of hippocampal neuronal loss in normal ageing and Alzheimer's disease. *The Lancet*, *344*(8925), 769–772. https://doi.org/https://doi.org/10.1016/S0140-6736(94)92338-8

Wickham, H. (2016). *Ggplot2: Elegant graphics for data analysis* (2nd ed.). Cham, Switzerland:

Springer International Publishing.

Wilde, G. J. C., Pringle, A. K., Wright, P., & Iannotti, F. (1997). Differential Vulnerability of the CA1 and CA3 Subfields of the Hippocampus to Superoxide and Hydroxyl Radicals In Vitro. *Journal of Neurochemistry*, *69*(2), 883–886. https://doi.org/https://doi.org/10.1046/j.1471-4159.1997.69020883.x

Yoshihara, Y., De Roo, M., & Muller, D. (2009). Dendritic spine formation and stabilization. *Current Opinion in Neurobiology*, *19*(2), 146–153. https://doi.org/https://doi.org/10.1016/j.conb.2009.05.013

Zeisel, A., Hochgerner, H., Lönnerberg, P., Johnsson, A., Memic, F., van der Zwan, J., … Linnarsson, S. (2018). Molecular Architecture of the Mouse Nervous System. *Cell*, *174*(4), 999-1014.e22. https://doi.org/https://doi.org/10.1016/j.cell.2018.06.021

Figure 1

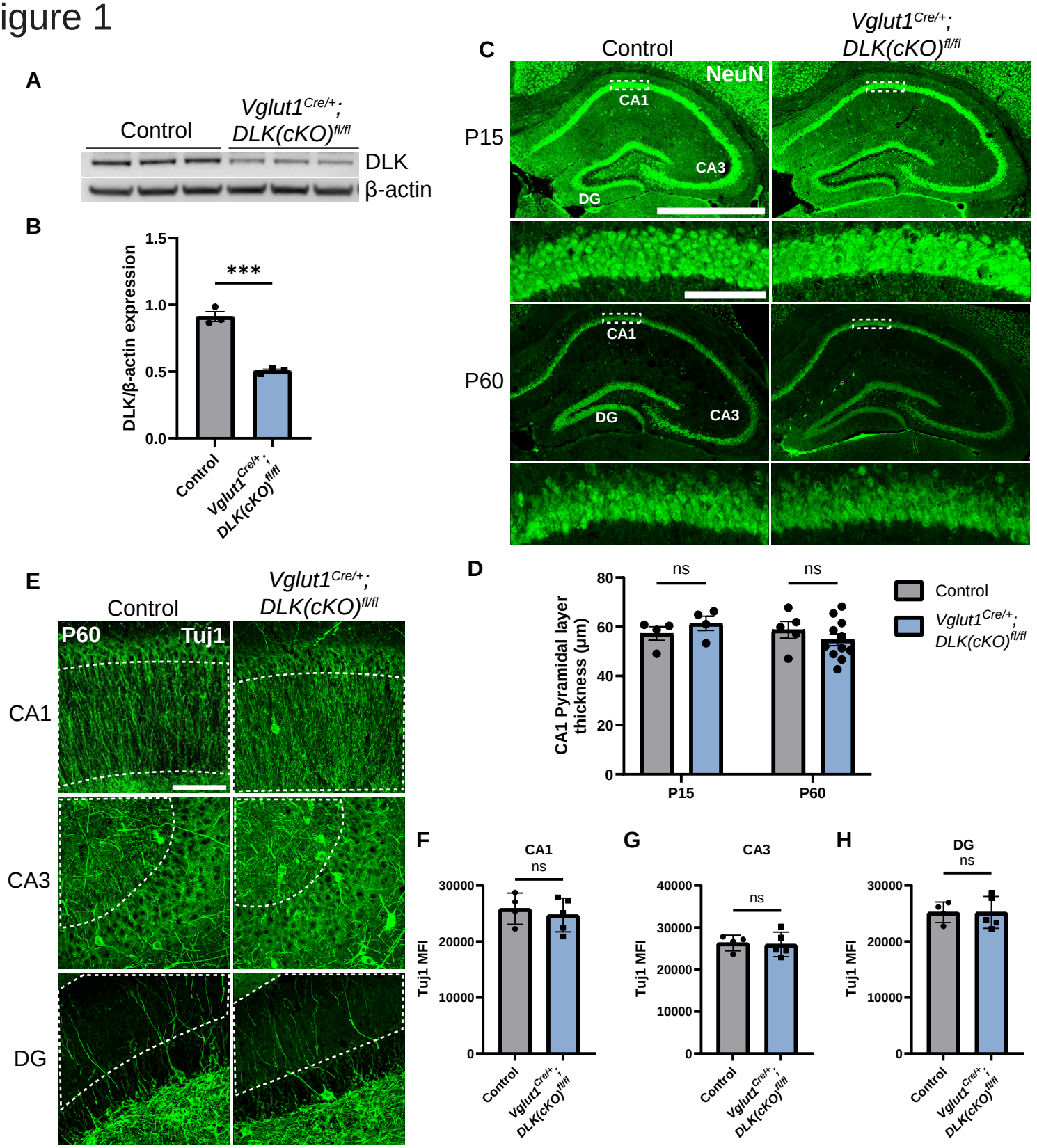
A
Control
Vglut1Cre/+; DLK(cKO)fl/fl
DLK
β-actin
B
DLK/β-actin expression
1.5
1.0
0.5
0.0
***
Control
Vglut1Cre/+; DLK(cKO)fl/fl
C
Control
Vglut1Cre/+; DLK(cKO)fl/fl
NeuN
P15
P60
CA1
CA3
DG
D
CA1 Pyramidal layer thickness (μm)
80
60
40
20
0
ns
ns
P15
P60
Control
Vglut1Cre/+; DLK(cKO)fl/fl
E
Control
Vglut1Cre/+; DLK(cKO)fl/fl
P60
Tuj1
CA1
CA3
DG
F
CA1
ns
Tuj1 MFI
30000
20000
10000
0
G
CA3
ns
Tuj1 MFI
40000
30000
20000
10000
0
H
DG
ns
Tuj1 MFI
30000
20000
10000
0
Control
Vglut1Cre/+; DLK(cKO)fl/fl

Figure 2

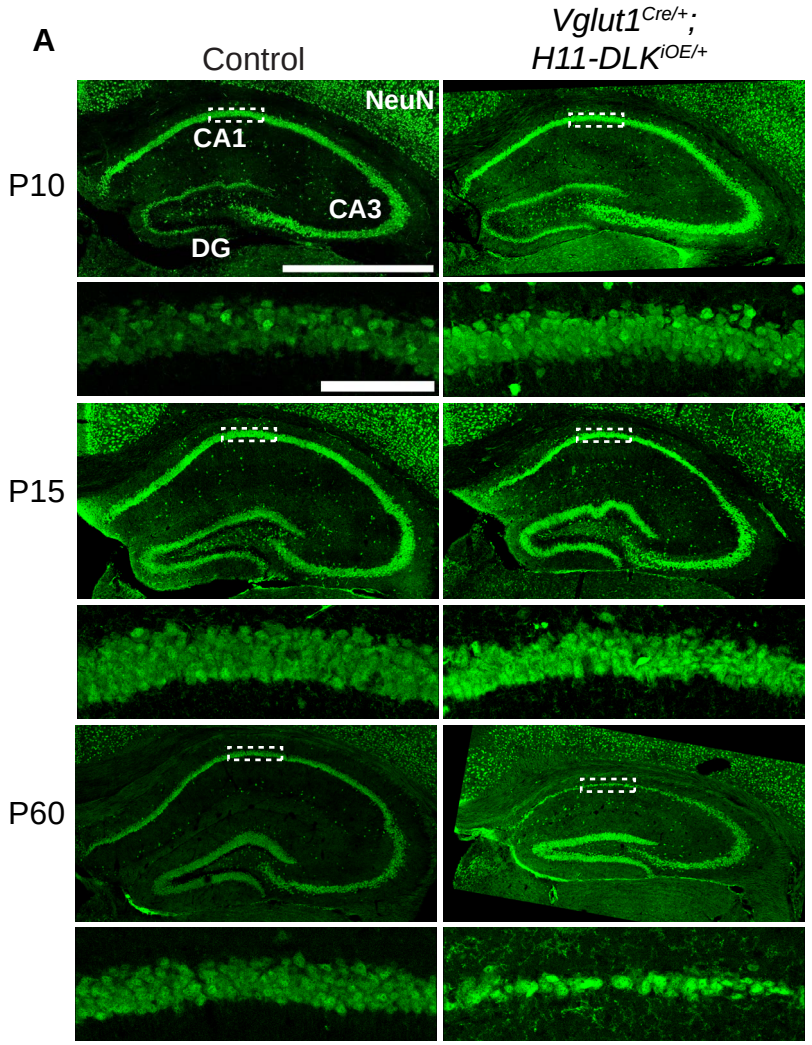
A
Control
Vglut1Cre/+;
H11-DLKiOE/+
NeuN
CA1
CA3
DG
P10
P15
P60

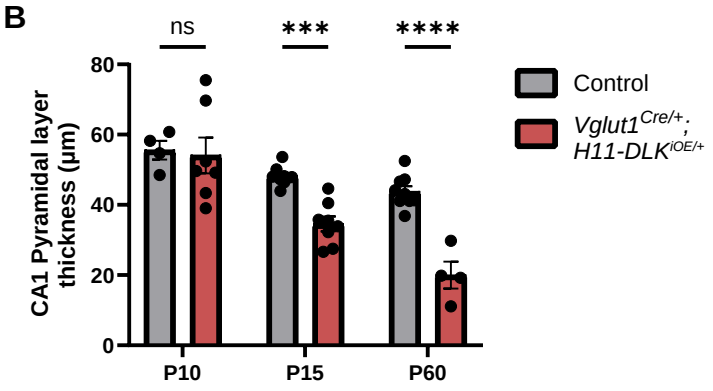
B
ns
***
****
CA1 Pyramidal layer thickness (µm)
80
60
40
20
0
P10
P15
P60
Control
Vglut1Cre/+;
H11-DLKiOE/+

Figure 3

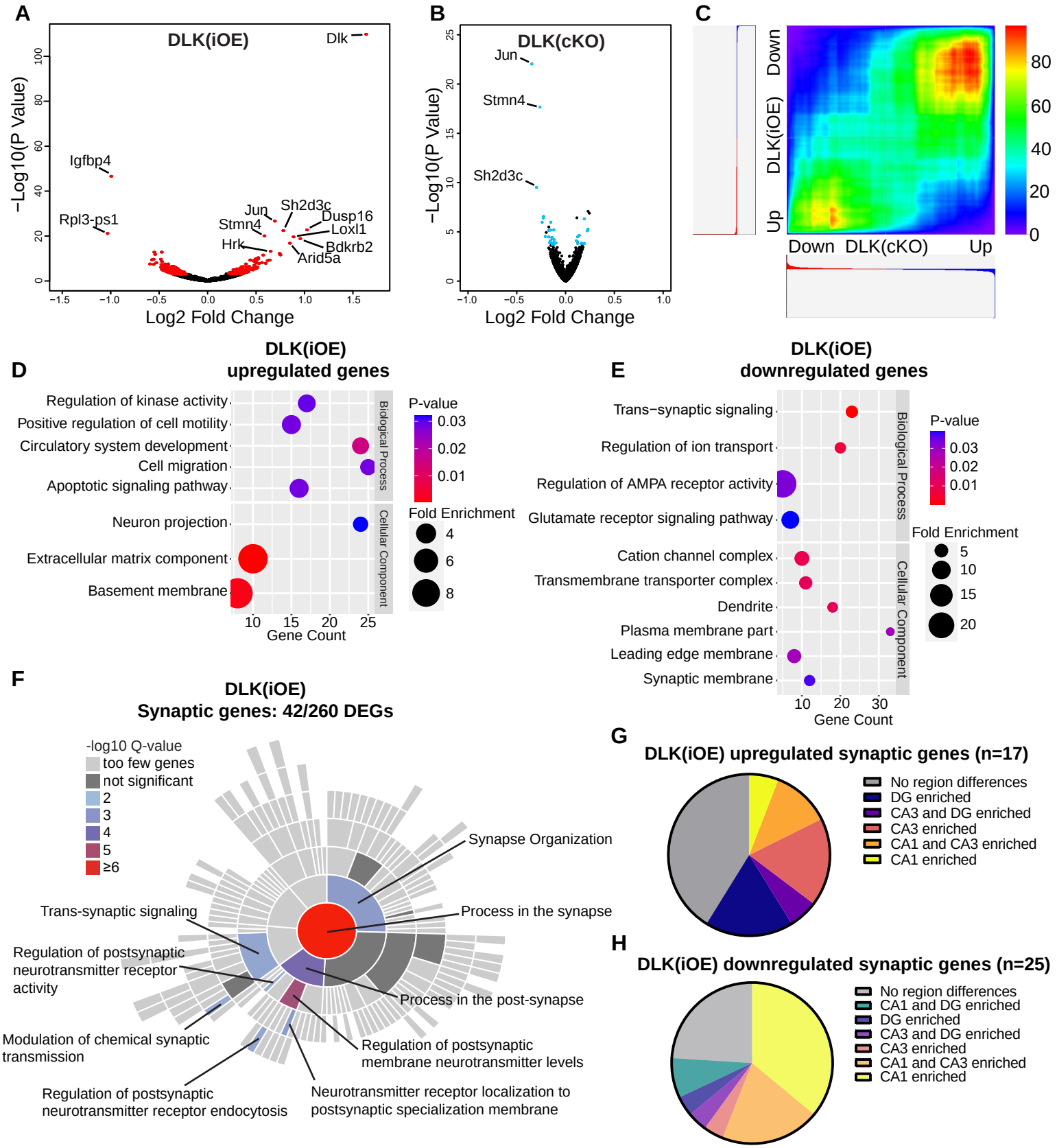
A
DLK(iOE)
Dlk
Igfbp4
Rpl3-ps1
Jun
Stmn4
Hrk
Sh2d3c
Dusp16
Loxl1
Bdkrb2
Arid5a
−Log10(P Value)
Log2 Fold Change
B
DLK(cKO)
Jun
Stmn4
Sh2d3c
−Log10(P Value)
Log2 Fold Change
C
Down
DLK(iOE)
Up
Down
DLK(cKO)
Up
D
DLK(iOE)
upregulated genes
Regulation of kinase activity
Positive regulation of cell motility
Circulatory system development
Cell migration
Apoptotic signaling pathway
Neuron projection
Extracellular matrix component
Basement membrane
Biological Process
Cellular Component
P-value
Fold Enrichment
Gene Count
E
DLK(iOE)
downregulated genes
Trans−synaptic signaling
Regulation of ion transport
Regulation of AMPA receptor activity
Glutamate receptor signaling pathway
Cation channel complex
Transmembrane transporter complex
Dendrite
Plasma membrane part
Leading edge membrane
Synaptic membrane
Biological Process
Cellular Component
P-value
Fold Enrichment
Gene Count
F
DLK(iOE)
Synaptic genes: 42/260 DEGs
-log10 Q-value
too few genes
not significant
2
3
4
5
≥6
Synapse Organization
Process in the synapse
Trans-synaptic signaling
Regulation of postsynaptic neurotransmitter receptor activity
Process in the post-synapse
Modulation of chemical synaptic transmission
Regulation of postsynaptic membrane neurotransmitter levels
Regulation of postsynaptic neurotransmitter receptor endocytosis
Neurotransmitter receptor localization to postsynaptic specialization membrane
G
DLK(iOE) upregulated synaptic genes (n=17)
No region differences
DG enriched
CA3 and DG enriched
CA3 enriched
CA1 and CA3 enriched
CA1 enriched
H
DLK(iOE) downregulated synaptic genes (n=25)
No region differences
CA1 and DG enriched
DG enriched
CA3 and DG enriched
CA3 enriched
CA1 and CA3 enriched
CA1 enriched

Figure 4

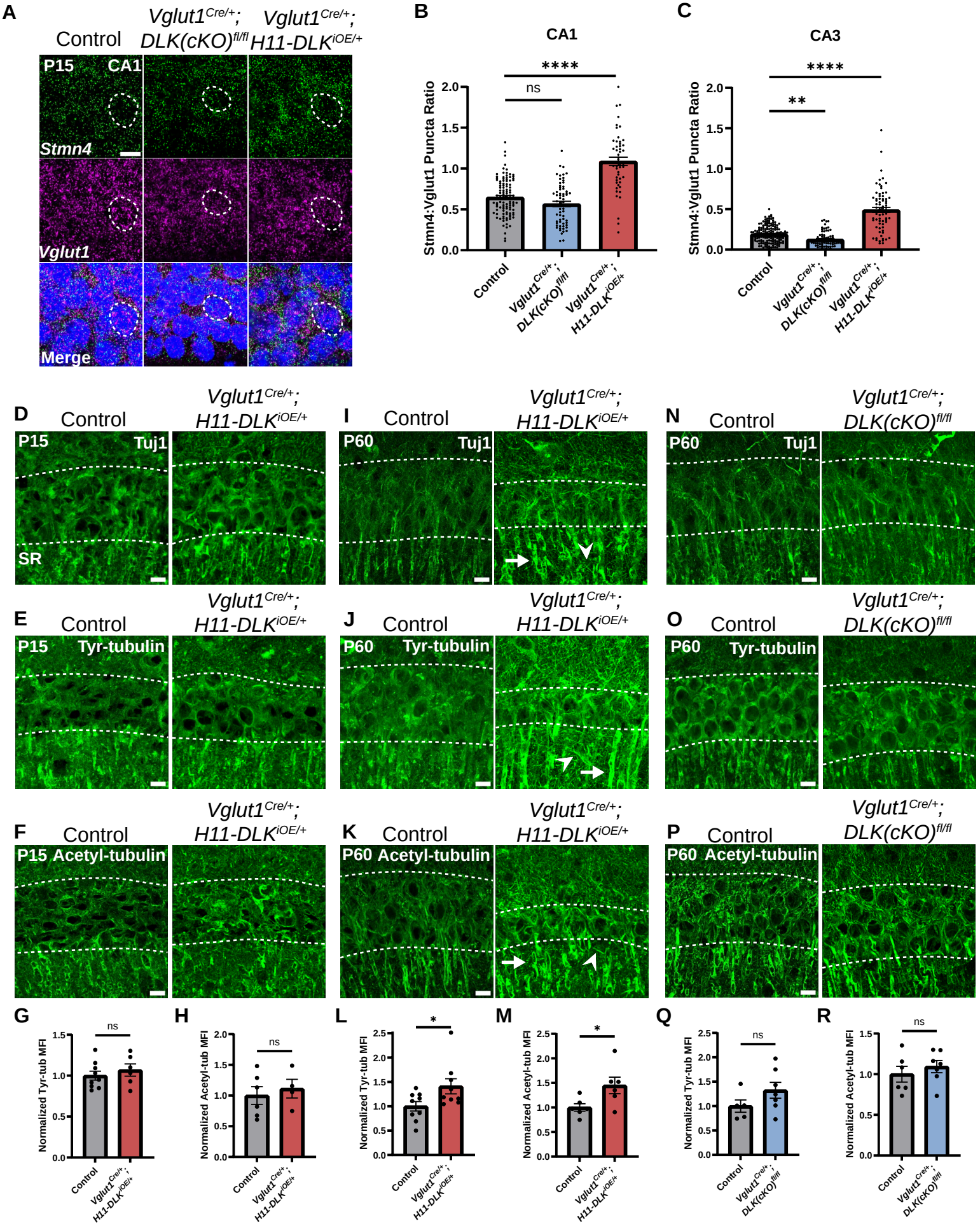
A
Control
Vglut1Cre/+; DLK(cKO)fl/fl
Vglut1Cre/+; H11-DLKiOE/+
P15
CA1
Stmn4
Vglut1
Merge
B
CA1
****
ns
Stmn4:Vglut1 Puncta Ratio
2.0
1.5
1.0
0.5
0.0
Control
Vglut1Cre/+; DLK(cKO)fl/fl
Vglut1Cre/+; H11-DLKiOE/+
C
CA3
****
**
Stmn4:Vglut1 Puncta Ratio
D
Control
Vglut1Cre/+; H11-DLKiOE/+
P15
Tuj1
SR
I
Control
Vglut1Cre/+; H11-DLKiOE/+
P60
Tuj1
N
Control
Vglut1Cre/+; DLK(cKO)fl/fl
P60
Tuj1
E
Control
Vglut1Cre/+; H11-DLKiOE/+
P15
Tyr-tubulin
J
Control
Vglut1Cre/+; H11-DLKiOE/+
P60
Tyr-tubulin
O
Control
Vglut1Cre/+; DLK(cKO)fl/fl
P60
Tyr-tubulin
F
Control
Vglut1Cre/+; H11-DLKiOE/+
P15 Acetyl-tubulin
K
Control
Vglut1Cre/+; H11-DLKiOE/+
P60 Acetyl-tubulin
P
Control
Vglut1Cre/+; DLK(cKO)fl/fl
P60 Acetyl-tubulin
G
ns
Normalized Tyr-tub MFI
H
ns
Normalized Acetyl-tub MFI
L
*
Normalized Tyr-tub MFI
M
*
Normalized Acetyl-tub MFI
Q
ns
Normalized Tyr-tub MFI
R
ns
Normalized Acetyl-tub MFI
Control
Vglut1Cre/+; H11-DLKiOE/+
Vglut1Cre/+; DLK(cKO)fl/fl

Figure 5

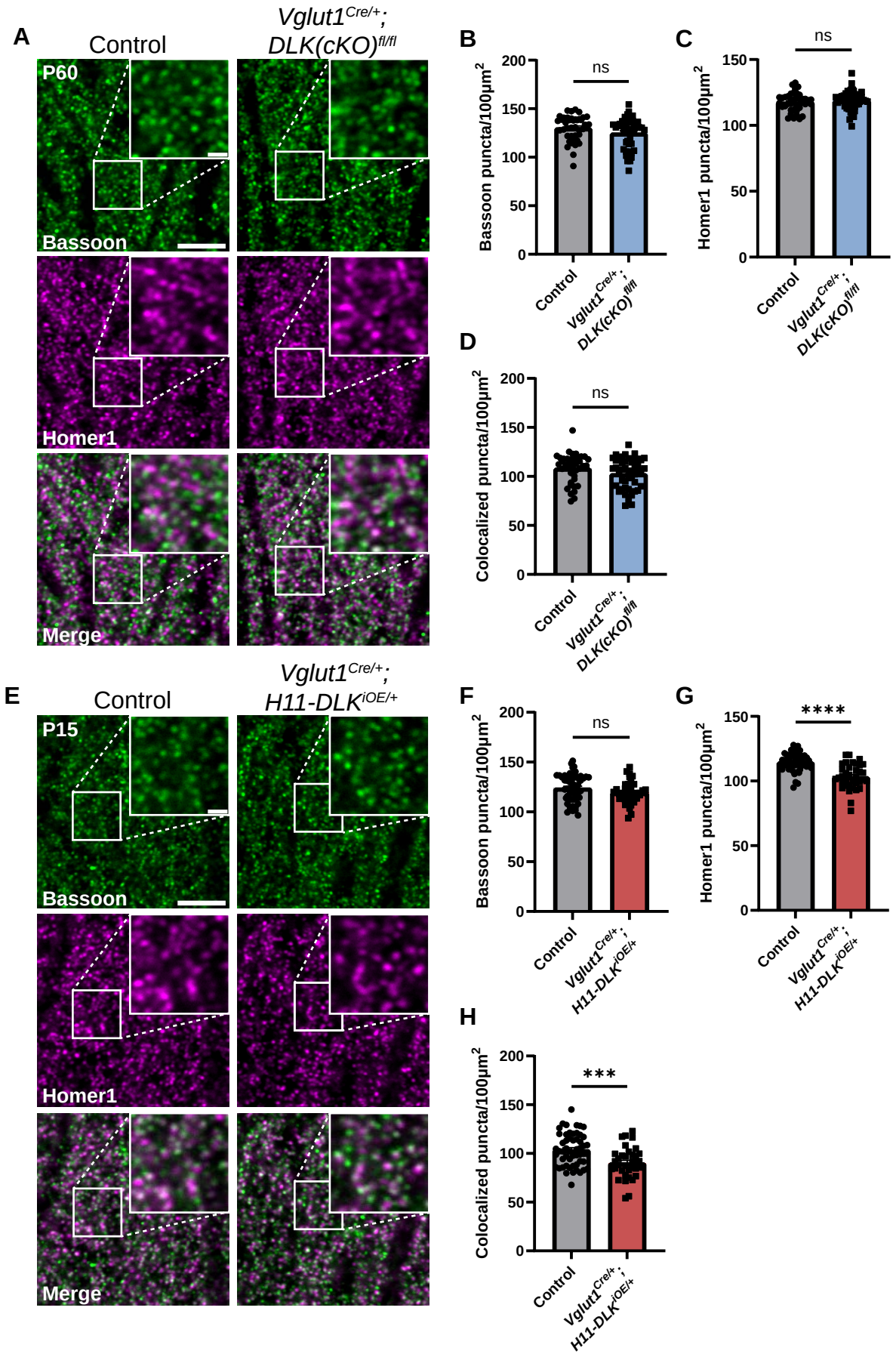
A
Control
Vglut1Cre/+; DLK(cKO)fl/fl
P60
Bassoon
Homer1
Merge
B
Bassoon puncta/100μm2
ns
Control
Vglut1Cre/+; DLK(cKO)fl/fl
C
Homer1 puncta/100μm2
ns
D
Colocalized puncta/100μm2
ns
E
Control
Vglut1Cre/+; H11-DLKiOE/+
P15
Bassoon
Homer1
Merge
F
Bassoon puncta/100μm2
ns
G
Homer1 puncta/100μm2
****
H
Colocalized puncta/100μm2
***

Figure 6

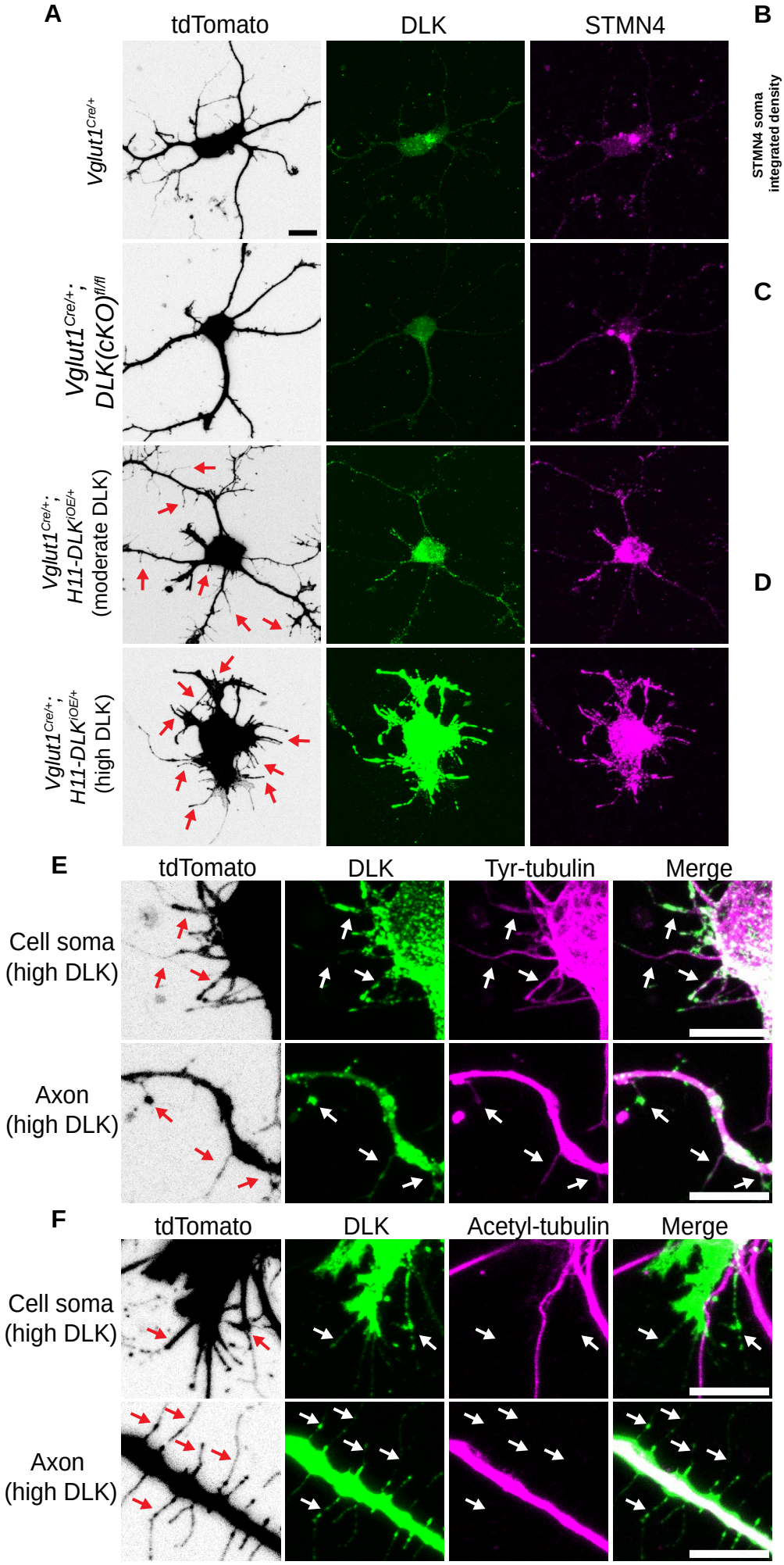
A
tdTomato
DLK
STMN4
Vglut1Cre/+
Vglut1Cre/+; DLK(cKO)fl/fl
Vglut1Cre/+; H11-DLKiOE/+ (moderate DLK)
Vglut1Cre/+; H11-DLKiOE/+ (high DLK)
B
Spearman correlation
r=0.7454
STMN4 soma integrated density
DLK soma integrated density
C
No axon
1 axon
Multiple axons
% of neurons
D
Primary neurite #/cell
****
****
E
tdTomato
DLK
Tyr-tubulin
Merge
Cell soma (high DLK)
Axon (high DLK)
F
tdTomato
DLK
Acetyl-tubulin
Merge
Cell soma (high DLK)
Axon (high DLK)

Figure 7

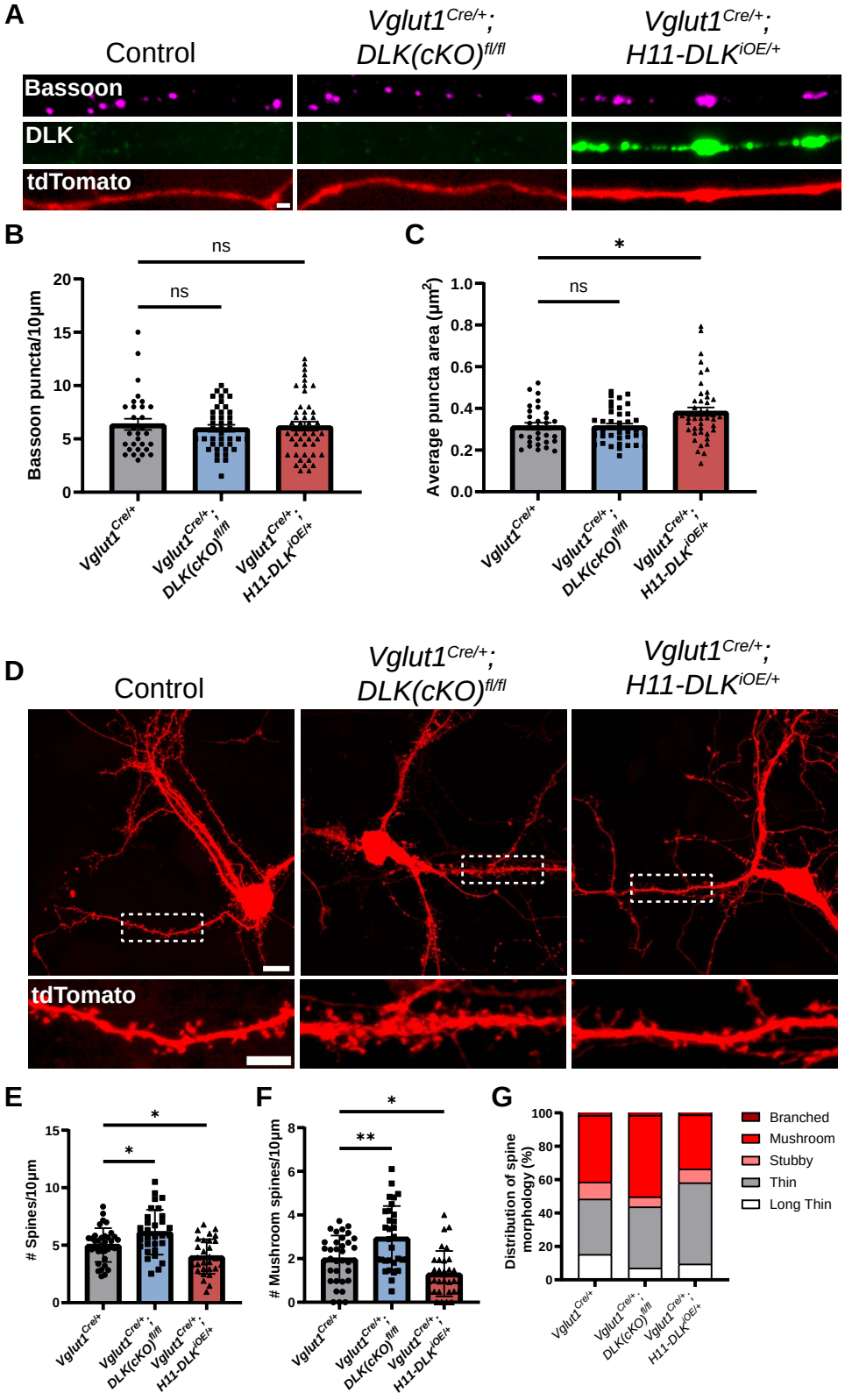
A
Control
Vglut1Cre/+; DLK(cKO)fl/fl
Vglut1Cre/+; H11-DLKiOE/+
Bassoon
DLK
tdTomato
B
ns
ns
Bassoon puncta/10µm
C
*
ns
Average puncta area (µm2)
D
Control
Vglut1Cre/+; DLK(cKO)fl/fl
Vglut1Cre/+; H11-DLKiOE/+
tdTomato
E
*
*
Spines/10µm
F
*
**
Mushroom spines/10µm
G
Distribution of spine morphology (%)
Branched
Mushroom
Stubby
Thin
Long Thin

Supplemental methods

HIPPOCAMPAL SPATIAL EXPRESSION ANALYSIS

False color expression images from the Allen Mouse Brain Atlas were used for evaluating expression pattern, and numbers were assigned based on color in dorsal hippocampus (Red=3, Yellow=2, Blue/Green=1, No=0). When intensity varied across sections or intensity was in-between two categories, preference was given to depicting general patterns of relative expression over absolute signal. When *in situ* data was not available, or expression patterns were unclear, we used additional transcriptomic data to assess spatial expression (Habib et al., 2016; Zeisel et al., 2018), and values were chosen to reflect relative expression. Generally, the following scale was used for Habib et al., 2016 data through the Single Cell Portal: 0 if next to no signal, 1 if expression in some cells, but average was still zero, 2 if quartile 3 value in violin plot is >0, 3 if higher average signal, again values were chosen to reflect relative expression. Genes were categorized as enriched in a region/s if one or two regions show higher values than another region. If two regions show different expression levels but are two levels above third region, the gene is considered as enriched in both (i.e., CA1=2, CA3=3, DG=0, considered as CA1, CA3 enriched). If only one level above other regions, the gene is enriched only in the region with strongest expression (i.e., CA1=3, CA3=2, DG=1, considered as CA1 enriched). Most expressed elsewhere in hippocampus used when the strongest expression is found in another region/cell type, and other descriptions don't explain where most of the signal is.

STMN2/STMN4 ANTIBODY SPECIFICITY

Given their highly similar protein size and sequences, we wanted to evaluate STMN2 and STMN4 antibody specificity. We used two antibodies for each. STMN2 antibodies were a mouse monoclonal anti-STMN2 (R&D Systems, MAB6930) and a rabbit polyclonal anti-STMN2 (Proteintech, 10586-1-AP). STMN4 antibodies were a mouse monoclonal anti-STMN4 (Santa Cruz, Sc-376936) and a rabbit polyclonal anti-STMN4 (Proteintech, 12027-1-AP). We tested the specificity of STMN2 and STMN4 antibodies by co-staining for STMN2 and STMN4, or with two separate STMN2 or STMN4 antibodies. In each case, antibody signal overlapped in the cell soma, presumably at the Golgi, as well as larger puncta elsewhere, with some overlapping small puncta, and some non-overlapping small puncta (Fig.S11A). Overlapping and non-overlapping signal can also be visualized by plotting intensity of signal along the neurite. By western blot STMN2 and STMN4 are highly similar at the protein level, with similar size proteins, though the STMN4 antibodies tested display a larger MW band specific to STMN4,

suggesting some specificity. The STMN2 antibodies also occasionally recognized a smaller MW band only recognized with one of the STMN4 antibodies (Fig.S11B). Furthermore, while STMN4 protein levels increased relative to β-actin in mice with increased DLK, STMN2 protein levels did not show significant increases. These different expression patterns further validate some degree of specificity with these antibodies. Whether the antibodies may also detect some of the same isoforms is not clear without further analysis.

Supplemental Figure 1. Additional evidence for expression levels of DLK and effects on hippocampal morphology at 1 year of age

(A) Confocal images of *Dlk* and *Vglut1* RNA expression in hippocampal glutamatergic neurons at P15. Scale bar 1000μm, 10μm zoomed ROI. (B) Long exposure western blot of DLK and β-actin from hippocampal tissue, arrow indicates lower band for DLK associated with conditional knockout (age P60, each lane representing protein sample from individual mice, N=3 mice/genotype). (C) IGV visual of representative *Vglut1*$^{Cre/+}$ and *Vglut1*$^{Cre/+}$*;DLK(cKO)*$^{fl/fl}$ reads for *Dlk* from P15 RiboTag data reveal reduced expression of floxed exon (~1/3 level of control). Other exons remained at a similar level as control. *Dlk* exon structure shown along the bottom in dark blue, with start ATG noted. Red region indicates exon deleted in conditional knockout. Height of reads (y-axis) in gray or blue represents number of reads overlapping a given sequence. (D,E) Confocal z-stack images of coronal sections from ~1 year old mice from CA1, CA3, and DG dorsal hippocampus immunostained for NeuN and DAPI in (D) control and *Vglut1*$^{Cre/+}$*;DLK(cKO)*$^{fl/fl}$ mice (1 year), (E) control and *Vglut1*$^{Cre/+}$*;H11-DLK*$^{iOE/+}$ mice (44-46 weeks old). Outlines highlight cell somas of pyramidal layer or granule cell layer. Scale bar 100μm. (F,G,H) Quantification of cross-sectional area from CA1, CA3, or DG dorsal hippocampus, respectively. Data points represent individual mice, averages taken across 3 sections per mouse, N≥3 mice/genotype. Statistics: One way ANOVA with Dunnett's multiple comparison test. ns, not significant; **** P<0.0001.

Supplemental Figure 2. Evidence for induced DLK expression visualized at RNA and protein levels.

(A) Confocal z-stack images of *Vglut1* and *Dlk* mRNA at P15 in control and *Vglut1*$^{Cre/}$*;H11-DLK*$^{iOE/+}$ mice. Scale bar 1000μm. Inset shows single slice CA1 neurons, with dashed line showing individual nuclei as used for quantification, scale bar 10μm. (B) Quantification of puncta shown as ratio of *Dlk* puncta to *Vglut1* puncta overlapping with individual CA1 neuron nuclei. Statistics: Mann-Whitney U test. **** P<0.0001. (C) Confocal z-stack images of control and *Vglut1*$^{Cre/+}$*;H11-DLK*$^{iOE/+}$ mice immunostained for DLK protein (P60). Scale bar 1000μm. Blue box, magnified view of pyramidal cell layer/stratum pyramidale (SP), scale bar 10μm. Yellow box, magnified view of stratum lacunosum-moleculare (SLM), scale bar 10μm.

Supplemental Figure 3. Region dependent vulnerability observed with increased DLK expression.

(A) Confocal z-stack images of ventral hippocampus in control and *Vglut1*$^{Cre/+}$*;H11-DLK*$^{iOE/+}$ mice immunostained for NeuN protein (P60). Dashed line regions are enlarged to the right. Top zoomed view shows dorsal (posterior) CA1 neurons with some thinning of pyramidal layer in mice with increased DLK. Bottom zoomed view shows ventral CA1 neurons appearing similar between genotypes. Scale bar: 1,000μm in hippocampi; 100μm in CA1 layer. (B) Quantification of pyramidal layer thickness across CA1. CA1 dorsal (anterior) data from Figure 1B. Data points represent individual mice, averages taken across 2-3 sections per mouse. Statistics: Unpaired t-test. ns, not significant; **** P<0.0001. (C) Confocal z-stack images of P60 dorsal and ventral hippocampus immunostained for p-c-Jun. Dashed line regions are enlarged to the right. Scale bar: 1,000μm in hippocampi; 100μm in CA1 layer.

Supplemental Figure 4. Additional evidence for DLK induced hippocampal neuron death.

(A) Confocal z-stack imaging of GFAP immunostaining at P15 and P120. Scale bar 500μm. Boxed areas represent areas for quantification. (B-D) Mean fluorescent intensity of GFAP at P15 in CA1, CA3, and DG regions, respectively. N= 5, 4 mice, quantified from 3 sections per mouse. Statistics: Unpaired t-test. ns, not significant; * P<0.05. (E) Single slice confocal image of TUNEL positive P15 CA1 pyramidal neuron in *Vglut1*$^{Cre/+}$*;H11-DLK*$^{iOE/+}$ overlapping with DLK transgene-dependent tdTomato expression and pyknotic nuclei. Scale bar 25μm. (F) Quantification of TUNEL positive neurons in CA1 pyramidal layer. Data points represent individual mice, averages taken across 3 sections per mouse, N=4 mice. Statistics: Unpaired t-test. ** P<0.01.

Supplemental Figure 5. Evidence for RiboTag samples and additional analysis of genes showing differential dependence on DLK expression levels.

(A) Western blot validation of immunoprecipitation of HA-tagged Rpl22. (B) qRT-PCR expression of *Vglut1* (glutamatergic neuron marker), *Wfs1* (CA1 marker), *Vgat* (inhibitory neurons), *Gfap* (astrocytes) shows expression of transcripts expressed in glutamatergic neurons and depletion of non-glutamatergic neuron transcripts. N=3 biological replicates, data shown as fold change of expression of marker genes in immunoprecipitated glutamatergic neuron RNA relative to whole hippocampal RNA. Normalized to *Gapdh* expression. (C) Venn diagram showing overlap of genes with statistically significant differential translation in DLK(cKO) and DLK(OE). (D,E) Heatmaps of significant genes from DLK(cKO) and DLK(OE). Columns

represent individual mice expression levels; rows represent individual genes with the right-hand labels showing which dataset the gene was found to be statistically significant in. Data were normalized by row, with color keys shown above the heatmap. (F,G,H,I) Pie charts show expression of differentially expressed genes based on adult, endogenous expression patterns in the Allen Mouse Brain Atlas *in situ* data. (F,H) Upregulated, or (G,I) downregulated genes when DLK expression is (F,G) increased or (H,I) conditionally knocked out are categorized based on expression patterns in CA1, CA3, and DG in dorsal hippocampus. (J) Sunburst plot shows significant enrichment for differentially expressed genes from DLK(cKO) relating to the synapse. (K) Pathway analysis of expression data for mice with increased DLK compared to control. Nodes represent sets of genes involved in pathways, with size dependent on the number of genes in the pathway. Nodes are clustered in shaded circles based on related pathways. All pathways shown have q-value (false discovery rate <0.05). Red represents pathways enriched in mice with increased DLK. Blue indicates pathways downregulated in mice with increased DLK.

Supplemental Figure 6. Levels of c-Jun and p-c-Jun show dependency on expression levels of DLK.

(A) Confocal z-stack images of CA1, CA3, and DG in control and *Vglut1*$^{Cre/+}$*;DLK(cKO)*$^{fl/fl}$ mice immunostained for c-Jun (P60). Scale bar 50μm. Corresponding DAPI staining is shown alongside for reference, dashed lines outline region used for quantification. Below, quantification of mean fluorescence intensity (MFI) of c-Jun in pyramidal or granule cell layer of each region. Data points represent MFI of individual mice normalized to average from control animals. 3 sections per mouse, N=4,4 mice. Statistics: Unpaired t-test. ns, not significant. (B) Confocal z-stack images of control and *Vglut1*$^{Cre/+}$*;DLK(cKO)*$^{fl/fl}$ mice immunostained for p-c-Jun (P60). Scale bar 50μm. Below, quantification of MFI of p-c-Jun in pyramidal or granule cell layer of each region. Data points represent MFI of individual mice normalized to average from control animals. 3 sections per mouse, N=6, 7 mice. Statistics: Unpaired t-test. ns, not significant; * P<0.05. (C) Confocal z-stack images of CA1, CA3, and DG in control and *Vglut1*$^{Cre/+}$*;H11-DLK*$^{iOE/+}$ mice immunostained for c-Jun (P15). Scale bar 50μm. Data points represent MFI of individual mice normalized to average from control animals. 3 sections per mouse, N=7,8 mice. Statistics: Unpaired t-test. ** P<0.01; **** P<0.0001. (D) Confocal z-stack images of CA1, CA3, and DG in control and *Vglut1*$^{Cre/+}$*;H11-DLK*$^{iOE/+}$ mice immunostained for p-c-Jun. Scale bar 50μm. Data points represent average number of p-c-Jun positive nuclei in ROIs from individual

mice normalized to average from control animals. 3-5 sections per mouse, N=4,5 mice. Statistics: Unpaired t-test. ** P<0.01; *** P<0.001.

Supplemental Figure 7. Stathmin transcript abundance and western blot analysis of DLK, STMN4 in mice aged P10 to 1 yr.

(A) RiboTag transcript abundance of Stathmin family members in transcripts per million (TPM). Differential expression analysis significance shown (p_{adj}). ns, not significant; **** P<0.0001. (B,C) Western blot of hippocampal tissue from P1, P8, P15, P60, and ~1yr old mice blotted for DLK, Flag, STMN4, STMN2, and actin in *Vglut1*$^{Cre/+}$*;DLK(cKO)*$^{fl/fl}$ and *Vglut1*$^{Cre/+;}$*H11-DLK*$^{iOE/+}$, respectively. (D,E) Relative DLK protein level normalized to actin and P1 control. N=3 mice/genotype. (F,G) Relative STMN4 protein level normalized to actin and P1 control. N=3 mice/genotype. Statistics: Two-way ANOVA with Sidak multiple comparisons test. ns, not significant; * P<0.05.

Supplemental Figure 8. Additional evidence for *Stmn4* and microtubule expression in DLK(cKO) and DLK(iOE) in hippocampus.

(A,B,D,E) Confocal single slice images of *Stmn4* and *Vglut1* RNAscope stained sections from (A,B) CA3 and (C,D) DG in (A,C) overexpression mice and (B,D) conditional knockout mice. Scale bar 10μm. (E) Confocal z-stack images of Tuj1 immunostaining of neuron specific beta tubulin in CA1, CA3, and DG at P15. Scale bar 50μm. (F) Confocal z-stack images of MAP2 immunostaining of CA1 pyramidal layer at P60 from control and *Vglut1*$^{Cre/+}$*;H11-DLK*$^{iOE/+}$ mice. Arrows point to apical dendrites with elevated signal. Arrowheads point to thin neurites with elevated signal. Scale bar 10μm. (G) Normalized MAP2 MFI after thresholding signal in SR. N=9, 9 mice, 3 sections averaged per mouse. Statistics: Unpaired t-test. ns, not significant.

Supplemental Figure 9. Increasing expression of DLK alters VGLUT1 pattern in dorsal CA1.

(A) Confocal single slice image of VGLUT1 immunostaining of control and *Vglut1*$^{Cre/+}$*;DLK(cKO)*$^{fl/fl}$ mice in CA1 SR at P60. Scale bar 5μm, inset scale bar 1μm. (B) VGLUT1 puncta density and (C) size. Data points represent individual ROIs quantified from 5-6 images per mouse across 3 sections. N=5 control, and 8 *Vglut1*$^{Cre/+}$*;DLK(cKO)*$^{fl/fl}$ mice. (D) Confocal single slice image of VGLUT1 immunostaining of control and *Vglut1*$^{Cre/+}$*;H11-DLK*$^{iOE/+}$ mice in CA1 SR at P15. Scale bar 5μm, inset scale bar 1μm. (E) VGLUT1 puncta density and (F) size. Data points represent individual ROIs quantified from 5-6 images per mouse across 3

sections, N=9 control, and 8 *Vglut1*$^{Cre/+}$*;H11-DLK*$^{iOE/+}$ mice. (G-I) Quantification from control and *Vglut1*$^{Cre/+}$*;DLK(cKO)*$^{fl/fl}$ mice for (G) Bassoon puncta size, (H) Homer1 puncta size, and (I) size of Bassoon-Homer1 overlap. Data points represent individual ROIs quantified from 5-6 images per mouse across 3 sections. N=7 control, and 8 *Vglut1*$^{Cre/+}$*;DLK(cKO)*$^{fl/fl}$ mice. (J-L) Quantification from control and *Vglut1*$^{Cre/+}$*;H11-DLK*$^{iOE/+}$ mice for (J) Bassoon puncta size, (K) Homer1 puncta size, and (L) size of Bassoon-Homer1 overlap. Data points represent individual ROIs quantified from 5-6 images per mouse across 3 sections, N=9 control, and 6 *Vglut1*$^{Cre/+}$*;H11-DLK*$^{iOE/+}$ mice. Statistics: unpaired t-test or Mann-Whitney U test if not passing normality. ns, not significant; * P<0.05; ** P<0.01; **** P<0.0001.

Supplemental Figure 10. Analysis of Stathmins in primary cultured hippocampal neurons from DLK(cKO) and DLK(iOE).

(A) Confocal z-stack image of Rosa26-tdTomato labeling of neuron morphology at DIV2. Red arrowheads point to long processes considered as axons. Scale bar 100μm. (B) Co-immunostaining of DLK and STMN4 in control growth cone show non-overlapping puncta. (C) Confocal z-stack images of DIV2 primary hippocampal neurons from genotypes indicated immunostained with DLK and STMN2. tdTomato labeling of neurons is from Rosa26-tdTomato. Scale bar 10μm. (D) Quantification of association between DLK level and STMN2 in cell soma. N=3 cultures/genotype, ≥45 cells/genotype. Spearman correlation r=0.4693.

Supplemental Figure 11. Additional evidence for STMN2 and STMN4 antibodies

(A) Confocal single slice images of STMN2 and STMN4 antibody comparison in DIV3 control primary hippocampal neurons. Dashed box outlines enlarged region. Scale bar 10μm full cell, 1μm enlarged region. (B) Western blot of P15 hippocampal tissue for STMN2 and STMN4 antibodies. Lanes 1-3 control for *Vglut1*$^{Cre/+;}$*H11-DLK*$^{iOE/+}$*,* and lanes 7-9 control for *Vglut1*$^{Cre/+}$*;DLK(cKO)*$^{fl/fl}$ genotype referred to as "+". Lanes 4-6 *Vglut1*$^{Cre/+}$*;H11-DLK*$^{iOE/+}$ referred to as "Tg". Lanes 10-12 *Vglut1*$^{Cre/+}$*;DLK(cKO)*$^{fl/fl}$ referred to as "-". (C) STMN2 or STMN4 protein level normalized to actin. N=3 mice/genotype. Statistics: One way ANOVA with Sidak's multiple comparison test. ns, not significant; * P<0.05.

Supplementary Figure 1

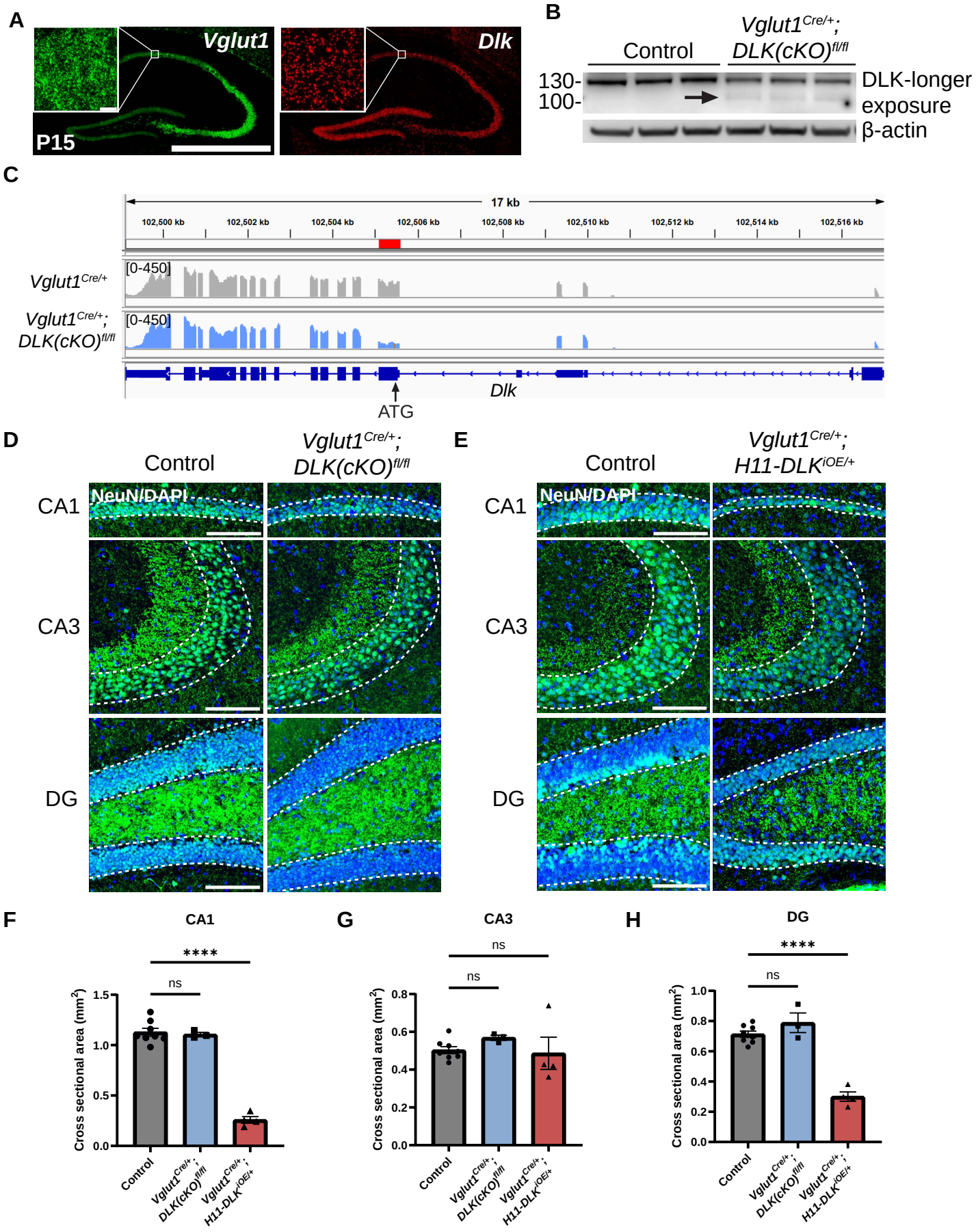

Supplementary Figure 2

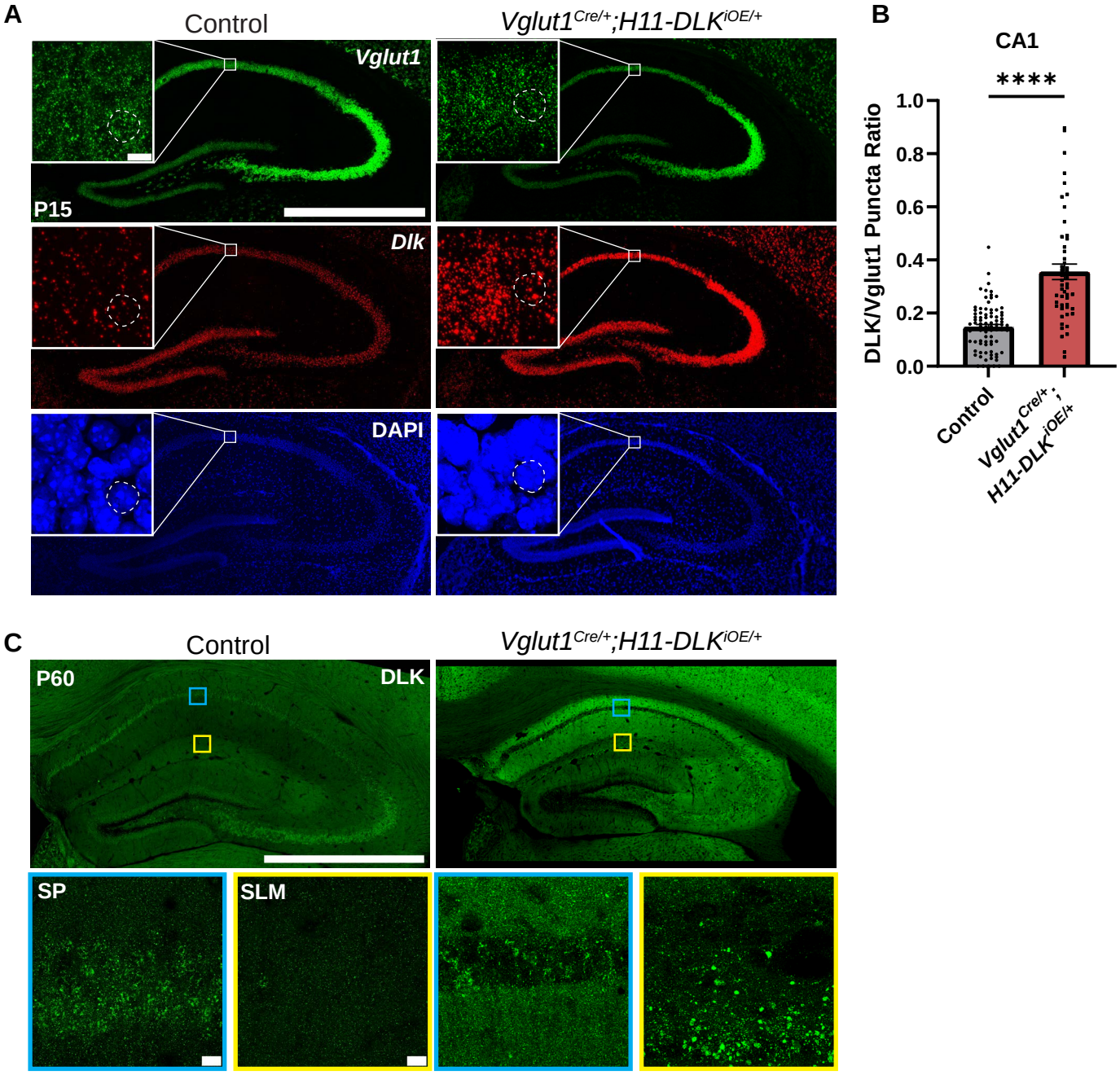

Supplementary Figure 3

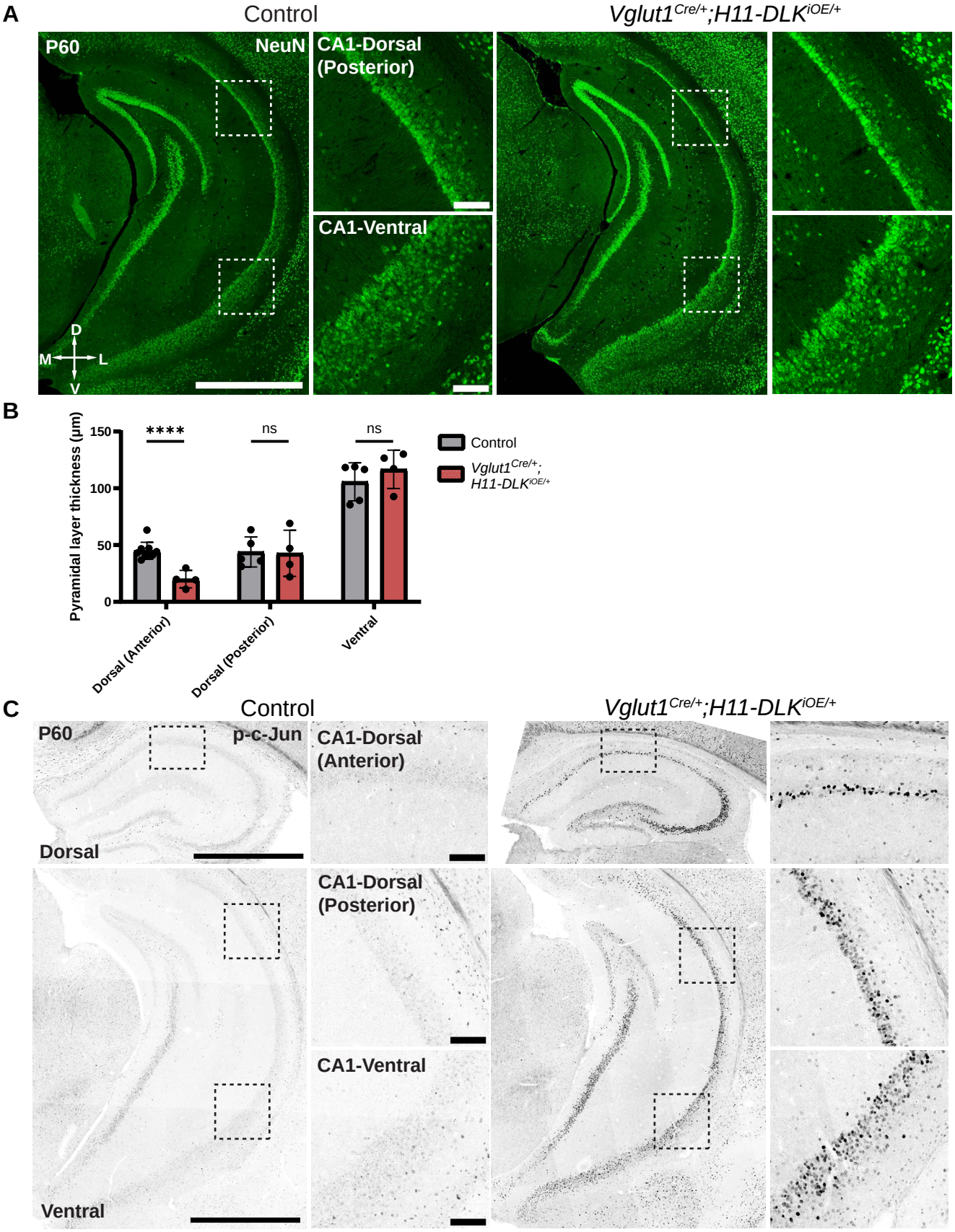

Supplementary Figure 4

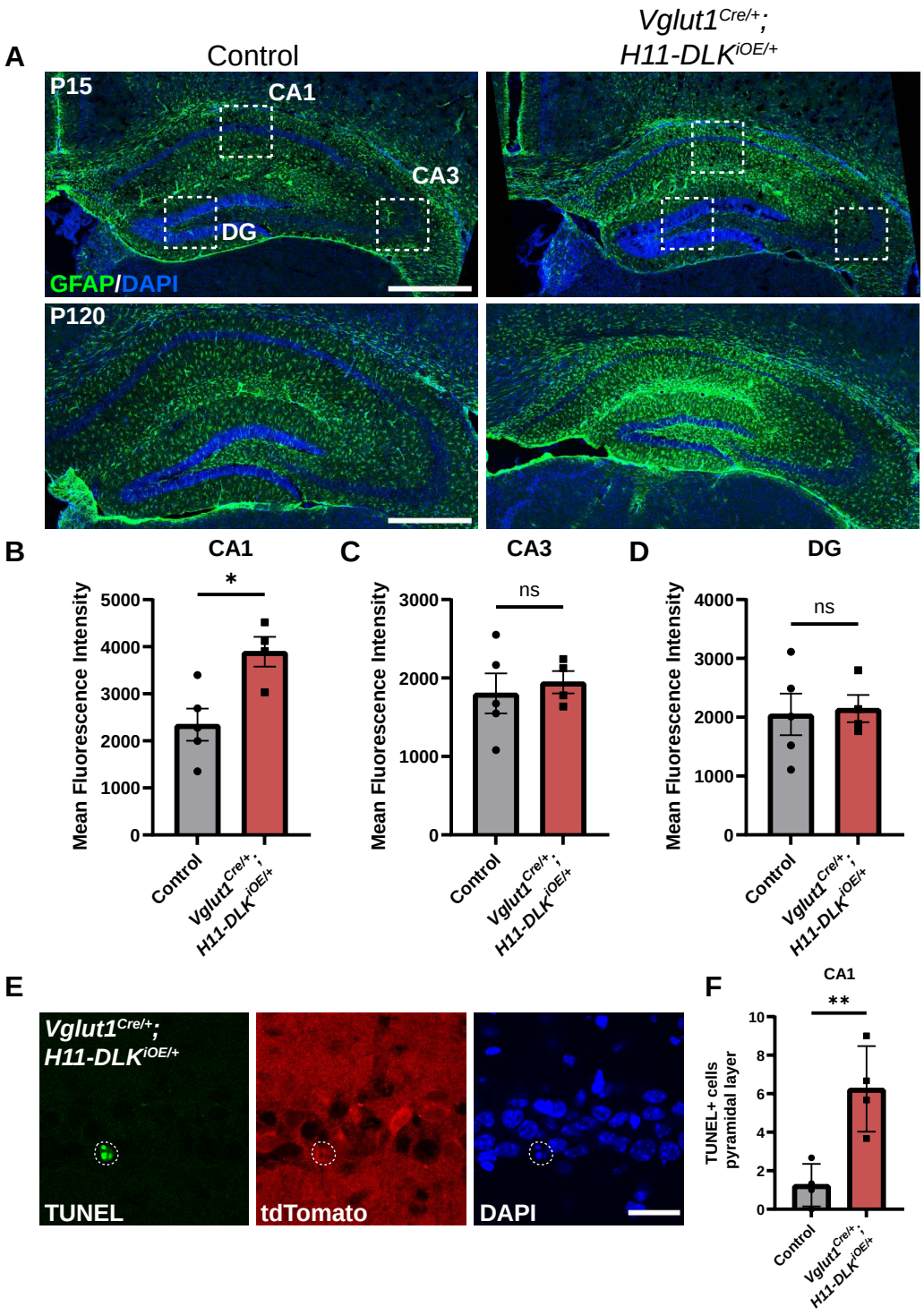

Supplemental Figure 5

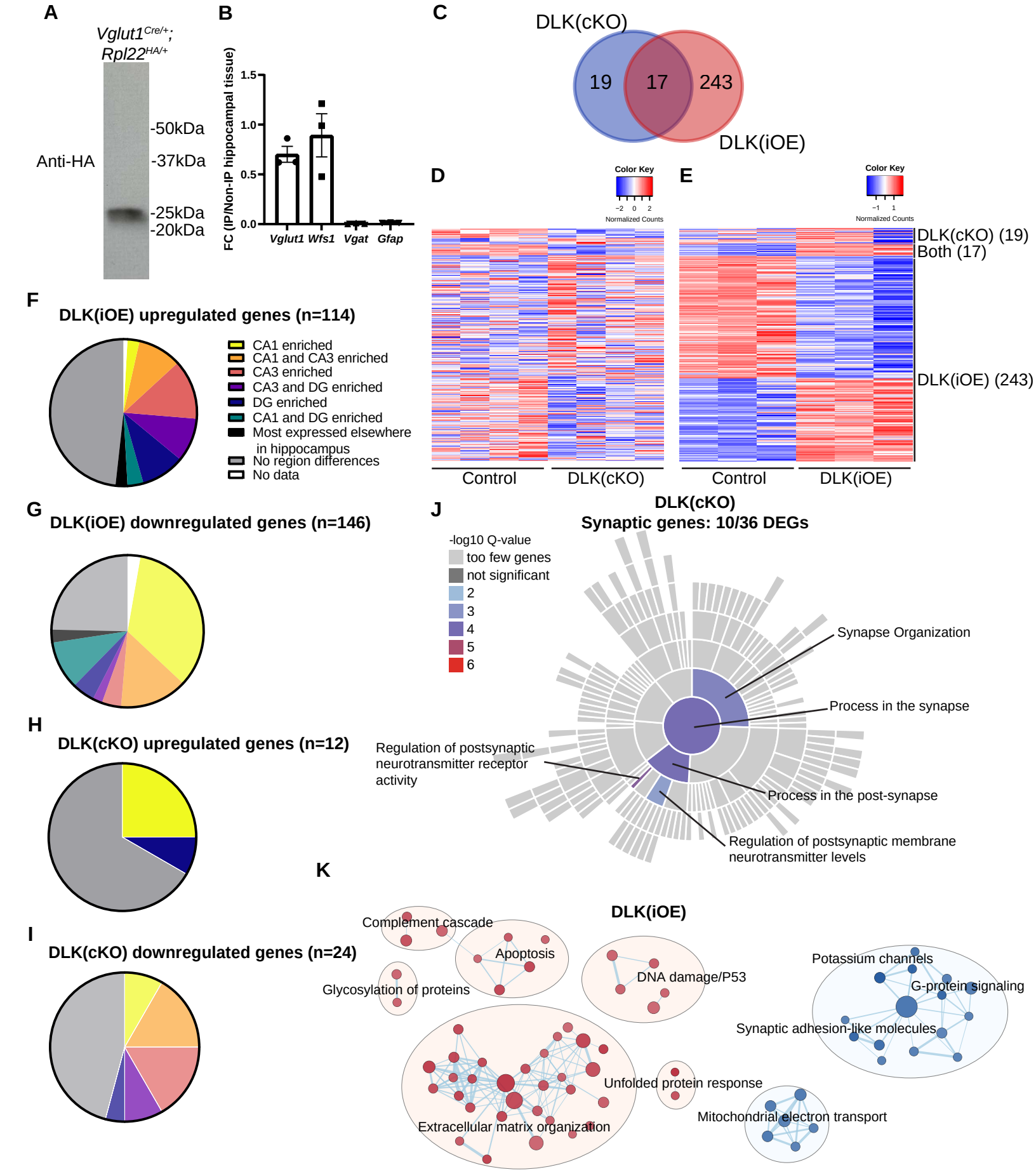

Supplemental Figure 6

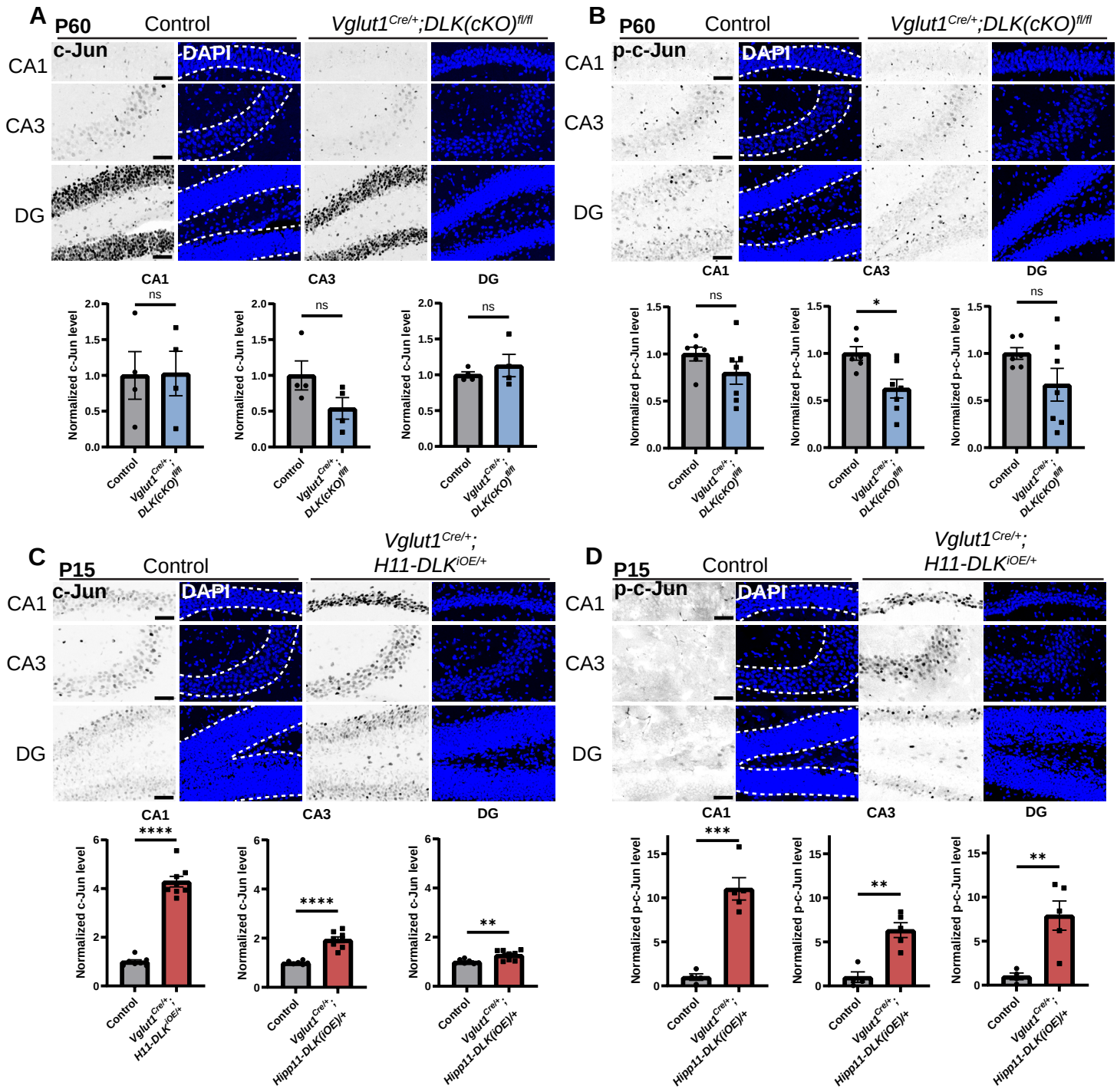

Supplemental Figure 7

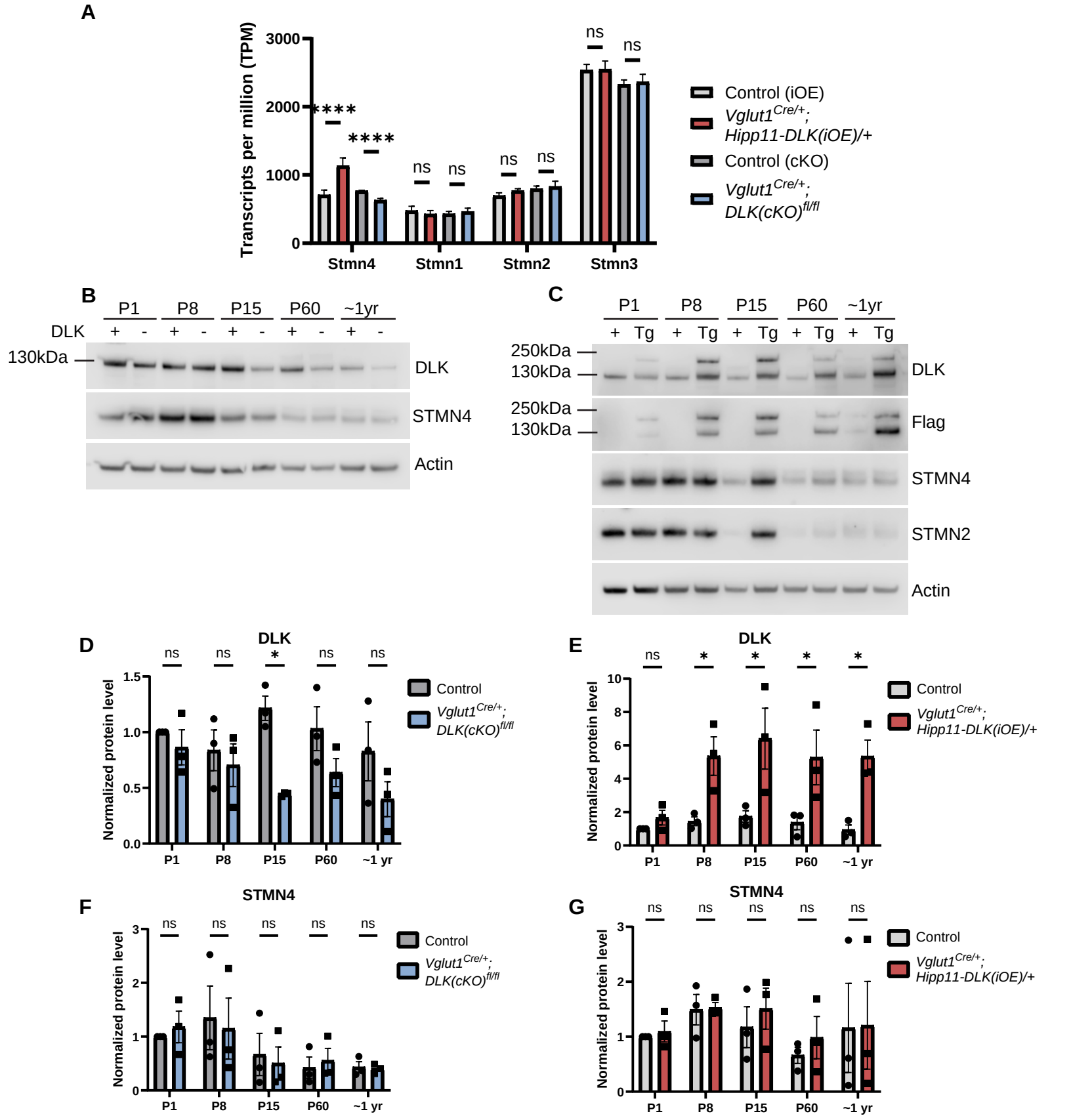

Supplemental Figure 8

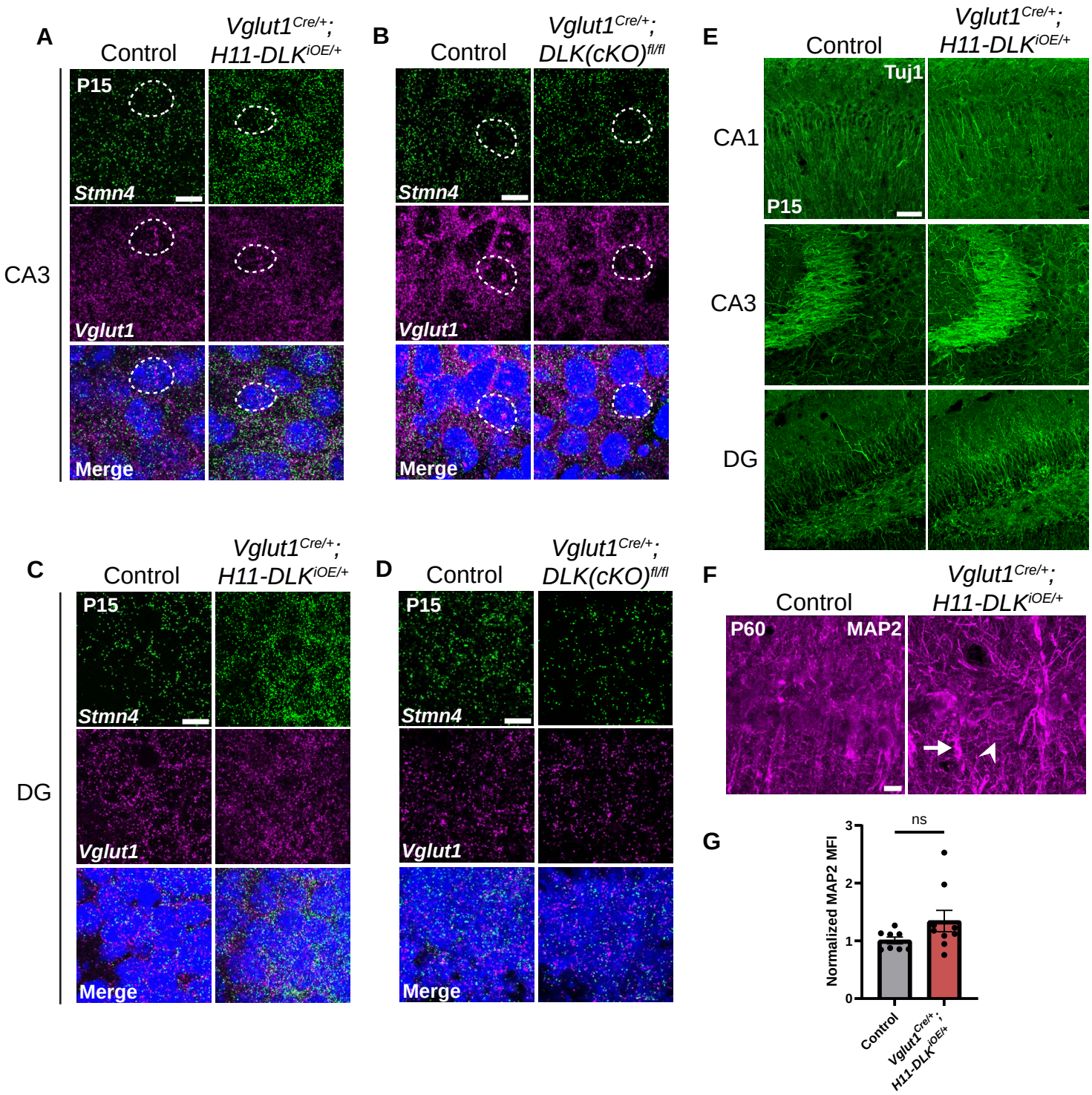

Supplemental Figure 9

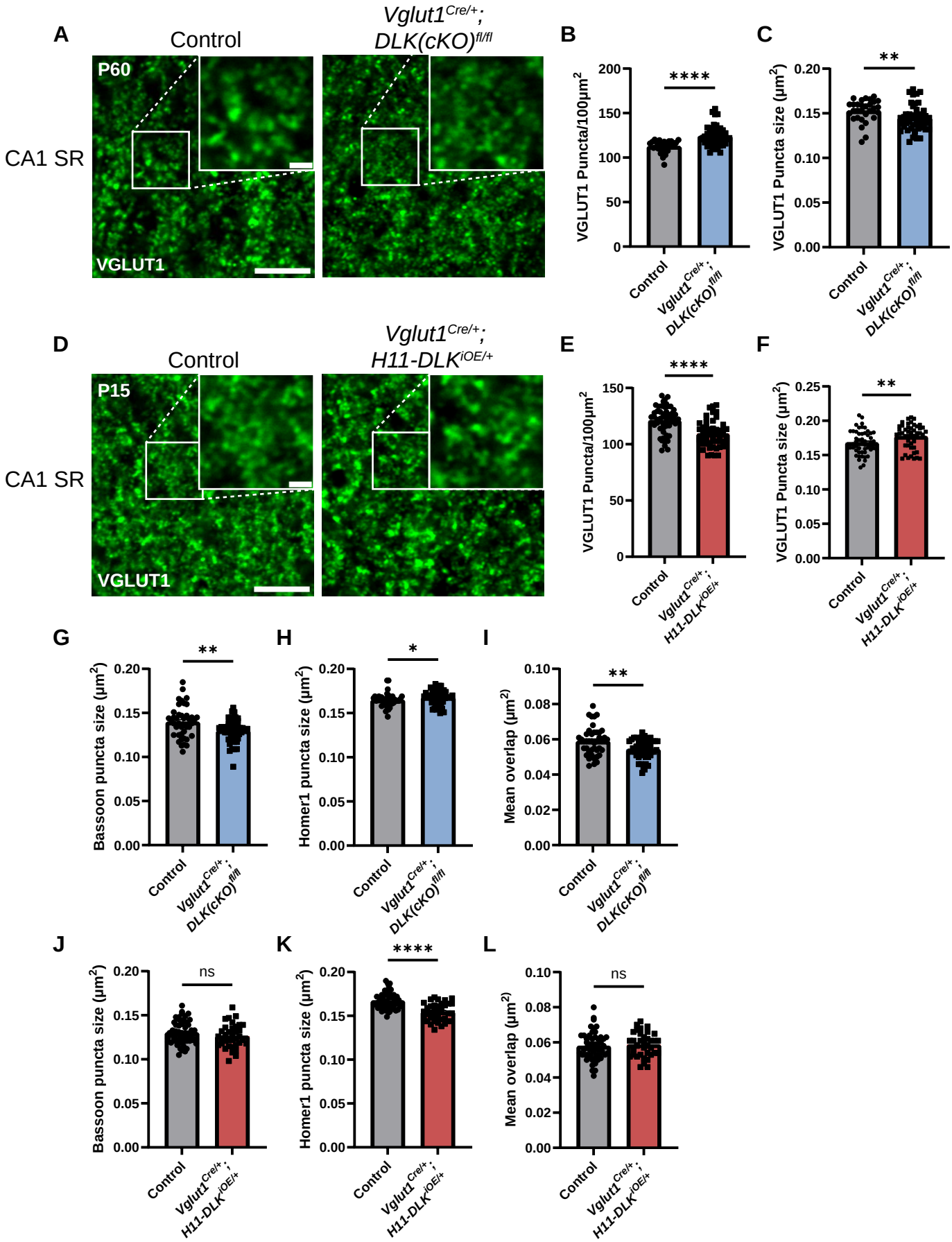

Supplemental Figure 10

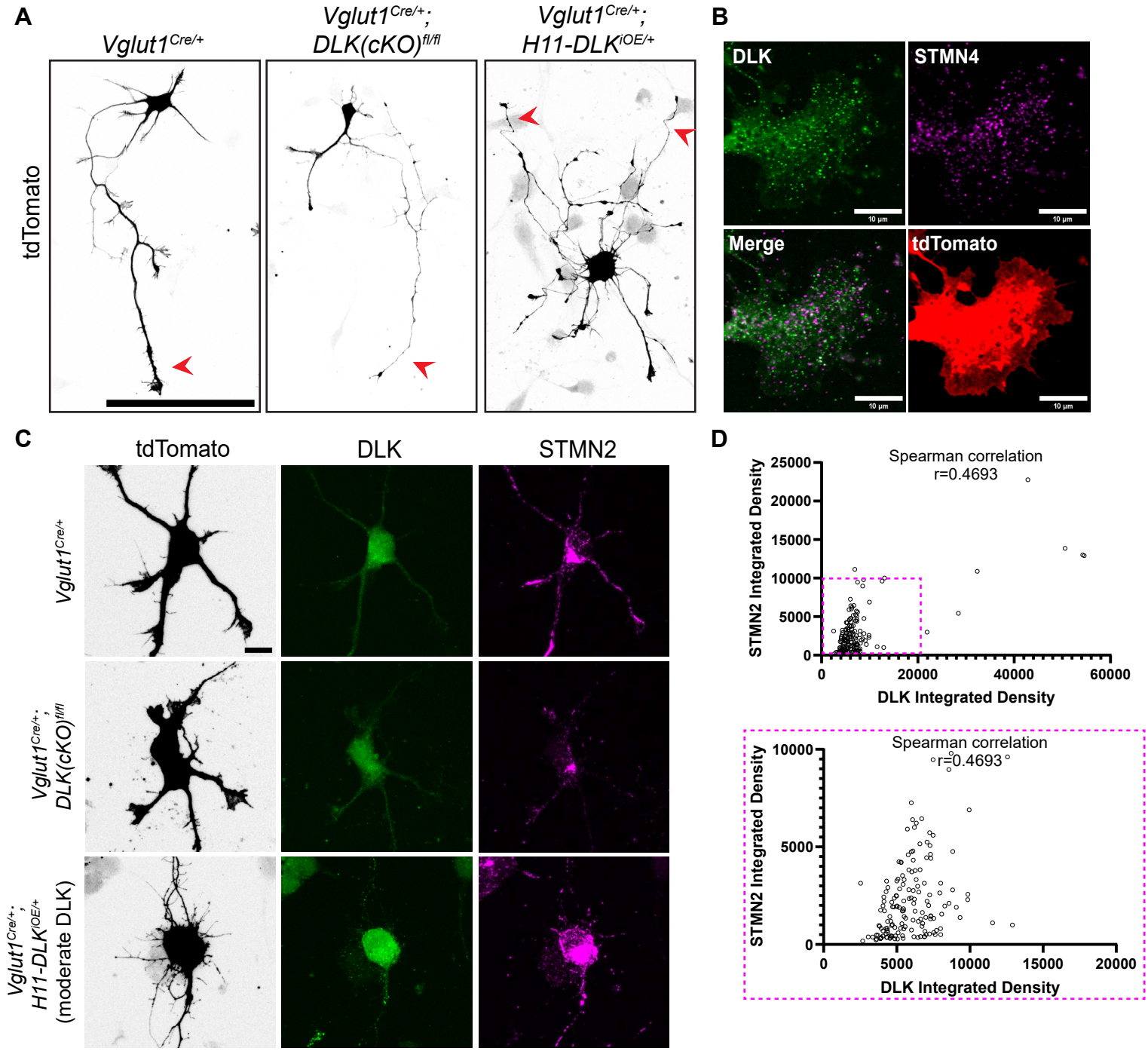

Supplemental Figure 11

A

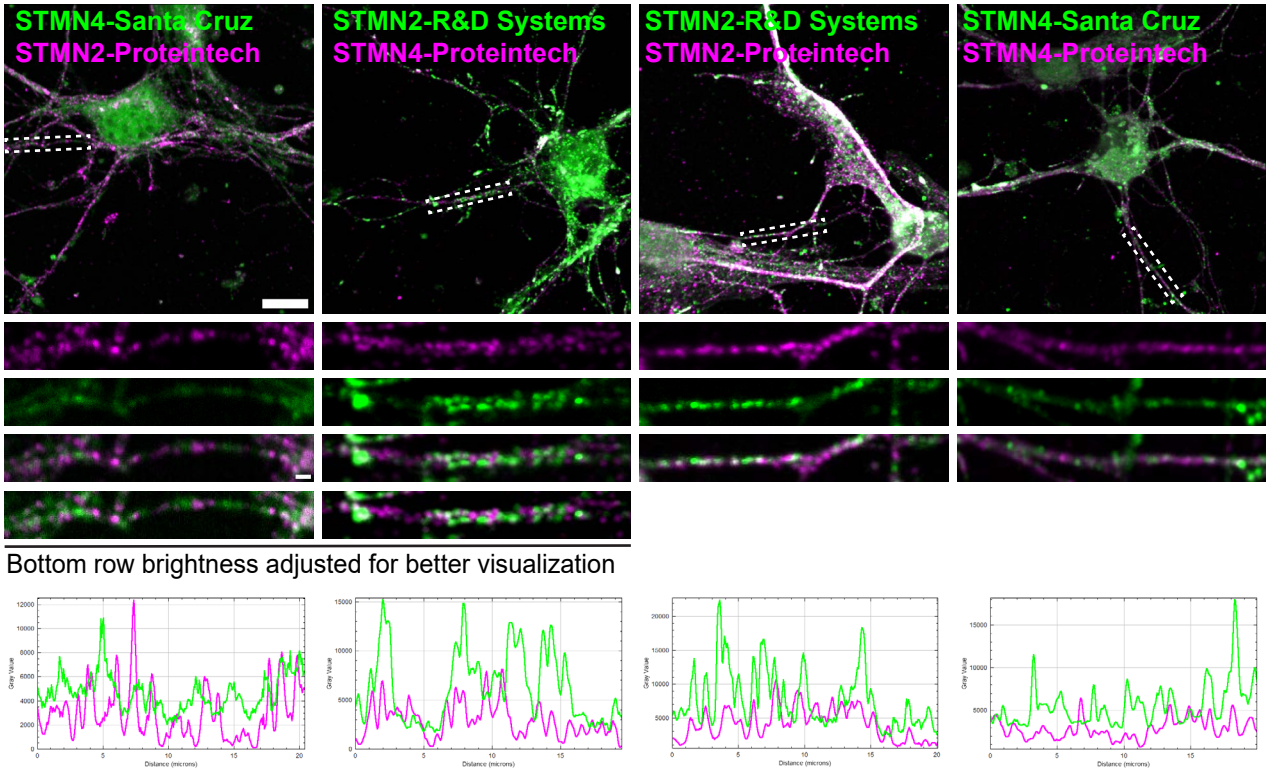

B

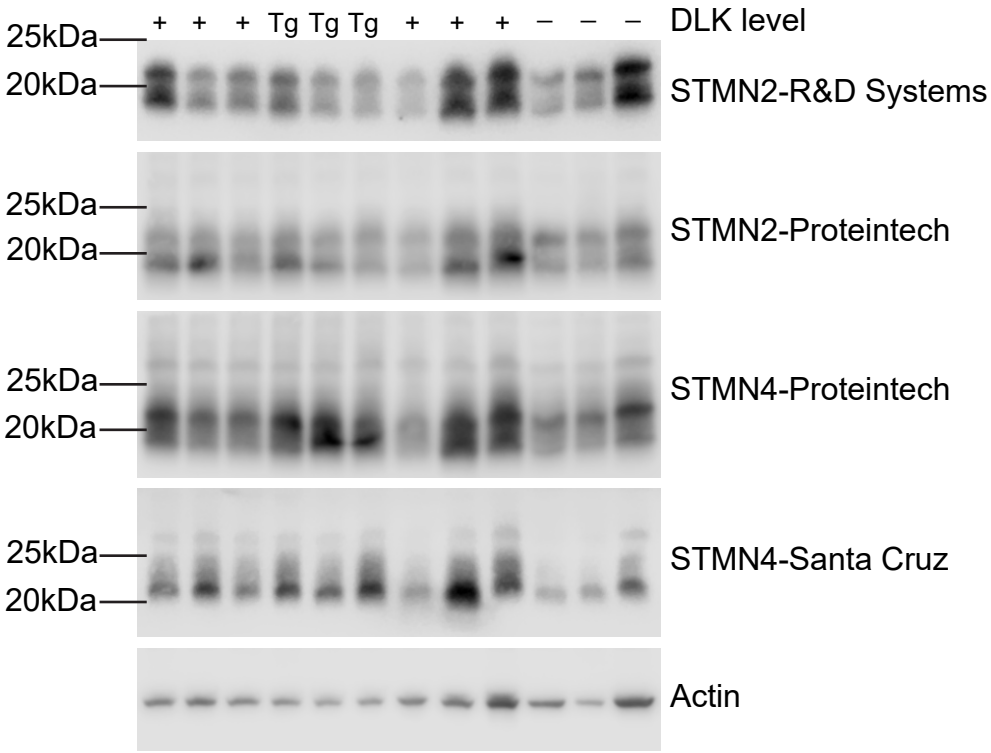

C

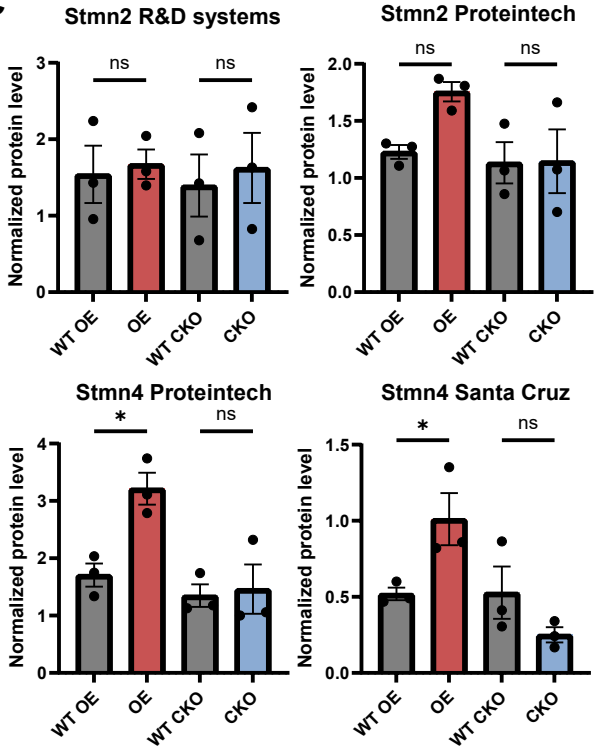

Table S1. Primers

Primers for genotyping			
Reagent or resource	Source	Identifier	Additional information
Hipp11 WT-Fw: TGGAGGAGGACAAACTGGTCA	Li et al., 2021	YJ12520	323bp (*Dlk* Wild-type) ~500bp (*Dlk*^{OE} mutant)
Hipp11 WT-Re: TTCCCTTTCTGCTTCATCTTGC	Li et al., 2021	YJ12521	
CAG-Re: CATATATGGGCTATGAACTAATGACCCCGT	Li et al., 2021	YJ12522	
DLK$^{fx/fx}$-Fw: GATGATTGCTAGTCATGGAGTAGTAGG	Li et al., 2021	YJ12523	350bp (*Dlk* Wild-type) 500bp (*Dlk*$^{fl/fl}$ mutant)
DLK$^{fx/fx}$-Re: GGTGGTGTTATCATAGTTCCATCATG	Li et al., 2021	YJ12524	
RiboTag Fw: GGGAGGCTTGCTGGATATG	Sanz et al., 2009		260bp (WT) 290bp (floxed allele)
RiboTag Re: TTTCCAGACACAGGCTAAGTA	Sanz et al., 2009		
Vglut1-cre Re: CCCTAGGAATGCTCGTCA AG	The Jackson Laboratory	12231	218bp (WT) 344bp (mutant)
Vglut1-cre Fw: ATGAGCGAGGAGAAGTGTGG	The Jackson Laboratory	17904	
Vglut1-cre Re: GTGGAAGTCCTGGAAACTGC	The Jackson Laboratory	17905	
Cre Fw: AGAACCTGAAGATGTTCGCG			~330bp (mutant) No band WT
Cre Re: GGCTATACGTAACAGGGTGT			
Rosa tdTomato Re: GGCATTAAAGCAGCGTATCC	The Jackson Laboratory	oIMR9103	196bp (mutant) 297bp (WT)
Rosa tdTomato Fw: CTGTTCCTGTACGGCATGG	The Jackson Laboratory	oIMR9105	
WT tdTomato Fw: AAGGGAGCTGCAGRGGAGTA	The Jackson Laboratory	oIMR9020	
WT tdTomato Re: CCGAAAATGTGTGGGAAGTC	The Jackson Laboratory	oIMR9021	
Primers for qRT-PCR			
Reagent or resource	Source		
Gapdh-Fw: GCTTGTCATCAACGGGAAG	Furlanis et al., 2019		
Gapdh-Re: TTGTCATATTTCTCGTGGTTCA	Furlanis et al., 2019		
Vgat-Fw: CGTGACAAATGCCATTCAG	Furlanis et al., 2019		
Vgat-Re: AAGATGATGAGGAACAACCC	Furlanis et al., 2019		
Vglut1-Fw: ACCCTGTTACGAAGTTTAACAC	Furlanis et al., 2019		
Vglut1-Re: CAGGTAGAAGGTCCAGCTG	Furlanis et al., 2019		
Wsf1-Fw: CATCATTCCCACCAACCTG	Furlanis et al., 2019		
Wsf1-Re: TACTTCACCACCTTCTGGC	Furlanis et al., 2019		
Gfap-Fw: CTCGTGTGGATTTGGAGAG	Furlanis et al., 2019		
Gfap-Re: AGTTCTCGAACTTCCTCCT	Furlanis et al., 2019		